STARS

Electronic Theses and Dissertations, 2004-2019

2012

Electromagnetic Environment In Payload Fairing Cavities

Dawn Trout

University of Central Florida

Showcase of Text, Archives, Research & Scholarship

ELECTROMAGNETIC ENVIRONMENT IN PAYLOAD FAIRING CAVITIES

by

DAWN TROUT
B.S.E.E Memphis State University, 1989
M.S.E University of Alabama in Huntsville, 1995

A dissertation submitted in partial fulfillment of the requirements
for the degree of Doctor of Philosophy
in the Department of Electrical Engineering and Computer Science
in the College of Engineering and Computer Science
at the University of Central Florida
Orlando, Florida

Spring Term
2012

Major Professor: Parveen Wahid

ABSTRACT

An accurate determination of a spacecraft's radio frequency electromagnetic field environment during launch and flight is critical for mission success. Typical fairing structures consist of a parabolic nose and a cylindrical core with diameters of 1 to 5 meters resulting in electrically large dimensions for typical operational sources at S, C and X band where the free space wavelength varies from 0.15 m to 0.03 m. These electrically large size and complex structures at present have internal fairing electromagnetic field evaluation that is limited to general approximation methods and some test data. Though many of today's computational electromagnetic tools can model increasingly complex and large structures, they still have many limitations when used for field determination in electrically large cavities.

In this dissertation, a series of test anchored, full wave computational electromagnetic models along with a novel application of the equivalent material property technique are presented to address the electrical, geometrical, and boundary constraints for electromagnetic field determination in composite fairing cavity structures and fairings with acoustic blanketing layers. Both external and internal excitations for these fairing configurations are examined for continuous wave and transient sources. A novel modification of the Nicholson Ross Weir technique is successfully applied to both blanketed aluminum and composite fairing structures and a significant improvement in computational efficiency over the multilayered model approach is obtained. The advantages and disadvantages of using commercially available tools by incorporating Multilevel Fast Multipole Method (MLFMM) and higher order method of moments (HO MoM) to extend their application of MoM to electrically large objects is examined for each continuous wave transmission case. The results obtained with these models are

compared with those obtained using approximation techniques based on the Q factor, commonly utilized in the industry, and a significant improvement is seen in a prediction of the fields in these large cavity structures. A statistical distribution of data points within the fairing cavity is examined to study the nature of the fairing cavity field distribution and the effect of the presence of a spacecraft load on these fields is also discussed. In addition, a model with external application of Green's function is examined to address the shielding effectiveness of honeycomb panels in a fairing cavity. Accurate data for lightning induced effects within a fairing structure is not available and hence in this dissertation, a transmission line matrix method model is used to examine induced lightning effects inside a graphite composite fairing structure. The simulated results are compared with test data and show good agreement.

To my daughter
Abigail
with love

ACKNOWLEDGMENTS

TABLE OF CONTENTS

LIST OF FIGURES

xiii

LIST OF TABLES

CHAPTER 1. INTRODUCTION/LITERATURE REVIEW

Computational electromagnetic (CEM) tools are widely used in industry to determine applicable electromagnetic fields on a variety of open platforms. It is desirable to use such tools in electrically large closed volumes such as launch vehicle fairings to improve the radio frequency (RF) environment definition. Determining fairing attenuation of external electromagnetic fields and distribution of fields within the fairing cavity due to internal sources are crucial to this environment definition [1]. The launch vehicle fairing structure is a conductive enclosure made of metal or composite materials designed to protect the spacecraft from ascent environments. These fairing structures typically consist of a parabolic nose and a cylindrical core with diameters of 1 to 5 meters resulting in electrically large dimensions for typical sources at S, C and X band where the free space wavelength varies from 0.15 m to 0.03 m [2]. As computational electromagnetic (CEM) modeling tools and computer systems to evaluate these electrically large cavity structures have been unavailable, evaluating internal fairing fields have historically relied on various approximation techniques and occasional costly vehicle tests [3]. For external transmitters, handbook type algorithms to determine aperture penetration are used to determine shielding effectiveness [4,5,6]. Newer tests with less time impact based on time domain techniques have surfaced, and power balance techniques that consider the cavity resonances with an average method are also gaining popularity [7,8].   Ray tracing type algorithms have also been used to make these evaluations in some cases. In recent years, however, there is interest in more precisely determining the field distribution within the cavity and some CEM tool evaluations are being made in other industries, especially with respect to reverberation chambers [9]. Excitation of cavity modes through apertures of rectangular and

other simple structures is being examined in literature using full wave computational methods such as finite difference time domain (FDTD), finite element method (FEM), and method of moments (MoM) [9,10,11].

Launch vehicle fairings are increasingly being made of graphite composite materials because of the weight savings and strength advantages offered by these structures. RF shielding of these composite materials has been demonstrated at 40 – 100 dB for typical range transmitters (above 1 GHz) [12,13,14,15]. Extensive shielding effectiveness test programs for complex aircraft structures with composite walls are also documented [16]. Evaluating the fields due to internal transmitters in these structures has not been thoroughly investigated and literature is inconsistent regarding the protection provided by these structures to external magnetic induced effects. Internal launch vehicle (LV) layered acoustic blanketing creates an additional challenge in evaluating cavity electromagnetic environments.

It is the goal of this dissertation to build on existing techniques by providing a series of test and computational models to examine fields in launch vehicle fairings from internal and external sources. First a brief summary of cavity theory is provided followed by a summary of related approximation and CEM techniques used in industry to evaluate cavity RF environments. Next, the works evaluating material layering effects on interior cavity fields are examined, followed by those evaluating external transient sources such as lightning.

1.1   Electromagnetic Fields in the Fairing Cavity due to Internal Sources

Spacecraft or vehicle RF transmission inside a fairing cavity will excite resonant modes related to the dimensions of the structure with respect to the wavelength, λ, of the emitter frequency [17,18]. The formal general solution to the interior cavity problem is derived by Van Bladel [19]. Considering a perfect electric conductor (PEC), where the electric field will be

perpendicular to the walls, modes are excited which becomes infinite at cavity resonance. In these PEC structures, currents only reside on the surface of the wall such that no energy is dissipated in the walls [19]. For imperfectly conducting walls, the electric field will have a tangential component and currents will penetrate the walls on the order of a skin depth, δ, where $\delta = \left(\frac{2}{\omega\mu\sigma}\right)^{1/2}$, ω is the angular frequency, μ is the permeability, and σ is the conductivity of the cavity wall material. For good conductors when $\delta \ll \lambda$ (wavelength) and less than the radius of wall curvature, the fields essentially vary as a plane wave in the conductor as the derivatives of the fields in the normal direction are much larger than those in the arbitrary tangential direction [19]. Energy is dissipated in the walls thus the amplitude at resonance does not reach infinity, but is rather related to the quality factor, Q, of the cavity as shown in (1).

$$Q = \omega \frac{stored\ energy}{dissipated\ power}$$
(1)

The stored energy is related to the electric fields obtained by the boundary conditions integrated over the cavity volume. The dissipated power is related to the surface currents of the walls multiplied by the resistance in the walls. Thus it can be seen that a PEC would theoretically have no dissipated power since the walls have zero resistance resulting in an infinite Q. In general, large volumes and higher frequencies contribute to higher Q values, and dissipative materials within the cavity result in higher dissipated power and lower Q values [20].

Cavity field solutions in closed form are only possible for a few simple geometries, including canonical boundaries, where separation of variables is possible [19]. Deviation from these closed form solutions via volume perturbations or cavity loading tends to shift the frequency response [18],[21]. [18] derives the equation for change in resonant frequency due to

material perturbations using the divergence theorem. Let E_0 and H_0 be the original electric and magnetic cavity fields, E and H be the perturbed cavity fields, ω_0 the resonant frequency of the original cavity and ω the resonant frequency of the perturbed cavity, then we have

$$\nabla \times \bar{E}_0 = -j\omega_0 \mu \bar{H}_0$$

$$\nabla \times \bar{H}_0 = -j\omega_0 \varepsilon \bar{E}_0$$

$$\nabla \times \bar{E} = -j\omega(\mu + \Delta\mu)\bar{H}$$

$$\nabla \times \bar{H} = -j\omega(\varepsilon + \Delta\varepsilon)\bar{E}$$

(2)

Following application of conjugate fields, vector identities and the divergence theorem, Pozar obtains the following equation [18].

$$\frac{\omega - \omega_0}{\omega} = -\frac{\int_{V_0} (\Delta\epsilon \bar{E} \cdot \bar{E}_0^* + \Delta\mu \bar{H} \cdot \bar{H}_0^*) dv}{\int_{V_0} (\epsilon \bar{E} \cdot \bar{E}_0^* + \mu \bar{H} \cdot \bar{H}_0^*) dv}$$

(3)

To observe the fractional change in resonant frequency, ω is replaced by ω_0 in the denominator and the perturbed fields, E and H, in (3) are assumed unchanged from the original field for small changes in material and we have

$$\frac{\omega - \omega_0}{\omega_0} \cong -\frac{\int_{V_0} (\Delta\epsilon |\bar{E}_0|^2 + \Delta\mu |\bar{H}_0|^2) dv}{\int_{V_0} (\epsilon |\bar{E}_0|^2 + \mu |\bar{H}_0|^2) dv}$$

(4)

Accordingly any increase in permittivity or permeability within the cavity will decrease the resonant frequency.

Shape perturbations are similarly derived by Pozar using the additional identity from conservation of power and the assumption that the total energy stored in the perturbed cavity is approximately the same as the unperturbed cavity [18]:

$$\frac{\omega - \omega_0}{\omega_0} \cong -\frac{\int_{V_0} (\mu|\bar{H}_0|^2 - \epsilon|\bar{E}_0|^2)dv}{\int_{V_0} (\mu|\bar{H}_0|^2 + \epsilon|\bar{E}_0|^2)dv} \qquad (5)$$

These equations show that the resonant frequency of the cavity is sensitive to both shape and material perturbations in the cavity. Consequently, proper modeling of these attributes is essential to obtain an accurate result.

Numerical analysis of relatively electrically small cavities is frequently performed for devices such as the cavity backed microwave antennas [22]. Actual fairings are very electrically large where dimensions can be greater than 100 times the transmit wavelength [23]. Computational requirements for numerical analysis of this size structure are often prohibitive, particularly when lossy materials such as blanketing and composite structures are considered. Consequently, launch vehicle providers have relied on approximation techniques to predict these inner cavity fields.

1.1.1 Approximation Techniques

The most widely used method for approximating fields within a large cavity is a power balance technique described by Hill [24,25]. In this method, a shielding effectiveness approximation expression is developed for electrically large cavities based on the cavity Q. The emphasis in this technique is shielding effectiveness, but the excitations can be external or internal. Average power densities are calculated based on aperture excitation or internal excitation balanced with losses from cavity walls, apertures, antenna load resistors, and internal

loading materials[24]. Both continuous wave (CW) and pulsed sources are examined. CW signals are assumed to be steady state, however, the duration of the source with respect to the time constant is considered for pulse sources. This method of predicting average fields within a cavity is especially useful in reverberation chambers where walls are intentionally very conductive [24]. Both measurements and FDTD type full wave simulations have shown this power balance technique to be effective in predicting average field levels in highly reflective cavities, especially when probability distributions are considered [26].

1.1.2   Reverberation Chambers

Reverberation chambers are typically large metallic cavities with a metallic stirrer to generate multiple eigenmodes and maintain peak fields over a broad frequency range [27]. Reverberation chambers use the resonant behavior of structures and mode stirring to perform radiated susceptibility testing with lower average power than possible with a single antenna in free space. Statistical methods are commonly applied to determine the average or average peak field for a given power output and frequency within these structures [28,29]. Chi squared is the dominant power distribution to for these multimoded cavities [30]. Anechoic chambers are the standard test method where a single emitter is directed at the equipment under test (EUT) in an absorber lined chamber. This differs from the reverberation chamber where antennas are pointed away from the EUT with reflective walls and mode stir paddles. The statistical characterization of fields in a reverberation chamber requires error banding and uncertainty regions to compare with fields generated during anechoic chamber testing [31]. Weakly correlated results between reflective and absorbing chambers gives credence to the need to examine the applicability of such approximations to launch vehicles, which often contain RF absorbing materials.

Bunting provided one of the first CEM studies of the reverberation chamber with a two dimensional FEM approach in 1999 which found, among other results, that determining the exact E-field at a given point in the structure is not generally realistic for these stirred cavities [9], [28], [32,33]. It is desirable in these chambers to have high Q's and uniformly random fields. Any materials in the chamber will load the Q and thus decrease the chambers ability to reach the peak levels. As it is necessary for some objects such as antennas to be in the chamber, the effect of loading materials on the average field values is well studied when the load is not a significant part of the cavity volume. Mean absorption cross section formulations for even small quantities of lossy materials indicate significant impacts on average fields as a result of cavity loading [34].

Reverberation chambers, which have natural almost PEC boundaries, are often modeled using FDTD codes. In addition, the symmetry of many of these chambers allows a reduction of the model to a two dimensional analysis. For non-symmetrical cavities, this reduction in complexity cannot be made and the entire volume must be meshed. Although this method is accurate and well-defined, the frequency response from the FDTD analysis is limited by the time step. Run-times can be excessive without techniques to increase the speed of the computations [21], [35]. Johnk has recently extended typical simple structures in reverberation models to large complex structures using time domain testing with FDTD [36]. Spherical Expansion, MoM, FEM and Modal Expansion Analyses are also employed in chamber analysis [27], [34] ,[37]. Although the statistical nature of reverberation chambers with mode stirring has not been shown to emulate a spacecraft loaded launch vehicle fairing environment, the associated analyses are important to show the value of numerical methods for electrically large cavities as well as the inherent complexity of such models. In addition, the test and analysis techniques to ascertain the bounds of these reverberation chambers are a valuable comparison tool.

1.2   <u>Modeling of Layered Materials within a Fairing Cavity</u>

Acoustic and thermal ascent environments necessitate absorbing blanketing materials in the payload fairing. Electrostatic charging and radio frequency absorption requirements enforce conductivities in materials that will as a minimum bleed residual charge. One of the first works performed to understand the effects of these materials on internal fairing fields was by Hallet and Redell, who derived equivalent impedance techniques for layered materials in launch vehicle structures. Fairing fields were quantified using Poynting's theorem to solve for an equivalent wave that would dissipate the transmitted power in the surface areas of the surrounding fairing, blanketing materials and associated apertures [17]. This approximation technique is used for comparison and discussed in the Section 2.7.3.

In smaller structures, layered dielectric materials have been effectively modeled with full wave numerical codes where each material can be represented by its electrical properties and precise dimensions. Waveguide, cavity backed slots, and layered microstrip lines can effectively be analyzed with full wave simulations.   Specific absorption rate (SAR) concerns have also led to the dielectric layers of the human head to be examined by the cell phone industry [38]. However, as complexity and electrical size of the cavity increases, such a separate representation is no longer supported and an equivalent representation is needed to reduce memory and time constraints.

In recent years, interest in larger structure field prediction due to internal transmitters has been surfacing in industries such as automobiles and aircraft [39]. Cell phone usage forged the auto industry from the FM band considerations into issues with high frequency signals inside cavities [8], [40]. Many studies concerning dielectrics in automobiles, however, are concentrated in the lower frequency range [41]. Papers identifying resonances of car structures into the GHz

range using numerical methods such as MOM have concentrated on metallic surfaces only to identify resonances. However, simpler studies that show rectangular or cylindrical structures with air versus dielectric fill have shown a significant shift in resonant structures due to these dielectrics [21]. The aircraft industry has relied heavily on flight data, testing and in-flight usage restrictions to effectively control the internal cavity environment [42], [43]. Automobiles and aircraft are dominated by large apertures, however, that are not dominant in LV fairings. Active works in below deck ship environments, however, are exercising reverberation chamber techniques and ray tracing to characterize complex cavities [44].

Equivalent impedance techniques of dielectric layers are also prevalent for microstrip lines, antennas, and layered printed circuit boards. Here thin conductors and dielectrics are combined and equivalent properties are formulated based on surrounding material properties [18], [45]. Equivalent characteristic impedance and material property parameters have been developed for propagation between the layers of cylindrical and coplanar microstrips on curved structures [46].

Measurement techniques are also valuable in developing models of layered materials [47], [48]. Application of approximation and measurement techniques in a cavity with distributed fields requires careful evaluation as the dominant parameter affecting sheet impedances of thin conductors have been shown to be affected by skin depth and field distributions at the surface of the material [49]. This study evaluates the applicability of these techniques using numerical codes and testing.

1.3 Modeling of EM Fields within a Composite Fairing Cavity

The use of composite fairings is increasing in the launch vehicle industry. As discussed earlier, shielding effectiveness studies of composite structures is a topic of active research. The

focus in this study is on distribution of interior cavity fields in these composite structures due to external transient magnetic sources and internally generated electromagnetic fields.

1.3.1 Penetration of a Composite Fairing Cavity by Magnetic External Transient Fields

The primary source of external transient magnetic fields is lighting. Direct strike lightning effects are thoroughly evaluated for composite aircraft structures [50]. In the space industry, launch commit criteria and ground protection systems such as catenary wires shift the focus for launch vehicle protection to indirect effects. The payload environment in a composite fairing cavity due to lightning induced effects is not fully quantified. The effects on the spacecraft are a function of the magnitude of the magnetic field and the available loop area in payload circuitry (see Figure 1). The time varying magnetic and electric fields lead to induced voltages and currents in vehicle and spacecraft circuitry. The governing equation used to approximate the magnetic field from a nearby lighting strike ignoring ohmic losses is given by [51].

$$
\begin{aligned}
&\oint H \cdot dl = I_i + I_d \\
&= \iint_A J_i \cdot da + \iint_A \frac{\partial}{\partial t}(\varepsilon_0 E)da \\
&Where: \\
&E, H = Electric\ and\ magnetic\ fields, \\
&A, l = loop\ area\ and\ length, \\
&I, J = current\ and\ current\ density, \\
&\varepsilon_0 = permittivity\ of\ free\ space, and \\
&i, d = lightning\ source\ and\ displacement.
\end{aligned}
\tag{6}
$$
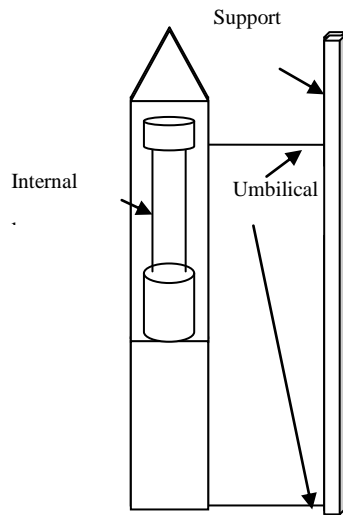
Figure 1: Typical launch vehicle with supporting structure showing umbilical and internal loops.

MIL-STD-464 quantifies the change in the electric field contributed by a near lightning strike 10 m away as 6.8 x 10^{11} volts/meter/second (V/m/s) [52]. Assuming a reasonable worst case circuit area, A, of 4 m x 0.05 m = 0.2 m^2, the contributing portion of the magnetic field due to the displacement current (I_d) is 1.2 A/m [50],[51]. This displacement current is relatively insignificant compared to the contribution of the lightning channel, allowing the magnetostatics assumptions to be applied [50], [20], [53]. Hence, a rough approximation of the magnetic field simplifies to $I_i/(2\pi r)$, where r is the distance from the strike and $2\pi r$ represents the circumference of the circle with radius, r. For instance, a 50 kA strike at 10 meters would contribute a magnetic field of 795 (amperes/meter) A/m. The rise time varies from 1.4 μs to 50 ns depending on which component of lightning is active (initial severe stroke, return stroke, multiple stroke, or multiple burst). For most launch sites, the range data includes strike magnitude and location (within a 250 to 500 meter accuracy), but does not include rise time information. MIL-STD-464 reports the change of magnetic field with respect to time for a near lightning strike 10 m away as 2.2 x 10^9

A/m/s. Using this we obtain the induced voltage that arises due to a lightning related magnetic field as [50], [52].

$$Max V_{oc} = \frac{d(\mu_0 \text{HA})}{dt} = \mu(2.2 \times 10^9)(0.2) = 552.9V \qquad (7)$$
$$Where:$$
$$\mu_0 = free\,space\,permeability = 4\pi \times 10^{-7}\,H/m.$$

The differential circuit voltage will be less than predicted by (7) due to actual circuit impedances and common mode rejection; however, the remaining voltage is undesirable for most spacecraft instrumentation cirucuits. Spacecraft retest criteria of 10 − 50 volts is common; however, lower sensitivities have been reported by design constrained spacecraft payloads [51],[54].

Early attempts at modeling this structure treated the fields as uniform [14] in a one dimensional FDTD analysis where each layer of composite slab is modeled as a homogeneous medium, characterized by constant effective conductivity and permittivity. The resulting shielding effectiveness for a 1 mm thick composite infinite panel with a conductivity of 10,000 s/m and a relative permittivity of 2 was 65 db into the 100 MHz range. A two dimensional analysis revealed less, but still significant shielding of a thinner multilayer composite panel [14]. The time domain analysis of this same study indicated significant slowing of the H field rise time inside the cavity. The case of interest to LV fairings are nearby strikes where far field assumptions may not be used and identical E and H field shielding cannot be assumed.

A combined FDTD/MFIE model was also developed for the evaluation of the fields in these composite structures due to a nearby transient source. Gaussian and Double exponential sources were used in the study. Significant attenuation by these structures was demonstrated,

however, a plane wave excitation was assumed which would not represent a lightning near field event [55]. Difficulties were discussed in using solely an FDTD method for analyzing penetration into the composite structures from external sources. Accordingly, a hybrid magnetic field integral equation (MFIE)/FDTD was developed to effectively determine the inner fields using FDTD while evaluating the external source with MFIE. Impedance boundary conditions were used to find the solution at the composite wall. The transient source was assumed to be a plane wave and the composite wall was assumed to be planar to avoid modeling issues with diffraction. Effective simulation of the composite wall by a homogeneous layer is again applied with effective comparison results to finite element source equivalent models [55]. This assumption is further supported by research of the composite structure layering and periodicity effects, which was found to be effective on layer models throughout the 100's of MHz range [56]. In addition this research found that box resonances, which were characterized by a PEC wall assumption, dominated the shielding effectiveness in a 1.2 meter enclosure at frequencies beyond 30 MHz. For lightning transients, the frequency content is low beyond 30 MHz so these resonances can be effectively ignored [57].

The diffusion of an incident magnetic field for an infinite thin metal plate is also discussed in the literature [58]. For incident pulse times shorter than field diffusion times, internal field amplitude reduction due to energy spreading in time is achieved [58].

Testing at a military lightning range of graphite composite samples typically used in launch vehicle structures revealed significant shielding to the change in magnetic field with respect to time. A lightning source was exercised directly in front of the removable panel in a metal enclosure. B-dot sensors measured the change in magnetic field within the enclosure for

each composite sample. For reference, a fiberglass panel was used to depict the absence of shielding and an aluminum panel indicated the complete enclosure shielding effectiveness [59]

These results would either indicate direct magnetic field attenuation or a slowing of the signal as the B-dot sensor measures the rate of change in the magnetic field. The rate of change in magnetic field as well as the magnitude of the magnetic field contributed to the induced voltages in circuitry [50]. However, spacecraft developers and launch vehicle providers have questioned the applicability of panel only studies to the launch vehicle fairing structure. This dissertation seeks to develop a magnetic transient shielding model based on launch vehicle composite fairing structures.

1.3.2   Modeling RF Sources within Composite Cavities

Field distribution evaluation of large composite structures has been largely reliant on test data. As testing is configuration dependent and not always feasible from a cost and schedule standpoint, techniques such as curve fitting and other approximation techniques are widely used to evaluate internal RF sources [17], [24]. GEMACS, a multi-method code developed for the Department of Defense, has been used to evaluate these structures [60]. Typically these simulations are evaluated using the Geometric Theory of Diffraction portion of this code where accuracy limitations exist. Newer full wave simulation codes are designed to model large structures of arbitrary shape using techniques to improve the computational efficiency of MoM via Fast Multipole Methods (FMM) and entire domain basis functions [61,62]. Using these available codes, combined with externally generated equivalent impedance techniques, to model the RF sources within the composite cavity is a major focus of this study.

14

1.4   <u>Summary</u>

The problem of evaluating field distributions in launch vehicle fairing cavities with internal sources is difficult and commonly encountered, but important for the spacecraft. This problem has historically not been well defined with reliance on approximation techniques and limited proprietary test data. This is because, for the frequencies of interest, the cavities are electrically very large leaving computational analysis unrealistic. Accordingly, there has been no comprehensive evaluation of these vehicle fairings with full wave computational techniques. In this dissertation, recent advances in available memory and methods to extend the frequency of existing techniques will be used to gain a better understanding of the fairing electromagnetic environment. Although most literature for very electrically large vehicles has focused on external scattering problems, there is interest in several industries to evaluate the fields within large complex cavities. In fact, during the course of this dissertation, new literature to study this problem has surfaced in defining the electromagnetic environment within electrically large cavities such as ships, aircraft and other country launch vehicles. The materials making up the fairing as well as materials within the fairing, such as graphite composite structures and acoustic blanketing materials, drive the need for equivalent models to improve the efficiency of these very large scale problems.

These radio frequency threats contributing to the electromagnetic fairing environment can be internal or external to the fairing. As some literature exists for the external threats, the primary focus of this dissertation is on internal excitation. However, with a large number of range and vehicle emitters contributing to the internal fairing environment, external sources will also be considered in terms of shielding effectiveness of fairing structures. We have also shown that lightning is also a significant contributor to the internal fairing environment. Existing

literature and industry practices regarding the shielding effectiveness of composite materials is inconsistent and further research will be shown here.

Recent advances in computational codes for large structures provide an opportunity to gain a more accurate insight into this topic using Method of Moments along with algorithms to reduce memory requirements and solution times. The major contribution of this dissertation is to provide test validated models with computational electromagnetic (CEM) codes to characterize the launch vehicle fairing environment, with metal (lined and unlined) and composite structures, due to internal and external emitters. This test anchoring is important because the electromagnetic community has historically relied on testing instead of CEM tools.

CHAPTER 2. ANALYTICAL METHODS AND COMPUTATIONAL TOOLS

The goal of this dissertation is to use computational methods to simulate internal fairing electromagnetic fields due to internal and external electromagnetic sources.   A series of theoretical and physical models are developed to thoroughly anchor the application of CEM methods discussed in this chapter to launch vehicle fairings.   These cavity models, discussed in the following chapters, include fairings with walls constructed of metal, blanketed metal, graphite composite, and metal with apertures. First, the full wave electromagnetic modeling technique used by the commercial tools is described here. Next, methods used to decrease the computational burden of the full wave technique are examined with required details of iterative and preconditioning procedures for accurate models. Finally, impedance equivalence methods are explored to further reduce model complexity. Both surface equivalent models used within computational tools and externally generated approaches are characterized. Limitations of the given modeling technique are also explored.

Since only a few simple cavities like a rectangular, cylindrical, and spherical can be solved in closed form, the cavity structure must be subdivided to apply the boundary equations to each element in a numerical solution. Although full wave techniques like MoM, FDTD, and FEM have been shown in literature to model layered small structures with accurate results, memory limitations exist for electrically large complex structures. Modifications to these baseline techniques to reduce the memory limitations are available in commercial tools. Application of these modifications to launch vehicle faring structures is new and considered in this dissertation. Since MoM is a source method based on surface and/or volume currents, only the physical structure need be meshed instead of the entire volume. As many other tools require

free space meshing which is memory intensive, the MoM derived methods are the concentration of this dissertation where high frequency considerations are important. Physical Optics is also briefly examined for applicability in cavities. Transmission Line Method is also considered for transient applications. In addition to using these CEM solvers, it is useful to modify complex layered materials in the fairing to equivalent forms. In this way, surface equivalents can be used instead of the more memory intensive volume based structures. Thin dielectric sheets, impedance sheets, thin films and distributed coatings are used to model layered structures. These equivalent surfaces alleviate the need for the mesh size to be small with respect to the thickness of the modeled material.

Previous works to determine launch vehicle internal fields have used simplified ray tracing techniques, system testing based curve-fitting equations, or approximation techniques discussed in 1.1.1. In this dissertation, full-wave based techniques are used to determine these internal fields in complex fairing structures. These full wave techniques and equivalent material models are evaluated and comparisons to existing approaches are made. This is important because spacecraft developers require accurate environment definition for sensitive spacecraft, and there is no current industry standard for predicting this internal environment.

There are two commercial codes considered here that specifically deal with complex large structures for electromagnetic problems: EM Software Systems, FEKO, and WIPL-D, 3D EM solver. Both have techniques for optimizing the MoM method for large complex structures. MultiLevel Fast Multipole Method (MLFMM) is the primary technique used in this study with FEKO, and entire domain\higher order basis functions with MoM are the focus for WIPL-D. Another CEM solver, CST Microstripes, optimized for time domain with the transmission line matrix (TLM) method is adopted for transient analysis. Although not required for general

default setting operation of these codes, advanced setting options such as solution selection, equivalent surfaces, iteration convergence criteria, and alternate meshing require a thorough understanding of the underlying electromagnetic theory to realize accurate models. Hence, the core methods used in these tools are described in this chapter.

The Method of Moments is discussed in Section 2.1. This technique is beneficial computationally for cavities where a large portion of the volume is empty. Limitations with MoM for electrically large structures remain and modifications to this technique must be made to solve these complex problems. MLFMM, which divides the space into near and far interactions to save memory and reduce solution time, is used in conjunction with MoM. The MLFMM method is discussed in Section 2.2. A description of MoM with higher order basis functions is provided in Section 2.3. Physical Optics is used for comparison and is briefly described here along with various applicable approximation techniques. TLM techniques are then examined for application to lightning induced effects. Existing equivalent impedance models used in this dissertation are also described here. Modifications to these models are described as they are needed for the determination of the field distributions.

2.1   Method of Moments (MoM)

The focus of this dissertation is on computationally efficient methods to determine fields in electrically large fairing structures. In both of the major models implemented, MLFMM and higher order method of moments, MoM is the core method, which is modified to achieve computational efficiency. In this section, the MoM and its application to electromagnetic scattering are delineated. Basis functions adopted by the commercial tools, which are important to meshing criteria, are also examined. In addition the matrix solver is briefly described for later reference.

The MoM process involves first discretizing the structure into segments that are typically small with respect to the wavelength of the frequency of interest. Next, the unknown currents on the structure are represented by basis functions. Weighting functions are then selected to test the solution. Finally, the matrix is solved to determine the current distribution which is used to determine other desired parameters such as fields [63]. This process of taking moments or multiplying by weighting functions begins with linear mathematical equations in the form shown [63,64,65].

$$L\Phi = g \tag{8}$$

where L is a linear operator, g is the known excitation and Φ is the unknown function. Solving this equation for each element of the mesh and approximating the unknown function leads to a set of linear equations. Approximation of this unknown is based on mesh parameter functions called basis functions, u_n formulated in [64] and shown below

$$\widetilde{\Phi} \approx \sum_{n=1}^{N} a_n u_n \tag{9}$$

where a_n are the expansion coefficients and N is the number of unknown coefficients. Since g, is the known source, it can be used to ascertain the accuracy of the approximation with the goal of making the linear operation on these functions equal to the source.

$$L\Phi \approx g \tag{10}$$

The amount of residual, R, in the approximation is related to the error and can be determined by substituting into the operator equation.

$$R = L(\widetilde{\Phi} - \Phi) = L\widetilde{\Phi} - g \tag{11}$$

In the weighted residual method, the weighting functions w_m are chosen such that the integral of a weighted residual of the approximation is zero [64].

$$\int w_m R dv = 0$$

$$< w_m, R > = 0$$

(12)

If a set of weighting functions $< w_m, R >$ are chosen and the inner product is taken for each function, w_m, we obtain

$$\sum_{n=1}^{N} a_n < w_m, Lu_n > = < w_m, g > , \quad m = 1, 2, \dots N$$

(13)

This system of linear equations can be cast in matrix form as

$$[A][X]=[B]$$

Where $A_{mn} = <w_m, Lu_n>$, $B_m = <w_m, g>$, and $X_n = a_n$.

(14)

Solving for [X] and substituting for a_n in the Φ approximation gives an approximate solution for to (8) [64].

2.1.1 MoM applied to Electromagnetic (EM) Scattering

When MoM is applied to electromagnetic problems the integral operator equations are derived from Maxwell's equations. The primary method is to find induced currents on conductive structures so that the scattered fields can be predicted. The EM fields are calculated based on integral equations developed from the source and boundary conditions at the scattering object [66]. The integral equation (IE) is converted to a set of matrix equations using basis and weighting functions [64]. The matrix equations will have the form:

$$[Z][I] = [V]$$

(15)

where Z is the impedance matrix, [V] is the known source voltage and [I] represents the induced currents that are approximated [64]. Equivalent electric $\vec{J}_s$ and magnetic $\vec{M}_s$ surface current densities generated from the surface equivalence principle (SEP) are needed to account for discontinuities of the tangential fields at scattering boundaries as shown in Figure 2.
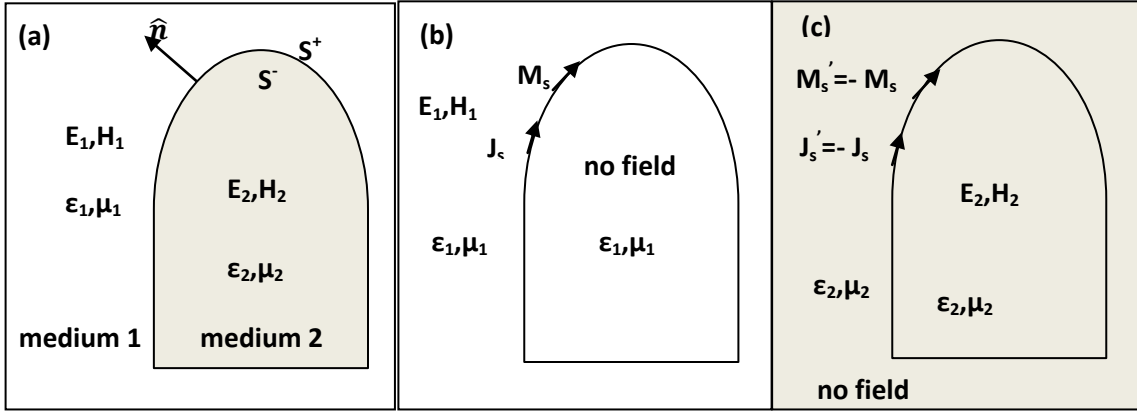
Figure 2. Dielectric body in a homogeneous environment (a) original (b) external (c) internal equivalent problems [67].

The electric fields in the internal or external area can be obtained by determining the field produced by a surface magnetic or electric current that produces the same field as the original problem. The original homogeneous problem fields in part a of the external region 1, or the internal region 2, are a result of the superposition of source and scattered and fields

$$\vec{E} = \vec{E}_i + \vec{E}_s$$

(16)

$\vec{E}_i$ is the field due to an impressed source in the absence of the scatterer

$\vec{E}_s$ is the scattered field [68].

To determine the scattered field, the equivalent problems shown in parts b and c are considered. Here the surface current densities based on the incident fields are substituted for the original fields as delineated in reference [67]

$$\vec{J}_s = n \times \vec{J}_{s_0} = -j\omega_0\mu\vec{H}_0$$

$$\vec{J}_s = \hat{n} \times \vec{H}_1(S^+) = \hat{n} \times \vec{H}_2(S^-)$$ (17)

$$\vec{M}_s = -\hat{n} \times \vec{E}_1(S^+) = -\hat{n} \times \vec{E}_2(S^-)$$

where the time dependency of $e^{j\omega t}$ is assumed, $\hat{n}$ is the unit normal directed from region 1 to region 2, and S^+ and S^- are the exterior and interior surfaces. The specific EM fields for each region according to [67] and [66] are given by

$$\vec{E}_1 = \vec{E}_{i,1} + \vec{\mathcal{E}}_{1,\vec{J}_s} + \vec{\mathcal{E}}_{1,\overline{M}_s}$$

$$\vec{H}_1 = \vec{H}_{i,1} + \vec{\mathcal{H}}_{1,\vec{J}_s} + \vec{\mathcal{H}}_{1,\overline{M}_s}$$

$$\vec{E}_2 = \vec{E}_{i,2} - \vec{\mathcal{E}}_{2,\vec{J}_s} - \vec{\mathcal{E}}_{2,\overline{M}_s}$$ (18)

$$\vec{H}_2 = \vec{H}_{i,2} - \vec{\mathcal{H}}_{1,\vec{J}_s} - \vec{\mathcal{H}}_{1,\overline{M}_s}$$

Thus, the total fields in the region are a result of the incident field in that region plus the scattered field due to the currents generated from the incident field. For the region of interest, the scattered fields are represented by:

$$\vec{E}_s = \vec{\mathcal{E}}_{\vec{J}_s}\{\vec{J}_s\} + \vec{\mathcal{E}}_{\overline{M}_s}\{\vec{M}_s\}$$ (19)

with $\mathcal{E}$ and $\mathcal{H}$ representing operator notation. For example $\vec{\mathcal{E}}_{\overline{J_s}}$ is the operator notation for Green's functions and surface current expressions [67], [19]

$$\vec{\mathcal{E}}_{\overline{J_s}}\{\vec{J_s}\}(r) = -j\omega\mu\left[\vec{I} + \frac{\nabla\nabla}{\beta^2}\right]\iint_{A'} J_s\left(r'\right)G(r,r')\,dA'$$

(20)

where the propagation constant, $\beta = \omega\sqrt{(\mu\varepsilon)}$ and $G(r,r')$ is the Green's function

$$G(r,r') = \frac{e^{-j\beta|r-r'|}}{4\pi|r-r'|}$$

(21)

When the surface is a PEC , $E_{tan}= 0$ leading to

$$\vec{E}_{s,tan} = -\vec{E}_{i,tan}$$

(22)

Substituting into (19) we have the electric field integral equation (EFIE) for PEC structures.

$$\left(\vec{\mathcal{E}}_{\overline{J_s}}\{\vec{J_s}\}\right)_{tan} = -\vec{E}_{i,tan}$$

(23)

The electric field integral equation is used by default for all MoM and MLFMM computations in FEKO and for higher order MoM computations in WIPL-D. The EFIE has a null space solution for external excitation even on a PEC boundary with no internal sources due to the non-trivial solution of the zero boundary condition at resonance [69].

This can be seen by examining the standard integral scattering equation for fields incident on a closed boundary with a homogeneous Dirichlet boundary condition considering an external region V_1 as in (24).

$$\varphi_{inc}(r) = \int_S dS' \, G_1(r,r') \, \partial_{n'} \varphi_1(r'), \quad r \in S \tag{24}$$

Now, if the source is placed directly on the boundary S filled with a medium with wave number k_1 in internal region V_2 [69] shows that the external region fields and Green's function apply to the inside because of the wave number k_1.

$$\varphi_1(r) = \int_S dS' \, G_1(r,r') \, \partial_{n'} \varphi(r') - \varphi_1 \, \partial_{n'} G_1(r,r'), \quad r \in V_2 \tag{25}$$

For closed regions with $\varphi_1(r) = 0$ boundary conditions for $r \in S$, then (25) becomes (26).

$$0 = \int_S dS' \, G_1(r,r') \, \partial_{n'} \varphi(r'), \quad r \in S \tag{26}$$

This in turn has a non-trivial solution for internal cavity resonant frequencies [69]. The integral operator in (26) becomes that in (24). Accordingly, the scattering equation (24) has a null-space solution at cavity internal resonant frequencies [69].

Numerical discretization errors can lead to this interior resonance being spread over a wider frequency range [66]. To determine fields with closed PEC structures a combined integral

equation (CFIE) can be selected which adds the magnetic field integral equation (MFIE) shown below

$$\vec{H} = \vec{H}_i + \vec{H}_s$$

$$\vec{H}_s = \mathcal{H}_{\overline{J}_s}\{\vec{J}_s\}$$

(27)

Again $\mathcal{H}_{\overline{J}_s}$ is the linear operator notation defined as

$$\mathcal{H}_{\overline{J}_s}\{\vec{J}_s\}(r) = \frac{1}{4\pi}\nabla \times \iint_{A'} J_s(r')\frac{e^{-j\beta|r-r'|}}{r-r'} \, dA'$$

(28)

When the CFIE is exercised a weighting constant related to the intrinsic impedance is needed to equalize the electric and magnetic field contributions to the equation [66]. In effect, the CFIE can be implemented as αEFIE + $(1 - \alpha)(j/\beta)$MFIE and the null space solution avoided by the careful choice of α (from 0 to 1). The resulting resonance is complex and thus the interior resonant condition is not valid for any real frequencies [69]. Since the MFIE is only valid for closed structures, the CFIE also has this constraint. Another possibility to obtain a unique solution, although computationally expensive, is to fill the cavity with a dielectric medium as dielectrics solutions employee the PMCHW by formulation (named after the developers of the formulation Poggio, Miller, Chang, Harrington, and Wu) [71],[66]. This dielectric solution uses combined internal and external EFIE and combined internal and external MFIE equations together in the MoM matrix to avoid internal resonance [69]. Use of these techniques for mitigating the issue of artificial interior resonances is discussed in this dissertation when considering shielding effectiveness of fairing structures. Other integral equation formulations exist to eliminate the interior resonance issue, however EFIE is still the most commonly used

equation in existing CEM tools and mitigation strategies for internal resonance issues within this method are needed [72].

When conductive structures that are not perfect electric conductors are modeled, equivalent surfaces are developed. This procedure is described in Section 2.7.

2.1.2 Rao, Wilton and Glisson (RWG) Basis Functions

For the general EFIE formulation, the following expansion function is used. Thus the total current for each element is based on the sum:

$$\vec{J}_s = \sum_{n=1}^{N_J} \alpha_n \cdot \vec{f}_n \tag{29}$$

where fn is the basis function and N_J is the number of basis functions and unknown coefficients.

In FEKO the Rao, Wilton and Glisson (RWG) basis functions utilizing triangular patches are used. This vector based function enforces the current continuity over the edge of the patch via interpolation. The function according to reference [73] is given in (30).

$$\vec{f}_n(\vec{r}) = \begin{cases} \dfrac{l_n}{2A_n^+} \vec{\rho}_n^+ & r \ in \ T_n^+ \\ \dfrac{l_n}{2A_n^-} \vec{\rho}_n^- & r \ in \ T_n^- \\ 0 & otherwise \end{cases} \tag{30}$$

The basis function is defined over two adjoining triangles, T_n^+ and T_n^- which share a common edge. The normalizing constants are $\dfrac{l_n}{2A_n^+}$ and $\dfrac{l_n}{2A_n^-}$ with A_n representing the area of triangle T_n and l_n representing the length of the shared edge as seen in Figure 3. The position vector $\vec{\rho}_n^+$ is defined with respect to the free vertex of T_n^+.
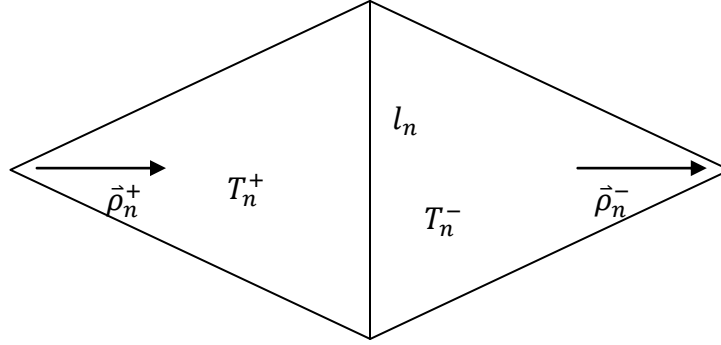
Figure 3. RWG basis element.

This approximated EFIE is converted to a system of linear matrix equations obtained using a scalar product of the basis and testing functions.

$$< \vec{h}, \vec{w}_m > = \iint_A \vec{h} \cdot \vec{w}_m dA \qquad (31)$$

Suitable testing or weighting functions, w_m, are the current expansion functions based on the Galerkin method where the weighting and basis functions are the same [73]. Substituting the field quantities in (23) and (29) the matrix is filled as follows.

$$\sum_{n=1}^{N_J} \alpha_n \cdot < \vec{\mathcal{E}}_{\overline{J}_s}\{\vec{f}_n\}_{tan}, \vec{w}_m > = - < \vec{E}_{i,tan}, \vec{w}_m > \qquad (32)$$

This basis expansion method with meshing constraints provides an accurate representation of EM scattering structures. Since the RWG basis function relies on linear elements, it is necessary that the solution changes minimally over the dimensions of the mesh element. The default mesh size in FEKO is $\lambda/8$, and model precision is added by decreasing the mesh size to smaller values at some memory cost [74]. For metal structures the referenced

wavelength is that of the propagating media (usually air) and for dielectrics, the wavelength is associated with that of the dielectric media. Memory and solution time required is intensive when solving electrically large complex structures, hence alternative approaches are often required.

2.1.3 Lower Upper (LU) decomposition

Following the development of basis function to form linear equations, the impedance matrix is solved for the unknown current coefficients α_n. LU decomposition, employed in FEKO, is a method of factorizing the matrices such that the right hand vector is not changed as is the case in Gaussian elimination [75]. Considering the standard matrix equation, [A][X] = [B], the matrix A can be subdivided into an upper, U, and lower, L, matrix as LU = A. The process of LU decomposition according to [75] is provided below as this method is modified as a preconditioner (Section 2.2.3.1) for reducing computational time in determining fairing fields.

$$A \cdot X = (L \cdot U) \cdot X = L \cdot (U \cdot X) = B \tag{33}$$

First,

$L \cdot Y = B$ is solved by forward substitution $y_1 = \frac{b_1}{l_{11}}$

$$y_i = \frac{1}{l_{ii}} \left[b_i - \sum_{k=1}^{i-1} l_{ik} \, y_k \right] \quad i > 0 \tag{34}$$

Similarly, $U \cdot X = Y$ where X is obtained by backward substitution $x_{n1} = \frac{y_n}{u_{mn}}$

$$x_i = \frac{1}{u_{ii}} \left[y_i - \sum_{k=i+1}^{N} u_{ik} \, x_k \right] \quad i < N \tag{35}$$

29

The method of moments has been proven to provide results consistent with analytical results in closed formed solutions [65]. However, the computational expense of this matrix solution process necessitates modifications for many electrically large structures [61].

2.2   Multilevel Fast Multipole Method (MLFMM)

MLFMM is the proposed method for modeling the internal cavity fields, which is an alternative formulation of the MoM that is applicable to large structures. This method introduces a controllable error which typically requires outer iterations to keep the solution within acceptable error limits. MLFMM is similar to standard MoM in that basis functions model the interaction between all the patches. With MLFMM, however, basis functions are grouped and interaction between groups are computed which saves computational resources [76]. MLFMM divides three dimensional structures into boxes which are further subdivided until only a small number of basis functions remain. The computational savings in memory and solution time are depicted in Table 1.

Table 1: Solution Time and Memory Comparison for MoM/MLFMM

Method	MoM	MLFMM
Solution Time	N^3	$N_{iter} N \log(N)$
Memory Usage	N^2	$N \log(N)$

N is the number of unknowns in the matrix system and N_{iter} is the number of iterations in the iterative solver [61].

The domain is divided into near and far interactions based on the relationship of the mesh cells with their neighbors. Boxes are further divided in a hierarchical fashion divided into 8 sub-boxes [77]. In FEKO the smallest box size is 0.23 λ, however this parameter is adjustable. Only

immediate mesh neighbors (near field) interactions are calculated with MoM basis and weighting functions. All other neighbors are calculated with a far field interaction [77]. This near and far field definition is based on proximity in the mesh, but is distinct from the near and far field distances of an electromagnetic source such as a transmit antenna [78].

First, the single fast multipole method (FMM) is examined for insight. The potential expansions can be written fully when a central point is introduced. Using the addition theorem, the basis, considering a one dimensional Gaussian Function which is regular everywhere, can be rewritten as described in [79]

$$\Phi(y, x_i) = e^{\frac{-(y - x_i)^2}{h^2}} \tag{36}$$

where x_i are source points and y_j are target points.
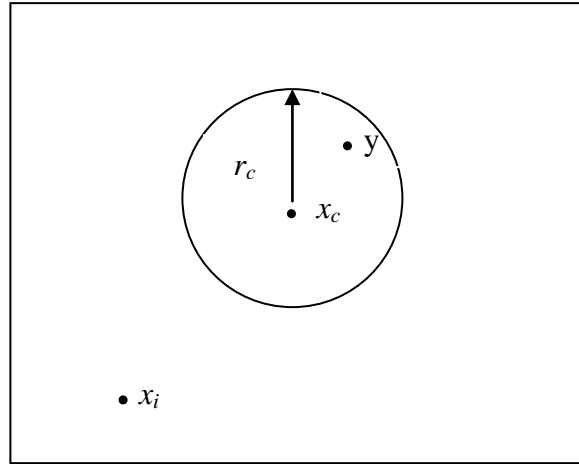
Figure 4. Near Region.

For any y and $x_c \in \mathbb{R}$; $\|y - x_c\| < r_c < \infty$, where r_c is the near field radius (Figure 4), the expansion can be written in the form below [61].

$$\Phi(y, \text{x}_i) = e^{-\frac{[(y-x_c) \ -(x_i-x_c) \ ]^2}{h^2}}$$

(37)

$$= e^{\frac{-(y-x_c)^2}{h^2}} e^{\frac{-(x_i-x_c)^2}{h^2}} e^{\frac{2(y-x_c)(x_i-x_c)}{h^2}}$$

Using a Taylor Series, the expression becomes

$$e^{\frac{-(y-x_c)^2}{h^2}} e^{\frac{-(x_i-x_c)^2}{h^2}} \sum_{m=0}^{\infty} \frac{2^m}{m!} \left(\frac{y-x_c}{h}\right)^m \left(\frac{x_i-x_c}{h}\right)^m$$

(38)

which leads to a separable expression

$$\sum_{m=0}^{\infty} \left[\frac{2^m}{m!} e^{\frac{-(x_i-x_c)^2}{h^2}} \left(\frac{x_i-x_c}{h}\right)^m\right] e^{\frac{-(y-x_c)^2}{h^2}} \left(\frac{y-x_c}{h}\right)^m$$

(39)

expressed as

$$\sum_{m=0}^{\infty} a_m(x_i, x_c) \, R_m(y - x_c)$$

where

$$a_m(x_i, x_c) = \frac{2^m}{m!} e^{\frac{-(x_i-x_c)^2}{h^2}} \left(\frac{x_i-x_c}{h}\right)^m$$

$$R_m(y - x_c) = e^{\frac{-(y-x_c)^2}{h^2}} \left(\frac{y-x_c}{h}\right)^m$$

Thus a source and target point can be separated when a central point and infinite series are used. The central point can then be used to translate interactions between near and far regions through the use of translation. As the infinite series cannot be realized, truncation of this series is performed and an error introduced as shown in an example from [79].

$$v_j = \sum_{i=1}^{N} q_i \, \Phi(y, x_i)$$

$$= \sum_{i=1}^{N} q_i \sum_{m=0}^{\infty} a_m(x_i, x_c) \, R_m\left(y_j - x_c\right) \quad\quad (40)$$

$$= \sum_{i=1}^{N} q_i \sum_{m=0}^{p-1} a_m(x_i, x_c) \, R_m\left(y_j - x_c\right) + \text{error}(p, x_i, y_j, x_c)$$

Where p is the truncation number chosen based on the desired error. Ignoring the error term,

$$v_j = \sum_{m=0}^{p-1} \left[\sum_{i=1}^{N} q_i \, a_m(x_i, x_c) \right] R_m\left(y_j - x_c\right)$$

$$v_j = \sum_{m=0}^{p-1} A_m \, R_m\left(y_j - x_c\right) \quad\quad (41)$$

Where $A_m = \sum_{i=1}^{N} q_i \, a_m(x_i, x_c)$, which depends only on the source and can be computed in one pass for different m.

Further, to reduce both the error and the number of terms required by a single central point, the regions are subdivided so that interactions to a central point in one region are calculated and then interactions between regions are calculated based on these central points. To illustrate this concept two central points are considered.

Let $\{F_n(y - x_{c1})\}_{n=0}^{\infty}$ and $\{G_m(y - x_{c2})\}_{m=0}^{\infty}$ be two sets of basis functions centered at x_{c1} and x_{c2} such that $\Phi(y, x_i)$ can be represented by two uniformly and absolutely convergent series as [79].

33

$$\Phi(y, x_i) = \sum_{n=0}^{\infty} a_n(x_i, x_{c1}) F_n(y - x_{c1}), \qquad \forall y \in \Omega_1 \subset \mathbb{R}^d$$

$$\Phi(y, x_i) = \sum_{m=0}^{\infty} b_m(x_i, x_{c2}) G_m(y - x_{c2}), \qquad \forall y \in \Omega_2 \subset \Omega_1$$

(42)

Where Ω_1 and Ω_2 are domains of y.

The potential can be fully defined by either set, so these expressions are set equal and a translation operator that relates the two sets of coefficients is formulated in [68].

$$\{b_m(x_i, x_{c2})\} = (F|G)(t)\{a_n(x_i, x_{c1})\}, t = x_{c2} - x_{c1}$$

(43)

Thus *t* is an expression that relates the two center points of regions 1 and 2.

The computational benefit can be seen by the number of interactions that are saved by translating to central points as shown in the simplified diagram in Figure 5 below [80].
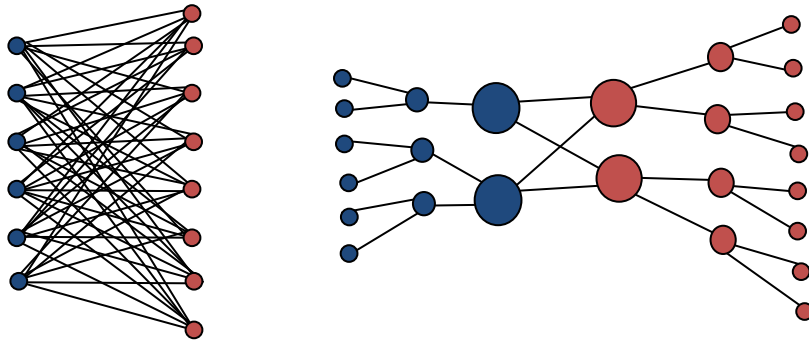
Figure 5. Interactions in standard MoM and MLFMM.

2.2.1   MLFMM applied to EM Scattering

To implement MLFMM for complex scattering problems, a dynamic 3-D scalar Green's function is used for the expansion function as expressed in [81].

$$\frac{e^{-jk|r+d|}}{4\pi|\boldsymbol{r}+\boldsymbol{d}|} = ik\sum_{l=0}^{\infty}(-1)^l(2l+1)j_l(kd)h_l^{(1)}(kr)\,P_l(\hat{d}\cdot\hat{r})$$

$$(44)$$
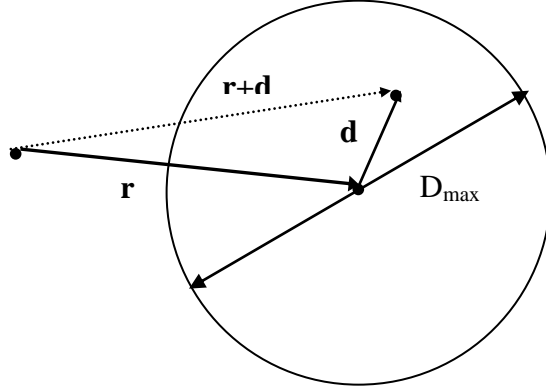
Figure 6. Vector definitions for expansion function [82].

Where k is the wavenumber, j_l is the spherical Bessel function of the first kind, $h_l^{(1)}$ is a spherical Hankel function of the first kind, P_l is a Legendre polynomial, $\boldsymbol{r}$ and $\boldsymbol{d}$ are two vectors, r and d are their amplitudes with d < r, and $\hat{d}$ and $\hat{r}$ are their unit vectors, respectively (see Figure 6). In this paper $e^{j\omega t}$ time convention is used [81]. The truncated series is shown in (45).

$$\frac{e^{-jk|r+d|}}{4\pi|\boldsymbol{r}+\boldsymbol{d}|} \approx ik\sum_{l=0}^{L}(-1)^l(2l+1)j_l(kd)h_l^{(1)}(kr)\,P_l(\hat{d}\cdot\hat{r})$$

$$(45)$$

The choice of the truncation variable is key to optimizing the computational savings inherent in this method while maintaining acceptable error. In general L varies as a function of r/λ and d. When d increases, the number of modes L required to maintain the same accuracy increases. For example, an empirical formula for less than 0.1 relative error, according to reference [81], is:

$$L = kd + \ln(\pi + kd) \tag{46}$$

The formula was refined in [83] by deriving the individual contributions of the Green's function truncation as

$$\epsilon = kR \sum_{l=L+1}^{\infty} (-1)^l (2l+1) j_l(kd) h_l^{(1)}(kr) P_l(\hat{d} \cdot \hat{r}) \tag{47}$$

where ϵ is the relative error and $R = r + d$.

This work showed a dependence of the error for a given L on R. The error is maximum when r and d are collinear. The spherical Hankel function contribution is found by examining the large argument approximation

$$\tag{48}$$
$$\epsilon \approx (2L+3) j_{L+1}(kd)$$

and the Bessel function contribution decreases with increasing arguments,

$$\epsilon \approx (2\delta)^{-1/4} e^{-kd \frac{(2\delta)^{3/2}}{3}} \tag{49}$$

where $\delta \approx 1.8 \left[\frac{\log\left(\frac{1}{\epsilon}\right)}{kd} \right]^{2/3}$

The final refined truncation variable, L, is now given by

$$L \approx kd + 1.8 d_0^{2/3} (kd)^{1/3} \tag{50}$$

where d_0 represents the required digits of accuracy.

The translation expression is derived using the identity

$$4\pi i^l j_l(kd) P_l(\hat{d} \cdot \hat{r}) = \int d^2k \, e^{-ikd} \, P_l(\hat{k} \cdot \hat{r}) \tag{51}$$

The expansion can be written in an integral form [81]

$$\frac{e^{-ik|r+d|}}{4\pi|\boldsymbol{r}+\boldsymbol{d}|} \approx ik\int d^2\hat{k}e^{-ikd}\,T_L(kr,\hat{k}\cdot\hat{r})$$

(52)

with the translation expression given below.

$$T_L\big(kr,\hat{k}\cdot\hat{r}\big) = \sum_{l=0}^{L} i^l(2l+1)h_l^{(1)}(kr)\,P_l(\hat{k}\cdot\hat{r})$$

(53)

To decrease the truncation error, L should be very high, however, the Hankel functions diverge for large arguments as L goes to infinity. This instability is caused by the exchange of summation and integration that is introduced by using the identity (51) in (45) [69]. Considering Figure 6, it has been shown for open structures for a given truncation variable, L, and a given distance within the circle, d/λ = 0.4 for example, that the truncation error decreases as r/λ increases in the nearer regions settling to a nearly constant error (at approximately r/λ = 2 for this case) [81]. It makes sense that the error would decrease for further r values as the interactions are further apart and would intuitively contribute less to the solution at a given location. After a certain distance is reached the interactions are far away and no further benefit to an increasing r distance is seen. However, for cavity structures, contributions to fields are less dependent on distance and more dependent on the eigenmodes in the cavity due to the boundary conditions in the overall structure. The applicability of MLFMM to these cavity structures is examined in this dissertation.

As can be seen, the use of MLFMM for complex structures requires a truncation of the translation expression series. To reduce the error that this introduces iterative techniques are introduced to achieve the desired accuracy with acceptable solution times. In addition,

preconditioners are applied at each iteration to improve the efficiency of the solutions. These combined techniques help reduce the computational expensive standard LU decomposition to a reasonable process. Within FEKO, the convergence criteria, and thus the allowable error, can be manipulated along with preconditioner selection. It is important to understand these parameters prior to altering default setting in FEKO.

2.2.2 Krylov Iterative Methods

Since MLFMM is an approximation of MoM an iterative method is combined with MLFMM to reduce the residual error to acceptably low levels. In FEKO the default level is 0.003 and can be adjusted by the user [74]. When determining the eigenvalues for large sparse matrices, iterative methods are applied to employ the more efficient vector by matrix multiplications rather than the time consuming matrix by matrix operations. Although the Green's function decays rapidly and most of its entries are in the near part of the matrix, the exact inverse of the impedance matrix can be dense [84]. To handle this, several Krylov sub-space iterative methods are used for MLFMM solutions. There is a trade off within these techniques between computations required per iteration and the speed of convergence which reduces the number of iterations. Most of these methods are a modification of Biconjugate Gradient (BCG) with additional matrix-vector multiplications applied instead of a matrix transpose. The utility of this approach can vary from problem to problem depending on the A matrix, thus a Krylov subspace provides optimal iterative and preconditioning method selection with each iteration [85]. Considering the linear matrix equation, Ax = b, an approximate solution, x_m, is desired. The Krylov subspace methods are iterative methods that search for the solution at the m_{th} iteration [86]. The Krylov subspace κ_{m} is written as

$$\kappa_m(A, r_0) \equiv span\{r_0, Ar_0, A^2 r_0, ..., A^{m-1} r_0\}$$

$$(54)$$

where $r_0 = b - Ax_0$ is the associated initial residual vector [85]. An important aspect of the Krylov subspace is its approximation of the A matrix inverse in the form

$$A^{-1} b \approx \quad x_m = x_0 + q_{m-1}(A) r_0$$

$$(55)$$

where q_{m-1} is a certain polynomial of degree m-1. When $x_0 = 0$, the simple formulation becomes.

$$A^{-1} \quad b \approx x_m = \quad q_{m-1}(A) b$$

$$(56)$$

The choice of the subspace, $\mathcal{L}_m$, and the preconditioning technique give rise to the varying forms of these Krylov methods. The first and simplest techniques are based on $\mathcal{L}_{m=} \kappa_m$. A minimum-residual variation is $\mathcal{L}_m = A\kappa_m$. The second class of techniques is based on modifying $\mathcal{L}_m$ to be a Krylov subspace method associated with A^T, in which $\mathcal{L}_{m=} \kappa_m(A^T, r_0)$ [85]. The Krylov subspace methods specifically employed by FEKO are the Generalized Minimal Residual Method (GMRES) , which is a minimum residual method. The other Krylov methods in FEKO are the Biconjugate Gradient Stabilized (BiCGStab) and Transpose Free Quasi-Minimal Residual (TF-QMR), which are based on the second class described above, except that again these techniques modify the matrix manipulation such that the additional matrix vector multiplications are made to eliminate the transpose operation as below [76], [85].

$$\kappa_m(A, v) \equiv span\{v, Av, A^2 v, ..., A^{m-1} v\}$$

$$(57)$$

It can be seen that starting with the vector v, Av is computed, subsequently the resulting vector is multiplied by A to obtain A^2v. This process continues until the desired operations are formed, albeit the dimension of the subspace increases with each approximation process.

2.2.3   Preconditioning Techniques

Preconditioning the sparse matrix within each iteration is important to reduce required computational resources and promote convergence [85].   In general, preconditioners use multipliers in the matrix equation to improve numerical stability and thus convergence as

$$M^{-1}Ax = M^{-1}b$$

(58)

The solution is unchanged, but $M^{-1}A$ can be made to be more attractive in an iterative solver. M^{-1} should be selected to have reasonable set-up time, memory demand, and overhead [75].

Block Jacobi is the simplest preconditioner and corresponds to the diagonal of the A matrix [85]. FEKO exercises Block Jacobi when the CFIE can be applied which is optimal for closed PEC structures. More complex preconditioners are needed with EFIE solutions to achieve convergence. The two choices of preconditioners in FEKO are incomplete LU Factorization and sparse approximate inverse [76].

2.2.3.1 Incomplete LU factorization (ILU)

In this method an incomplete factorization of the original matrix A is performed as compared to the standard LU decomposition described in Section 2.1.4.   The matrix is made sparse before LU decomposition such that only interactions near the diagonal of the matrix are considered. FEKO utilizes a modification of this method that allows some level of fill in L and

U up to the user selected value with a maximum of 12 [74]. The level of fill is otherwise established by the program using conditional algorithms based on the matrix multiplications.

Numerical issues can be encountered with ILU because of the indefinite EFIE matrix [84]. This indefinite solution is more easily understood by considering the differential form of the Helmholtz equation in (59).

$$(\nabla^2 + k^2)\varphi(\boldsymbol{r}) = s(\boldsymbol{r})$$

(59)

Where k^2 is positive definite and the Laplacian operator is negative definite, leading to the resulting operator to be indefinite for closed regions with Neumann or Dirichlet boundary conditions. The resonances with zero eigenvalues cause this indefiniteness. Hence, iterative solutions will have difficulty converging close to the resonant frequencies [69].

Limiting the interactions considered to near the diagonal, introduces error into the solution with the error term of the form $A = LU + E$, where E is the residual error. Following preconditioning the form becomes

$$L^{-1}AU^{-1} = I + L^{-1}EU^{-1}$$

(60)

Thus the inverse of the upper and lower matrices are also multiplied by the error term which depends on how diagonally dominant the original matrix was. Large perturbations in the identity matrix can occur when the matrix is not diagonally dominant [85]. This numerical problem is particularly an issue when the operations are divided over multiple processors. Accordingly, ILU is the default preconditioner for single processor operations only in FEKO [74].

2.2.3.2 SParse Approximate Inverse (SPAI)

To alleviate this error, it is desirable to find a preconditioner that does not require solving a linear system. The original system can be preconditioned by a matrix M which is a direct approximation of the inverse A [85]. One such method is referred to as the SParse Approximate Inverse (SPAI) where there is active research regarding its application to most efficiently promote convergence of the solutions of interest. The focus of this dissertation evaluation of MLFMM is for large systems where multiple processors are needed, and SPAI is the preconditioning technique applied by the CEM tool when multiple processors are utilized. With SPAI, the accuracy of the approximated inverse, M, is ascertained by minimizing the Frobenius Norm, F(M), of the residual matrix, $I - AM$, as given in (61) [85].

$$F(M) \ = \ ||I - AM||_F^2$$

(61)

This method provides the added advantage that F(M) can be found directly as in (61) or by finding the 2-norm of the individual columns of the residual matrix as in (62),

$$F(M) \ = \ \left||I - AM\right||_F^2 = \sum_{j=1}^{n} \left||e_j - Am_j\right||_2^2$$

(62)

in which e_j and m_j are the jth column of the identity matrix and of the matrix M, respectively [85]. Consequently, the overall norm is minimized when the 2-norm is minimized as in (63) for each column [85].

$$f_j(m) \ = \ \left||e_j - Am_j\right||_2^2, j = 1, 2, \dots, n$$

(63)

The advantage of SPAI for parallelization is the individual rows of the pre-conditioning matrix can be obtained independently from each other. As data in the neighboring rows and

columns are required, FEKO stores the data from these neighboring rows locally to keep processor to processor interaction to a minimum [77].

2.2.4 MLFMM implementation in FEKO summary

Step 1: The mesh is created to discretize the problem.

Step 2: The hierarchical tree structure is created as shown in Figure 7 [80]. The parent box contains 8 smaller boxes or elements with the smallest size default box size of 0.23λ.
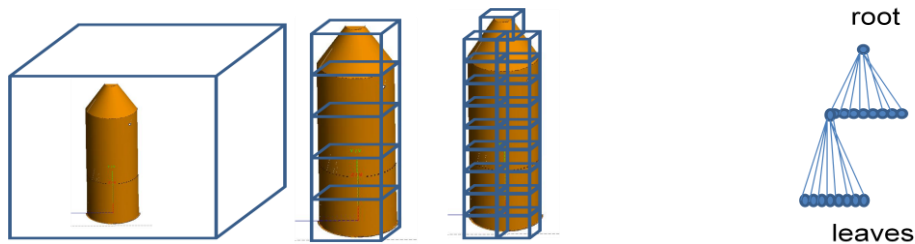
Figure 7 MLFMM processes (boxing, roots, and leaves).

Step 3: Near Field sparse matrix elements are computed. MoM is used for interactions in the same box and neighboring boxes. Other interactions are assigned to the far-field. Neighboring boxes are selected also because they are too close to the source box for a valid Green's function approximation [87].

Step 4: Preconditioner is applied. For sequential operations, a simpler preconditioner such as Block Jacobi or ILU is applied. For parallel operations, a more complex preconditioner such as SPAI is applied.

Step 5: Iterative solution is applied.   The stored sparse near field matrix solution is directly computed [77].   Calculation of far field interactions for all other boxes through

aggregation (finding the interactions within a box to a central point), translation (translating interactions from one central point to the next) and disaggregation (determining interactions from a central point onto sub-boxes or members of the box) as shown in Figure 8 is performed [77], [88].
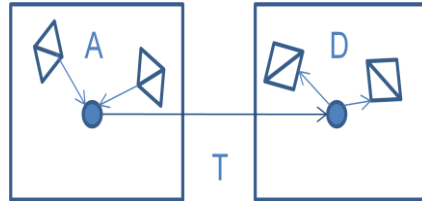
Figure 8 MLFMM processes (aggregation, translation and disaggregation).

As stated earlier, understanding the intricacies of the MLFMM application as well as the outer iteration parameters is necessary for optimizing advanced parameter settings. For instance, if parallel processors are used, the preferred preconditioner is SPAI. Consequently, altering the fill level of ILU will not promote a better solution.

2.3   Higher Order Basis Functions

Heretofore we have discussed implementations to extend the frequency/electrical size range of solutions based on MoM with RWG basis function implementations including preconditioners with MLFMM for parallelization. For accurate representation, the triangular patch RWG function with constant current assumptions require about 100 unknowns per square wavelength, and are widely used because they have straight forward field integrals and satisfy continuity [69]. However, in addition to a high memory requirement, these RWG functions also have low-order convergence requiring large increases in the number of unknowns to achieve small increases in accuracy [69].

Higher order basis functions show faster convergence and have hence been a subject of interest. For MoM, Wandzura and Hamilton extended the RWG basis functions to higher order. In addition, the use of the quadrilateral patches, instead of the triangle patches, reduces the required unknowns per wavelength to about 72, even with zero order approximations [69].

Another method used to extend MoM to electrically larger structures is to change the basis functions from subdomain to entire domain. Typically entire domain is used practically not over the entire structure, but over elements much larger than those supported by linear based functions. For instance, entire domain functions can represent currents on the order of a couple of wavelengths while subdomain functions, such as roof-top and RWG, require elements on the order of one tenth of a wavelength to properly represent the currents. Entire domain functions are normally implemented by means of higher order polynomial and trigonometric functions such that changes in current over the element are represented by this single function. Lagrangian polynomials which are a classical way of solving a set of equations with constraints are often used for the higher order function. The choice of polynomial should be based on its ability to reduce unknowns. Trigonometric functions are orthogonal, but the orthogonality property is not always useful in the evaluation of field integrals. One obstacle in the implementation of the higher order basis functions, however, is the continuity equation that is automatically met with some piecewise linear functions such as the rooftop function, is not automatically met for polynomial functions. Continuity then must be applied separately at free edges and joining segments. Adding the continuity equation to the basis functions results in a higher number of basis functions than the necessary testing functions, which prevents direct Galerkin method implementation. Careful choice of the basis functions with hierarchical properties can reduce the number of unknowns and allow the use of Galerkin method [89][90].

Use of these higher order basis functions have been shown to be comparable to CFIE implementations of coated dielectric structures [91],[92] .

To implement this method, a function is first applied to a single element to approximate the currents over that element. Next, the single element functions are combined with the continuity equation. In addition, the continuity equation allows the expression of one current in terms of the other. Taking advantage of this allows the number of unknowns to be reduced and the application of the Galerkin test function feasible.

The current intensity is approximated along the wire I(s) by a sum of finite polynomials in (64) as described in [90]:

$$I(s) = \sum_{i=0}^{n} a_i \left(\frac{s}{L}\right)^i \qquad -L \leq s \leq L \qquad (64)$$

where the wire length along coordinate s is 2L, and a_i, $i = 0$ to n, are the unknown coefficients.

For example consider two wires connected at their ends, the continuity equation at s $= L$ is

$$I_1 + I_2 = 0 \qquad (65)$$

Hence, by incorporating the starting expansion I_1 can be written:

$$I_1 = a_0 - a_1 + \sum_{i=2}^{n} a_i(-1)^i$$

Thus unknown coefficients are expressed in terms of other unknown coefficients and unknown current intensities at wire ends. Substituting this result into the unknown wire ends

gives a starting current expansion where Galerkin testing can be applied (permission granted) [90].

$$I(s) = \frac{1}{2}I_1[1 - s/L] + \frac{1}{2}I_2[1 + s/L] + \sum_{i=2}^{n\_even} a_i[(s/L)^i - 1]$$

$$+ \sum_{i=3}^{n\_odd} a_i[(s/L)^i - s/L]$$

From this expression it can be seen at the free wire ends that the basis functions are equal to zero and only the basis function corresponding to I_1 influences the continuity equation satisfaction at the interconnection.

This process can also be applied to plates in a more complex way resulting in the following equation for bilinear surfaces [90]:

$$J_{ss}(p, s) = \frac{1}{e_p(s)\sin(\alpha_{ps}(p, s))}$$

$$\times \sum_{j=0}^{n_p} \left\{ b_{1j}\frac{1 - s}{2} + b_{2j}\frac{1 + s}{2} + \sum_{i=2}^{n_{s\_even}} a_{ij}[s^i - 1] + \right.$$

$$\left. + \sum_{i=3}^{n_{s\_odd}} a_{ij}[s^i - s] \right\} p^j$$

$$-1 \le p \le 1 \quad -1 \le s \le 1 \quad e_p = \left|\frac{d\mathbf{r}(p, s)}{dp}\right|$$

For bilinear surfaces, the parametric equation $\mathbf{r}(p,s)$ is a linear function of the p-coordinate making the Lame coefficient, e_p, a function of the s-coordinate only [90]. Note that

47

the sine functions result from taking the normal direction of the adjoining surfaces and $e_p(s)$ represents the Lame function.

This basis function is defined over two interconnecting plate, sometimes referred to as a doublet, and will reduce to the quadrilateral rooftop function for subdomain approximation. These basis functions should ideally have both global and local continuity, have simple field integrals and have constant current and charge distributions. The use of higher-order basis functions has also been shown to decrease local charge variation on the solution [66].

An intuitive step is then to combine the benefits of MLFMM with higher order basis functions to further accelerate the solution with minimal unknowns, however there are limitations to this approach because the direct MoM method is only applied to near interactions in MLFMM, while multipole expansion is utilized for far interactions. As discussed in Section 2.2, the boxing process in MLFMM subdivides the initial cube into smaller boxes, with the smallest box size several times larger than the largest patch edge. Because of the size of the edge length in RWG versus higher order basis functions is much smaller, the number of levels of MLFMM is one or two less than that for RWG basis functions. Also the number of unknowns in each group is larger for higher order basis functions than for RWG causing more near field interactions to be computed and stored for the higher-order case. Thus the efficiency of higher order Galerkin method with MLFMM is low [69]. Although some of these constraints can be overcome by changing the testing functions, the direct higher order MoM (HO MoM) discussed in this section and the RWG based MLFMM approach will be the major focus of this dissertation.

2.4   Physical Optics

Physical Optics is an asymptotic numerical method used for electrically very large structures. This, along with ray tracing techniques such as geometric theory of diffraction, has been shown effective on large open structures, but evidence of applicability in cavity problems is not readily available. The current density on a PEC at observation point $\vec{r}$ is calculated as shown in [93] as

$$\vec{J}^{PO}(\vec{r}) = \begin{cases} 2\hat{n} \times \vec{H}_i(\vec{r}) & illuminated\ region \\ 0 & shadowed\ region \end{cases}$$

(66)

These equations are valid for an infinite plane interface, but have been found to be accurate when applied to each mesh unit for structures that are very large electrically [94]. Creeping waves behind metal structures are not adequately simulated, thus solution inaccuracies have been found to occur behind conductors such as in antenna back lobes and when radius of curvature is small. Improvements can be made by increasing the number of interactions considered and using a hybridized PO/MoM solution where MoM is implemented for sources with smaller features [95]. The PO results are compared to MLFMM solutions in Section 3.3.2 to examine their applicability to launch vehicle fairing field predictions.

2.5   Approximation/Statistical Prediction comparison Techniques

The primary methods of field prediction/measurement comparisons are those related to the cavity Q and statistical distributions. Both of these methods are used for comparison in this study and are summarized here.

Determining the fields due to internal fairing transmission has been largely dependent on predicting some average value based on the predicted Q in the cavity as discussed in the

introduction section [24]. This cavity Q prediction relies on determining four separate Q factors that affect the overall Q as shown in (67) below. At frequencies of interest for launch vehicles the dominant effects relate to absorption in cavity walls and loads within the cavity.

$$Q_{antenna} = \frac{16\pi^2 V}{\eta_t \eta_r \lambda^3}$$

$$Q_{walls} = \frac{3V}{2u_r S\delta}$$

$$Q_{apertures} = \frac{4\pi V}{\lambda \langle \sigma_l \rangle}$$

(67)

$$Q_{absorber} = \frac{2\pi V}{\lambda \langle \sigma_a \rangle}$$

Where V = cavity volume, S is the cavity surface area, σ_l and σ_a is the aperture and absorber cross sections, δ is the skin depth, and $\eta_t \eta_r$ are the transmitter and receiver efficiencies.

These equations have been proven useful especially by the reverberation community where absorbers are a very low percentage of the total volume of the chamber and the walls are intentionally very conductive. Nevertheless, measured chamber Q's seldom reach the calculated Q values based on textbook metal conductivities. One reason is the conductivity dependence on frequency and another is the material surface effects can alter the Q. That is, the surface roughness alters the ability of the chamber to highly focus the fields resulting in a lower Q. For instance, applying a highly conductive spray on less conductive walls can actually lower the Q of the chamber [96].

The reverberation community described in the introduction section 1.1.2 uses statistical distributions to predict the maximum expected cavity values within a certain confidence interval

based on detailed test characterization of the chamber with multiple paddle wheel positions. This technique is known as mode stirring where each paddle position changes the electromagnetic boundary conditions of the cavity. As the tuner position is adequately rotated, the sample will be independent from the previous sample. Independent samples are needed to monitor the reverberation testing for proper statistics. Position and frequency stirring are other means of changing these boundary conditions. The position or measurement location is altered with position stirring, while the frequency is swept for the frequency stirring approach in which uncorrelated samples are determined when the difference between frequencies of two points is greater than the Q bandwidth shown in (68) [97].

$$\Delta f > \frac{f}{Q(f)} \qquad (68)$$

Figure 9 depicts a sample of a chamber modal structure represented by colors with various intensities where the wider bandwidth Q captures more modes [28].
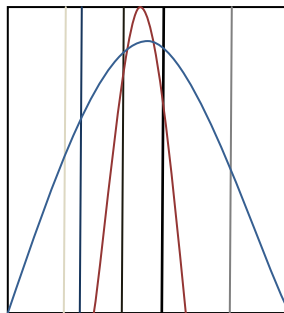
Figure 9. Q bandwidth and modes.

In reverberations chambers it is desirable for the Q to be high to generate higher fields for test purposes, but wide enough to include enough modes so that the proper statistics are

51

maintained for a predictable test. Increasing the complexity and size of the room will increase the number of modes, while lowering the conductivity of the walls will widen the bandwidth.

The expected probability distribution function (PDF) for a single field component in a mode dense cavity is the Chi or Rayleigh distribution with two degrees of freedom as depicted in (69) [28]. The two degrees of freedom represent the magnitude and phase of a single axis electric field component. For magnitude of the total field six degrees of freedom may be used, but better comparison results are obtained in practice by examining field components separately.

$$f(|E_z|) = \frac{|E_z|}{\sigma^2} exp\left(-\frac{|E_z|^2}{2\sigma^2}\right)$$

(69)

Cumulative distribution functions (CDFs) are readily applicable to test data and are typically selected over the PDF for statistical comparisons involving test. The mean normalized CDF for the Chi distribution with two degrees of freedom is shown in (70). These statistics are applied in the later sections of this study so that small E-field probes could be utilized. In reverberations chambers the Chi squared CDF representing the power is applied more often [96].

$$F(x) = 1 - exp\left(-\frac{\pi}{4}x^2\right)$$

(70)

When the cavity does not have adequate modes, as with very high Q chambers, this distribution may not apply. The Weibull distribution can more generally be applied in these cases [27],[98]. The corresponding PDF and CDF are shown below in (71).

$$f(x) = abx^{b-1}exp\left(-ax^b\right)$$
$$F(x) = 1 - exp\left(-ax^b\right)$$

(71)

Note, that when b = 1, the distribution corresponds to the exponential distribution and when b = 2, it corresponds to the Rayleigh distribution.

The applicability of these Q and statistical techniques to launch vehicle cavities, that typically contain acoustic absorbers and are often made of composite material, will be examined in this dissertation. In recent years, several other communities have undertaken similar experiments to determine the effect of internal radiators in cavities which are not ideal reverberation chambers such as airplanes [99], shipboards [97], and even launch vehicles [25]. The effectiveness of these the Q predictions is highly dependent on the accuracy of wall conductivity inputs and absorption characterization.

Tait cleverly combined source and frequency stirring in his "random walk" technique using a portable multidirection antenna transmit and receive device to negate the need for a paddle [97] . This method showed that the same statistics could be applied inside a crowded ship as in a reverberation chamber. These statistical methods can be easily accomplished on ships and other platforms that are designed to have people walking in them, however, are less practical on vertical launch vehicles where supporting antenna and/or paddle mount structures are needed [97]. Position and frequency stirring are also used for statistical comparisons on the composite test fixture described in Section 5.3.5.

2.6   Transmission Line Matrix Method or Transmission Line Modeling (TLM)

The method used to analyze the transient induced pulse from nearby lightning strikes is TLM. This numerical technique solves the field problems by using circuit equivalents and transmission line theory. TLM divides the physical space into circuits that can be solved for voltages and currents that are related to fields through analogies to Maxwell's equations [64].

For instance, if a two dimensional shunt node illustrated in Figure 6 is considered, the Helmholtz wave equation shown in (72) and derived in [64] applies.
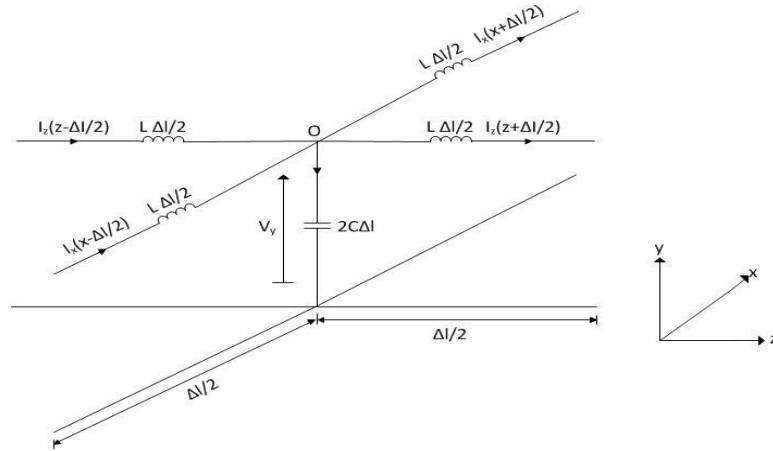
Figure 10. Equivalent network of a two-dimensional TLM shunt node [64].

$$\frac{\partial^2 V_y}{\partial x^2} + \frac{\partial^2 V_y}{\partial z^2} = 2LC\frac{\partial^2 V_y}{\partial t^2}$$

(72)

To equate to field theory, the Helmholtz equation in (73) can be derived from Maxwell's equations.

$$\frac{\partial^2 E_y}{\partial x^2} + \frac{\partial^2 E_y}{\partial z^2} = 2\mu\varepsilon\frac{\partial^2 E_y}{\partial t^2}$$

(73)

Comparing these equations yields the following equivalence between parameters

$$E_y \equiv V_y$$

$$\mu = L$$

$$\varepsilon = 2C \tag{74}$$

Therefore, the voltage at the shunt node is E_y. The inductance per unit length is the permeability of the medium and twice the capacitance per unit length is the permittivity of the medium. The magnetic fields can similarly be related to the currents in the equivalent circuit.

The TLM method is ideal for transient events in electrically small structures such as is the case with lightning where frequency content is predominantly under 30 MHz (discussed in Section 7.3.3). To adequately model the vehicle walls with this technique a thin film is model is developed where volume resistivity and thickness are handled using a skin depth approximation.

2.7 Equivalent Impedance Techniques

To reduce the computational time and memory requirements when analyzing layered material, it is desirable to use an equivalent structure, i.e. an equivalent impedance, wherever possible. FEKO, WIPL-D and CST Microstripes have such equivalent impedance implementations. Surface impedance sheets, thin films, thin dielectric sheets, and distributed loading models are implemented through a direct material property parameter entry in these tools. "Good dielectrics" and "good conductors" have straight forward formulations [20]. For other materials when required equivalent parameters are unknown or program constraints are not met, these parameters can be derived by test or analysis outside of the solver. In this research, the surface impedance models implemented needed to be developed in conjunction with externally calculated analytical and test models.

2.7.1 Surface Impedance Sheet

If the surface impedance of a thin conductive sheet is known, it can be modeled as an impedance sheet. The complex surface impedance represents an infinitely thin layer. If the surface impedance is not known, or if it is desired to represent a layered material, each layer's material properties can be modeled and the equivalent surface impedance can be calculated within FEKO. In this case, each layer is represented as a dielectric with appropriate thickness, relative permittivity and associated loss tangent or conductivity. The combination of layer properties is formulated into an equivalent single surface impedance using the volume equivalence principle and denoted as a thin dielectric sheet (TDS). This TDS can be stand alone or combined as a coating to a conducting surface. The layered approach is based on the outward normal of the structure with the outermost layer listed first [74]. Restrictions of this technique include that the thickness of the overall material, including all layers, must be electrically thin with respect to the propagating media (normally air) and geometrically thin with respect to mesh dimensions. The thickness does not have to be small with respect to the wavelength of the layered media itself. Propagation within the layered material is assumed to be in the normal direction as it would for a good conductor with perpendicular incidence where $\sigma_2 \gg \omega \varepsilon_0 \varepsilon_{r2}$, $\sigma_2 \gg \sigma_1$ [67]. When the surface impedance is implemented in the MoM surface integral equation, an additional term of $-Z_s J_s$ is added to the standard PEC EFIE in (23) as shown below, with small additional computational costs [67].

$$E_{s,tan} - Z_s J_s = -E_{i,tan}$$

$$(75)$$

The surface impedance in the above EFIE equation for a given material thickness d is defined as

$$Z_s = \frac{\beta_2}{2j\omega(\varepsilon_{2-}\varepsilon_1)\tan\left(\beta_2\frac{d}{2}\right)}$$

(76)

Assuming the layer is electrically thin such that $|\beta_2 d| \ll 1$, the TDS approximation becomes

$$Z_s = \frac{1}{j\omega(\varepsilon_{2-}\varepsilon_1)d}$$

(77)

and for metallic surfaces, the surface impedance is represented as [74].

$$Z_s = \frac{1-j}{2\sigma\delta_{\text{skin}}\tan\left[(1-j)\frac{d}{2\delta_{\text{skin}}}\right]}$$

(78)

These are the formulations used in later sections to represent the layers by specifying impedance sheets or by specifying the dielectric properties of the layered materials in a TDS. Conductive thin films are similarly implemented in CST Microstripes where volume resistivity is combined with the appropriate skin depth for materials that are penetrable by electromagnetic fields [100].

2.7.2 Distributed loading

In WIPL-D, layered materials can be modeled similarly, i.e. directly as a dielectric with a specified conductivity or as a distributed coating. When modeling thin materials, the size of the mesh needs to be less than the material thickness, which can become computationally prohibitive at GHz frequencies for electrically large structures. For very thin materials, the layer can also be modeled as an infinitely thin layer by designating one side of the geometry as air within WIPL-

D. Alternatively, thin coatings can be modeled as homogeneous resistive or dielectric distributed loadings represented by a surface impedance [66]. The constraint to apply distributed loading is $|\sigma_m + j\omega\varepsilon_m| \gg |j\omega\varepsilon|$ and $d \ll \lambda$, where σ_m and ε_m are the conductivity and permittivity of the modeled material respectively, and ε is the permittivity of the propagating media.

For conductive media the surface impedance is given as [66]

$$Z_s = R_s + jX_s = \frac{1}{\sigma_E d} \qquad (79)$$

$$\text{where } \sigma_E = \sigma_m + j\omega(\varepsilon_m - \varepsilon)$$

and for dielectrics, the surface impedance is formulated as given in (77).

Hence we see that all commercially available tools have similar parameters and thickness constraints in the use of their equivalence models.

2.7.3   Hallet Redell Method

The equivalent impedance of the layers can also be derived outside of the computational solver and entered into the model as an impedance sheet or material characteristic of a dielectric. The method, published by Hallet and Redell to determine the electric fields in a vehicle cavity with layered wall material, has been implemented in this industry and will be used for comparison data. They represented the layers as one equivalent impedance through an iterative process of determining the equivalent intrinsic impedance of two layers at a time. The impedance of the equivalent layer is given by [17].

$$\eta_L(1) = \eta_1 \left\{ \frac{\left[(\eta_2 + \eta_1)e^{\alpha_1 l} + (\eta_2 - \eta_1)e^{-\alpha_1 l}\right]\cos\beta_1 l + j\left[(\eta_2 + \eta_1)e^{\alpha_1 l} - (\eta_2 - \eta_1)e^{-\alpha_1 l}\right]\sin\beta_1 l}{\left[(\eta_2 + \eta_1)e^{\alpha_1 l} - (\eta_2 - \eta_1)e^{-\alpha_1 l}\right]\cos\beta_1 l + j\left[(\eta_2 + \eta_1)e^{\alpha_1 l} + (\eta_2 - \eta_1)e^{-\alpha_1 l}\right]\sin\beta_1 l} \right\} \qquad (80)$$

where

α is the attenuation constant of the media,

58

β is the phase shift constant of the media, and

l is the length (thickness) of the media.

For layered media lining the walls of a cavity with an internal transmitter, the most external layer has an impedance η_2 and the next most external layer, an impedance of η_1. This equivalent intrinsic impedance η_L is then treated as the most external layer and used as η_2 in the equation. This process is repeated for all the layers until a final equivalent layer is achieved at the innermost layer.

This equivalent intrinsic impedance is then used to compute the electric field in the cavity using Poynting's Theorem which states "The power delivered by internal sources (the payload transmitter) to a volume is accounted for by the power dissipated in the resistance of the media (air) plus the time rate of increase in power stored in the electric and magnetic fields in the volume plus the power leaving through the closed surfaces(s)." Steady state assumptions are made and the electric field that could dissipate the transmitted power across the vehicle inner surface area is calculated as [17].

$$|E| = \sqrt{\frac{P_t}{2\sum_{n=1}^{n=k} A_n \cdot real\left(\frac{\eta_n}{|\eta_0 + \eta_n|^2}\right)}}$$

(81)

where

η_0 is the intrinsic impedance of the media (air) in the fairing volume.

η_n is the complex impedance of the surface layer material

A_n is the surface area in square meters.

n is a designator for each surface type.

In the Hallet Redell method an average value of the fields within a cavity with the lining layers replaced with an equivalent impedance layer is computed. Assumptions made to simplify this method for feasibility of implementation are provided below.

- o The magnitude of the RF field is hypothesized to be equivalent to the magnitude of a single incident wave which would dissipate the total transmitter RF energy in the surface areas.

- o The uniform energy density within the volume is that of a wave of magnitude E_0 everywhere within the volume.

- o Steady state conditions negate the need to characterize the gain properties and distance of the source within a cavity.

- o Propagation through the medium is at normal incidence.

In this dissertation a brief comparison of the field distributions computed using this method and those computed using MLFMM is referenced in CHAPTER 4. The equivalent impedance technique for layers used here is implemented successfully for thin layers in the HO MoM method when compared with test data in Section 4.3.2.1.

2.7.4 Nicholson-Ross-Weir (NRW) Technique

The measured (test) values of unknown material electrical parameters may be determined by using either antenna measurements, cavity evaluations, or waveguide measurements [101], [102], [103]. The Nicholson-Ross-Weir (NRW) technique is a waveguide technique examined here for applicability to determine equivalent parameters when the composition of layered

materials is computationally expensive. An adaptation of this technique is used and explained in Sections 4.3.2.2 and 5.3 to determine the equivalent impedance of a three layer blanket and a composite shell fairing. This technique derives material electrical characteristics via S-parameter data measured in a transmission/reflection line technique using a Vector Network Analyzer (VNA). In this case a waveguide for the specific frequency band of interest is obtained and a blanket sample that completely fills the height and width of the guide is manufactured. Precision tolerances for the material sample dimensions are required for each size waveguide as any gaps between the sample and the guide can skew the results. Determining the phase between the coaxial connection points and the material sample is also crucial to an accurate measurement. The process may be performed by providing the distance parameter directly to the VNA or by using de-embedding features common to many VNAs, where measurements in the empty guide are performed first and stored for reference.

The advantage of this NRW method is that both complex permittivity and complex permeability can be obtained with conversion techniques derived for measured complex scattering parameters (S-parameters) inputs. The disadvantages are in the required precision of the material sample and the accuracy is low when the sample is multiples of a half-wavelength. This is because there are an infinite number of roots to the equation defining the material propagation constant, γ, in the dominant mode for the guide, TE_{01} as shown in (82). One iterative technique used to reduce this ambiguity is shown below with the full derivation is shown in [47].

$$\gamma = j \sqrt{\frac{\omega^2 \mu_r \varepsilon_r}{c^2} - \left(\frac{2\pi}{\lambda_c}\right)^2} \qquad (82)$$

Where γ is the propagation constant and $\varepsilon = \varepsilon_0 \varepsilon_r$, $\mu = \mu_0 \mu_r$ and $c = \frac{1}{\sqrt{\mu_0 \varepsilon_0}}$.

The mismatch caused by the change in impedance as the wave travels through the sample causes a reflection of the wave. The input reflection, Γ_{in}, obtained from the measured S_{11}, corresponds to the equivalent combination of all reflection and transmission coefficients through each interface of the material sample [104].

The ideal sample thickness for the standard NRW measurement is $\lambda/4$ to avoid ambiguous phase for half wavelength samples. For these homogeneous cases the choice of sample size does not affect the prediction of permittivity and permeability for the material and may be chosen for measurement convenience. It is important to note that the purpose of this NRW and similar methods is to predict the electrical properties of a single homogeneous material sample. In this dissertation the NRW technique will be adapted to give equivalent properties of layered homogeneous and inhomogeneous materials. In the proposed adaptation of this method explained in Section 4.3.2.2, used for layered blanketing and composite materials, equivalent material parameters are predicted with a sample size representative of the desired material implementation. That is, the resulting material properties of the complex samples are predicted based on an equivalent homogeneous sample of a given thickness. For the layered and composite sample cases, the equivalent material properties are a function of the sample length. Accordingly it is imperative that sample size is that of the actual configuration of interest. There is some literature support for determining the material characteristics using techniques typically used for homogenous samples as in the antenna method in reference [105].

2.8   <u>Summary</u>

In this section methodologies used in the analysis presented in this dissertation are summarized. These include the underlying method of moments full wave solution with

particular adaptations to extend its use to electrically large structures. MLFMM and HO MoM, the two primary methods utilized for this extension throughout this dissertation, were explained in detail so that the limits of these methods described in the following chapters could be understood. The circuit based techniques with corresponding field quantities used in TLM were provided and are applied for transient lightning sources examined in CHAPTER 7. Approximation and equivalent impedance techniques developed internal and external to available CEM tools were also described for application throughout this dissertation. The following chapters use the methodologies described here to examine and understand the payload fairing RF environment due to internal and external excitation. Both metallic and composite structures are considered with applicable fairing linings and spacecraft loads.

The first study to be considered is the presence of an internal emitter in a metallic fairing. The following chapters will consider fairing structures with increasing complexity. Layered acoustic blankets, composite structures and the effects of a spacecraft volume are also examined. Finally, shielding effectiveness is examined related to external RF transmitters and lightning induced transients in the last chapters. The focus of this research is on determining effective 3D EM modeling techniques to evaluate the spacecraft RF environment internal to the payload fairing for both internal and external sources with varied load and absorption conditions. Practical considerations when performing such test-based modeling are also highlighted.

CHAPTER 3. METALLIC FAIRING - INTERNAL SOURCE

3.1   <u>Introduction</u>

This first chapter focuses on the metallic fairing to establish limitations to the 3D techniques and describe particular issues with electrically large highly reflective cavities.

Characterizing the radio frequency environment within the fairing cavity due to active internal transmitters is a common problem in the launch vehicle industry [2].   It is desirable to limit the number of switches required to turn-on a transmitter on-orbit to achieve a reliable system, but spacecraft power buses that automatically turn-on transmitters will often lead to transmission in the fairing during system check-out procedures. Transmitting inside the vehicle fairing, however, can lead to an RF environment for which the spacecraft has not qualified. Precisely determining this environment is essential as over-qualifying sensitive spacecraft instruments can lead to damage.   Additionally, the use of computational electromagnetic software in RF environment evaluation is not yet a standard practice in the field of electromagnetic compatibility for space systems. It is thus necessary to show how accurately such tools can emulate the fairing cavity environment and what limitations specific to cavities need to be considered when developing such models.

To address the fairing environment uncertainties, launch vehicle providers have performed testing within the various launch vehicles. Transmission can occur at any spacecraft or vehicle frequency emitter with the most common sources being at the S band for telemetry data.   As vehicle testing is expensive, it is typically desired to cover testing over a wide frequency range so that data will be applicable for a variety of emitters. Double ridge guide horns are primarily used for such testing because of their large frequency range and availability

to support standard electromagnetic test requirements [106]. In this investigation, data obtained for a physical fairing fixture, using these horns for transmit and receive is compared with two different MoM based modeling methods. One method is the MLFMM described in Section 2.2 with antenna pattern implementation of the horns, and the other is entire domain or MoM with higher order basis functions described in Section 2.3 using a mutual coupling approach. Details of these models using two commercially available 3D CEM codes for electrically large systems are described herein.

3.2   Fairing Fixture - Test Results

3.2.1   Metallic Fairing Fixture

A test fairing fixture was developed to compare test results with other in-cavity testing performed by the launch vehicle industry and to provide a validation process for the computational models. The fairing fixture is made of 0.06 inch thick Lexan, a material similar to Plexiglas, with an external metal support frame [107]. Aluminum foil is used to line the test fixture in order to represent a typical metal launch vehicle fairing. The fixture was divided into several longitudinal sections to facilitate fabrication of a fairing-like model. There is a nose section, a cylindrical mid-section and a tapered lower section. Each section ends in an outer lip so that it can be bolted to the other sections. A metal frame is used at the outside structure for support [107]. The height and width of the fairing are 2 meters and 0.6 meters, respectively. These dimensions are smaller than typical fairings, but provide a reasonable representation with laboratory setting constraints. The aluminum lined fairing fixture, shown in Figure 11, is the baseline structure model used for simulations and testing.

Figure 11. Aluminum fairing fixture.

3.2.2   Test Procedure

Double ridge guide horns, EMCO 3115, were used for both transmit and receive placed at the bottom and top of the fairing fixture, respectively, with an excitation power of 1 mW as seen in Figure 12 [108]. A signal generator was used to feed the transmit antenna at the bottom of the fairing and a spectrum analyzer recorded the power from the receive antenna at the top of the fairing.

Figure 12. Horn placement in test fixture [1].

Baseline tests were performed with the aluminum lined fairing configuration. The test frequency range considered in this dissertation is 1 GHz to 6 GHz to cover the commonly used S and C transmit bands. An amplifier was added to the set-up to evaluate the adequacy of using one input power level in the test. Input power levels were set at -20, 0 and 16 dBm with the frequency response shown in Figure 13. Although there is variation across the frequency range, the data shows that these measurements are linearly scalable with power level. Accordingly, the 0 dBm transmit power level was selected for convenience for the remainder of the tests.
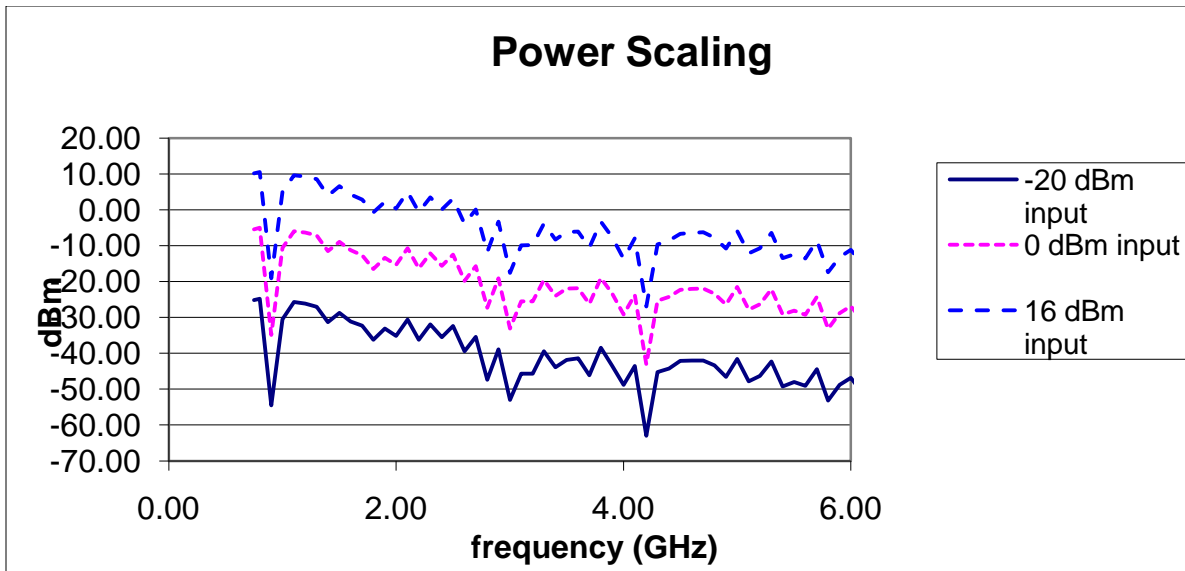
Figure 13. Frequency response with varied input power.

3.3 Metallic Fairing Fixture - Modeling and Simulation

3.3.1 MLFMM/Antenna Pattern

A Pro-Engineer (Pro-E) 3D product design computer aided design (CAD) Software model of the fairing structure was imported into the electromagnetic simulation software, EM Software & System's FEKO. For this effort, the fairing walls were modeled as perfect electric conductors (PEC) with continuous walls alleviating the need to model any external structures.

The method of implementing the antenna within the cavity has multiple considerations. The complexity of the horn antenna does not lend itself to be accurately modeled as a point-source. Hence, a full antenna model was generated using MoM and MLFMM to emulate the actual EMCO 3115 test horn as shown in Figure 14. The patterns generated across the frequency range of interest were then compared to manufacturer data and showed negligible differences in generated pattern [2], [108].

68
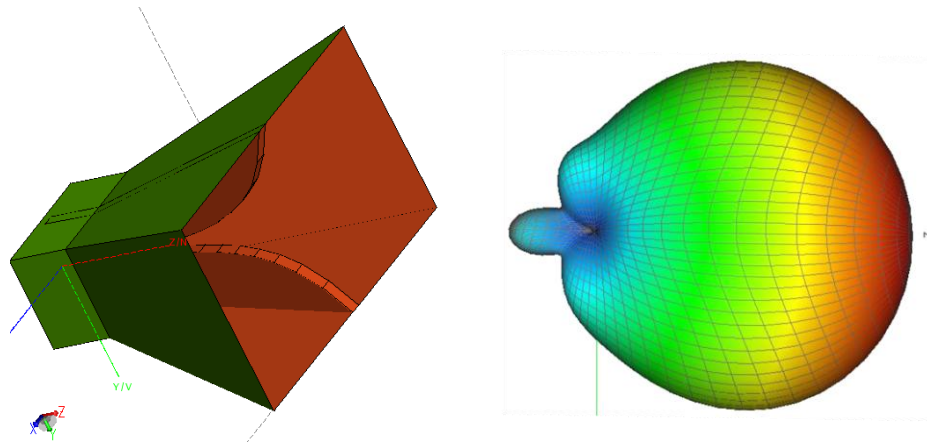
Figure 14. EMCO 3115 Double Ridge Guide Horn and model with generated pattern.

The peak gain was within 1 dB of the published EMCO gain data in the modeled frequency range and is within the peak gain tolerance of two different EMCO 3115 antenna measurements by ETS Lindgren. Note the manufacturer gain data could not be directly used in the CEM tool because it lacked the necessary phase information. Implementation of this horn into the fairing fixture can be performed in three ways within FEKO:

a. Import the antenna CAD file generated and place the antenna at the appropriate transmit and receive locations.

b. Perform separate run to generate antenna patterns as shown in Figure 14 for each frequency of interest and import the far field pattern data at the appropriate transmit and receive locations.

c. Perform separate near field pattern points in a symmetrical shape such as a sphere surrounding the antenna as shown in Figure 15 and import these points into the fairing as independent sources. This technique can only be utilized for the transmit antenna. This method has shown to be effective in [95] horn simulations on large antenna dish using

69

physical optics where the antenna is made of multiple near field sources around the sphere.
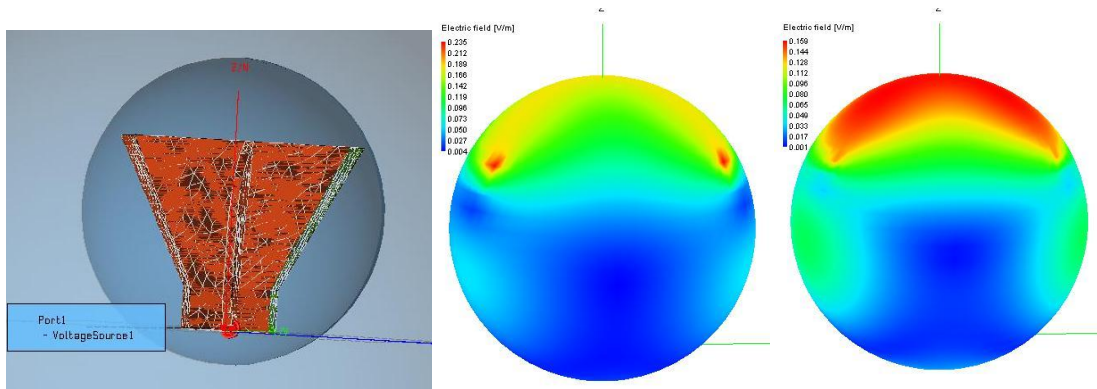
Figure 15. Near field sphere around horn with 1 GHz field simulations at 0 and 160 degree phase.

The antenna options were primarily evaluated at 1 GHz where MoM simulations were feasible. The full antenna implementation method is the most accurate, but computationally expensive for a detailed antenna structure. The near field technique did not provide acceptable results inside the cavity structure. One factor was the sphere required to surround the antenna had its boundary close to the fairing walls. The far-field pattern option was selected because it demonstrated reasonable results and is computationally efficient.

3.3.2   Computational Method Comparison

The fairing simulations were first modeled using the MoM solver to determine the frequency limit of this solution which was determined to be 1.4 GHz with 16 parallel processors and 120 gigabytes of memory for each processor. To extend this frequency limit into the S-band range two approaches were considered.

70

First MLFMM was examined to extend the frequency range of the simulation by a boxing algorithm that alleviates the full matrix solution burden of MoM. This technique maintains the use of direct MoM in the near-field regions described in Section 2.2. The EFIE equation is the standard implementation as it is applicable for open and closed structures as discussed in Section 2.1. A comparison of the E-field with EFIE MoM and EFIE based MLFMM solutions is shown in Figure 16.
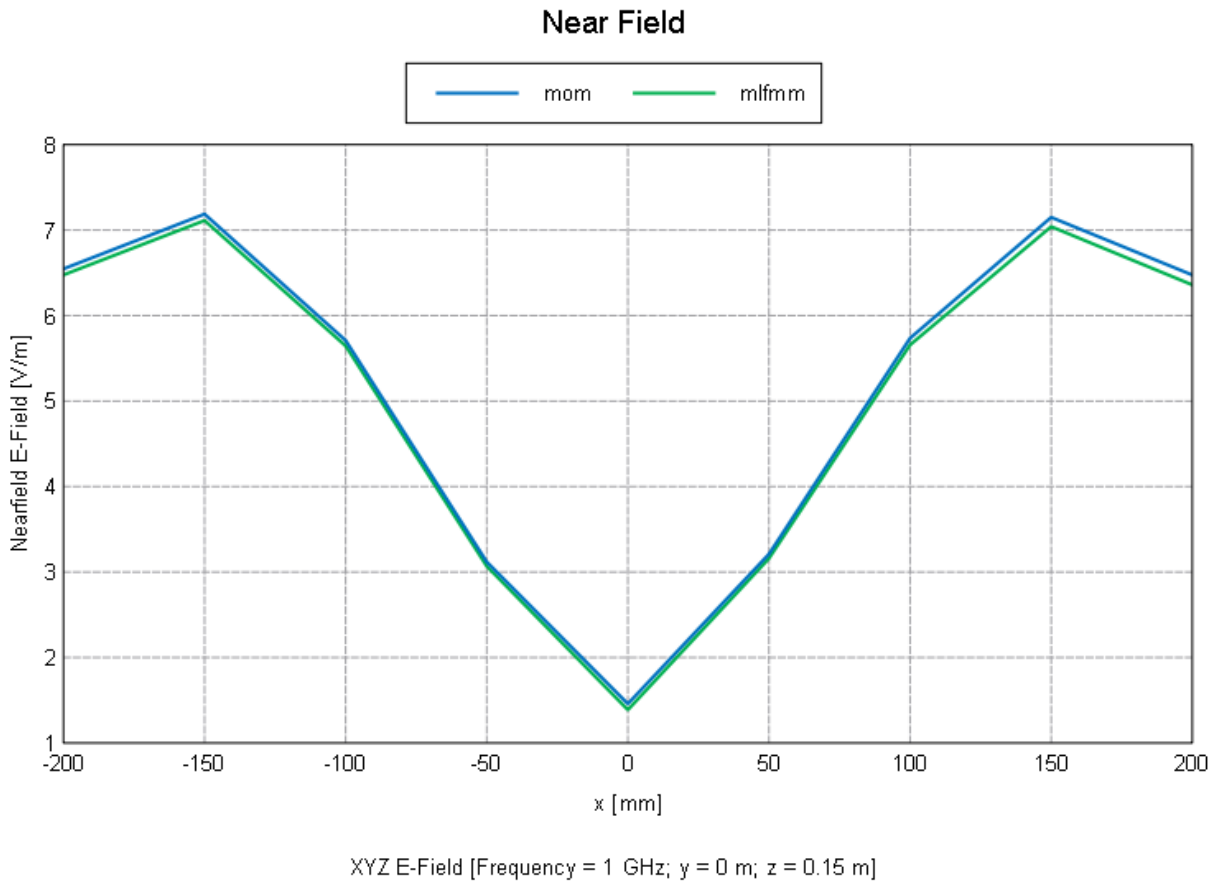
Figure 16. MLFMM/MoM EFIE E-Field comparison along horizontal axis in fairing.

The MLFMM series truncation in this case introduces only a slight approximation error. The CFIE formulation, which is only applicable for closed structures, combines electric and

magnetic integral equations to obtain a solution with better convergence properties in resonant structures.

Second, the physical optics solver was examined as a possible method to extend the frequency range of the simulation. This technique has been shown very effective in electrically large open structure simulations with FEKO and other tools [95]. As described in Section 2.4 this method is not a full wave solution like MoM, but an approximation of the currents based on the incident field. The applicability of this technique in cavity structures is of interest because of its ease of implementation and computational efficiency. Similar optics based techniques have also been used in launch vehicle evaluations making the comparison necessary. The physical optics solution was compared to the MLFMM EFIE and the CFIE solutions as seen in Figure 16.
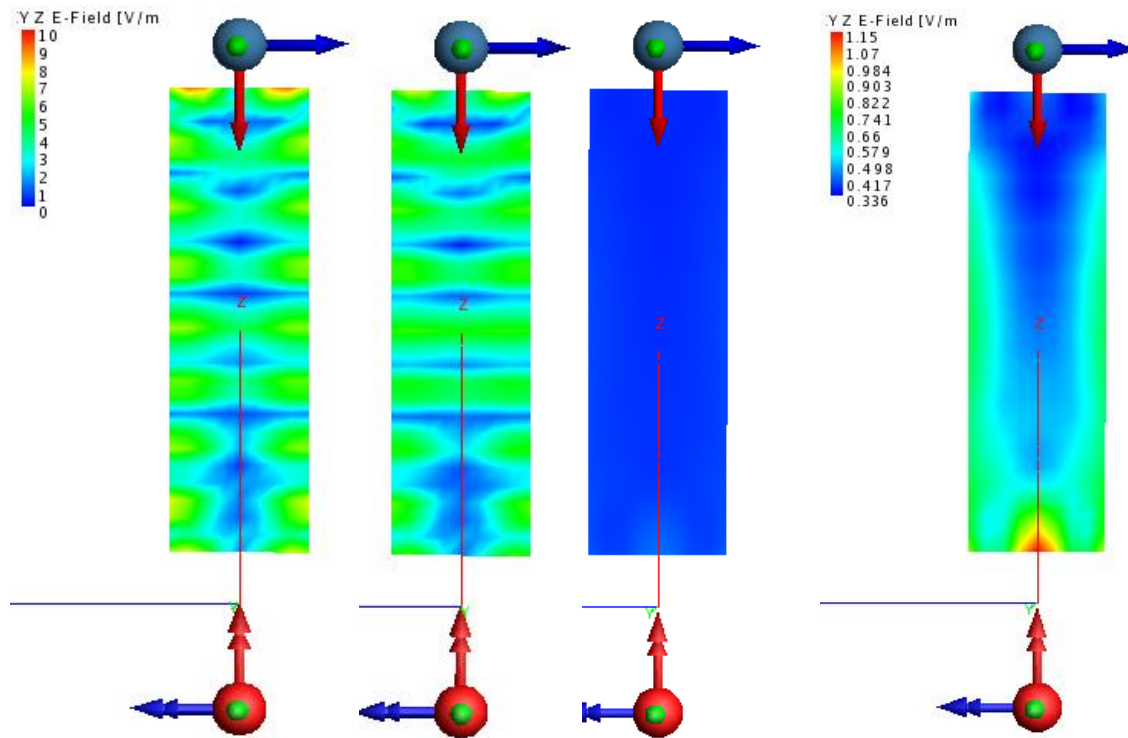
Figure 17. MLFMM EFIE, MLFMM CFIE and PO comparison at 1 GHz for fairing fixture and with PO distribution on a separate scale.

The MLFMM EFIE and CFIE have similar field distributions although the EFIE solution has a slightly higher value due to slight residual error with the EFIE solution. The PO solution has lower field intensities that are not clearly present on the same 10 V/m scale as the CFIE and EFIE solutions. The PO distribution on a lower scale is also shown in shown in Figure 16. This distribution does show higher values near wall of the cavity related to the wall currents, but does not allow for eigenmode development in the cavity with resulting fields significantly lower than the full wave solutions. The CFIE solution is more effective at reducing residual error since it combines the EFIE and MFIE equations. The MFIE, however, can only be incorporated on

73

closed structures. The implementation in the computational tool used here is limited to PEC boundaries. The linear comparison of the three techniques is in Figure 18.
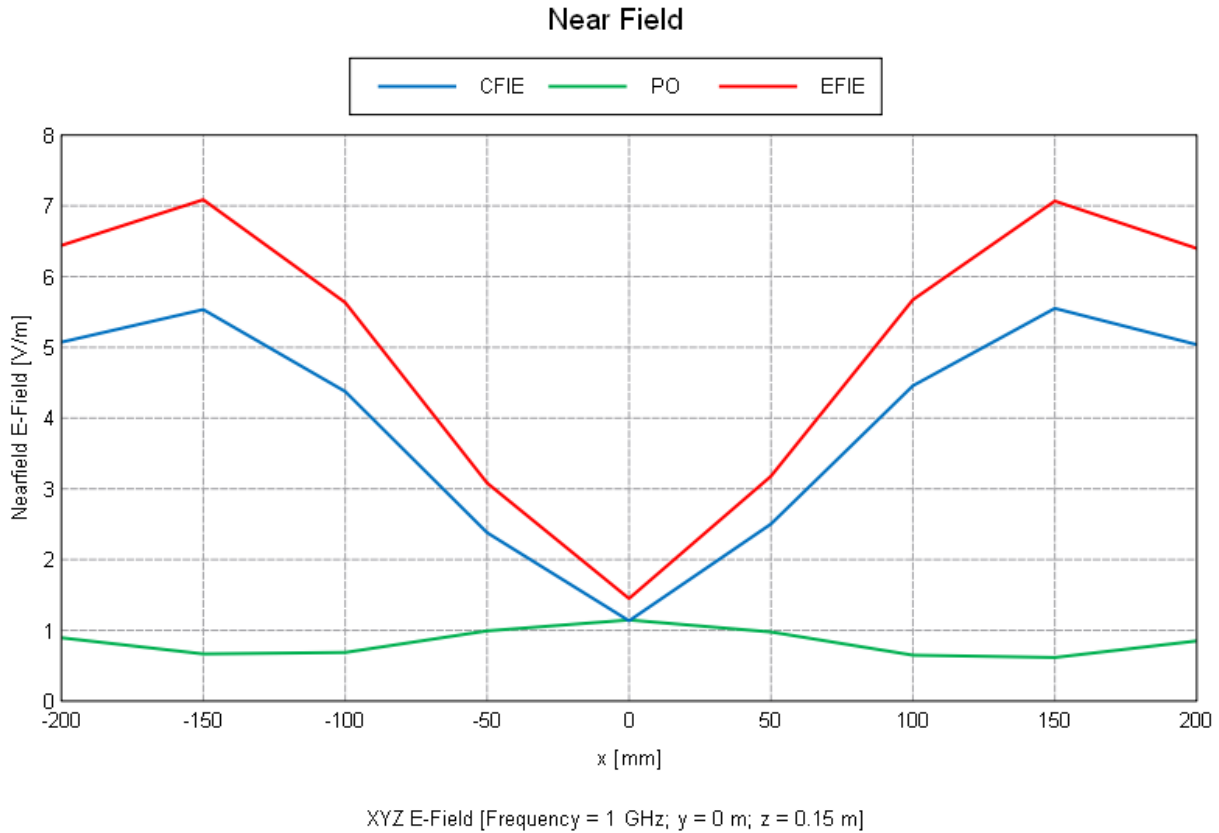
Figure 18. CFIE, EFIE and PO comparison at 1GHz in PEC fairing fixture of peak field levels along horizontal axis.

It is clear that the PO solution shown does not have adequate accuracy for this fairing structure and is not used further in this dissertation. Also in this figure, note that the EFIE magnitude is higher than that of the CFIE solution. Thus the default EFIE solution provides a bound for the field levels in the cavity. These higher fields are contributed to by a greater residual error when truncating the MLFMM solution using EFIE equations. The degree to which

74

this over-prediction of fields occurs in resonant structures using the MLFMM technique is of concern when convergence of the solution cannot be achieved. This effect is studied and discussed in this dissertation as it becomes the limiting case for utilizing MLFMM in resonant structures.

3.3.3 MLFMM Simulations

The fairing fixture was simulated from 1 to 2 GHz in 100 MHz increments using the Multilevel Fast Multipole Method (MLFMM), with new mesh generation for each frequency. Convergence issues in the MLFMM model were discovered and prompted another change in the model from the EFIE formulation to the CFIE formulation. The CFIE solution can be implemented for this PEC closed structure.

Comparison data in Figure 19 indicates reasonable correlation in the received power between test and simulation results for this electrically large cavity. The average difference in the 1 to 2 GHz band is 0.842 dB with a peak difference of 5.38 dB. Some variation would be expected due to gain differences in the test case for the transmit and receive EMCO antennas, the aluminum foil lining in the test case versus the PEC in the simulation case, and possible leakage from the test cavity where the structure is pieced together.
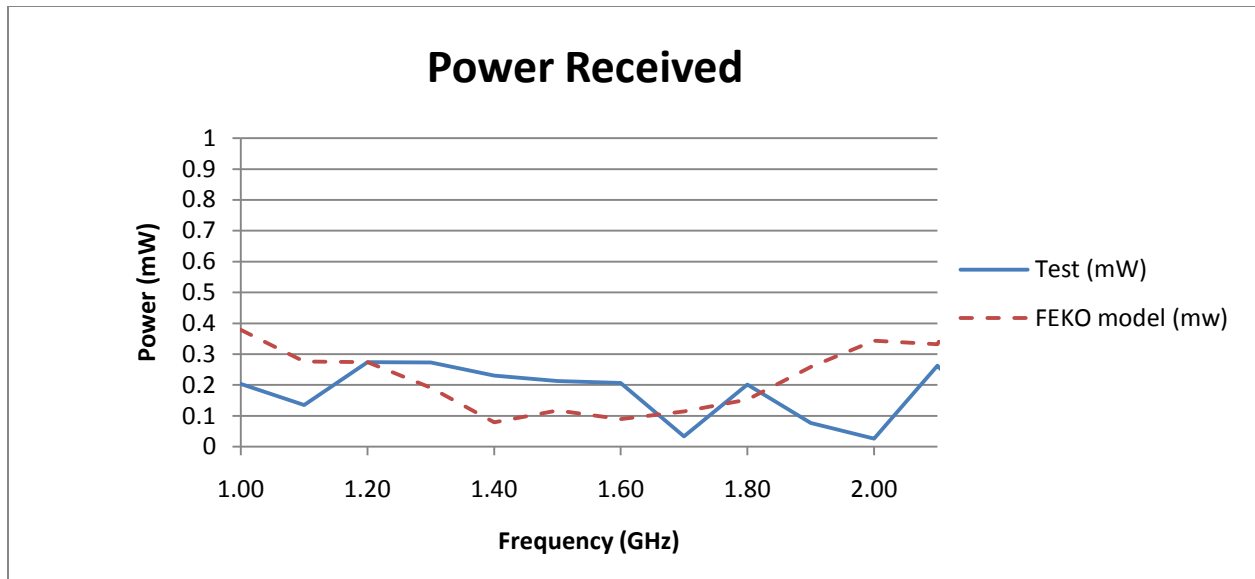
Figure 19 Simulation and test data of the aluminum lined fairing.

Both simulation and test cases showed frequency dependent variation in the power data which is expected with multiple reflections at metal walls. The standard EFIE equation simulations are shown up to 2 GHz. Beyond this frequency, convergence was not achieved. The CFIE technique achieved nearly identical results to the EFIE solution at 2 GHz and gave reasonable results at 2.1 GHz, but convergence issues persisted beyond this frequency. The probable reason for the convergence issues, even with CFIE implementation, is due to the MLFMM introducing numerical excitation that increased with increasing frequencies. MLFMM convergence issues are encountered due to truncation of the scalar Green's function implemented with the addition theory series which introduces an error that can be controlled in open structures, but difficult to achieve sufficiently accurate results in electrically large reflective cavities [69].

3.3.4   Higher Order Basis Function/Mutual Coupling Simulation

The second approach examined to increase the frequency range was to use direct MoM implementation with higher order basis functions as implemented in WIPL-D [11].   It is desirable to anchor at least two computational methods so that they can be used for comparison when test models are not feasible. Although multiple electromagnetic modeling tools exist, full wave simulation tools that can accurately model very electrically large structures are not prevalent [109]. The MLFMM technique was used in the previous section to extend the size and frequency capabilities of the MoM. The technique used in this section is also based on MoM, but uses higher order basis functions to improve computational efficiency [62].   Hence, electrically large structures can be modeled on PC platforms that have adequate memory allocations for the required number of unknowns. 80,000 unknowns were the limit for this study. This technique requires the mesh element size be on the order of a wavelength instead of one tenth of a wavelength required for linear basis function algorithms as described in Section 2.3 [66]. Evaluations within the cavity add to the computational complexity as the standard EFIE solution can accentuate errors at resonance.   As mentioned, using combined electric and magnetic field equations adds to the complexity of the solution, but greatly improves the solution accuracy. The higher order (HO) MoM solution in WIPL-D has been shown to compare well with CFIE solutions and is further examined, in this study, for test data comparisons [110].

The WIPL-D ProCAD imported fairing model is provided in Figure 20 [111]. Modifications to the meshing algorithm were applied to optimize the structure mesh to the frequency range of interest. Outer fairing walls were represented using a distributed impedance model of the aluminum surface in the S-band frequency range.   WIPL-D supports surface representation as either lumped elements or distributed impedances with minimal impact to

electric field integral equation (EFIE) solution time [66][90]. Although perfect electric conductor (PEC) and aluminum solutions are similar, the distributed impedance of aluminum was applied to account for wall losses and reduce resonant mode issues associated with EFIE solutions for closed PEC structures [7]. The integral accuracy was also increased due to the complexity of the cavity simulations [6].

One major difference in this simulation approach and that presented in the previous section is the use of the antenna geometry in the model [111]. In this simulation, the antenna is part of the computational fairing mesh model instead of being inserted only as an antenna pattern in the model. Although more computationally expensive, manifestations of eigenmode development based on the horn structure (Figure 21) are evident with this technique which cannot be captured with the pattern approach.
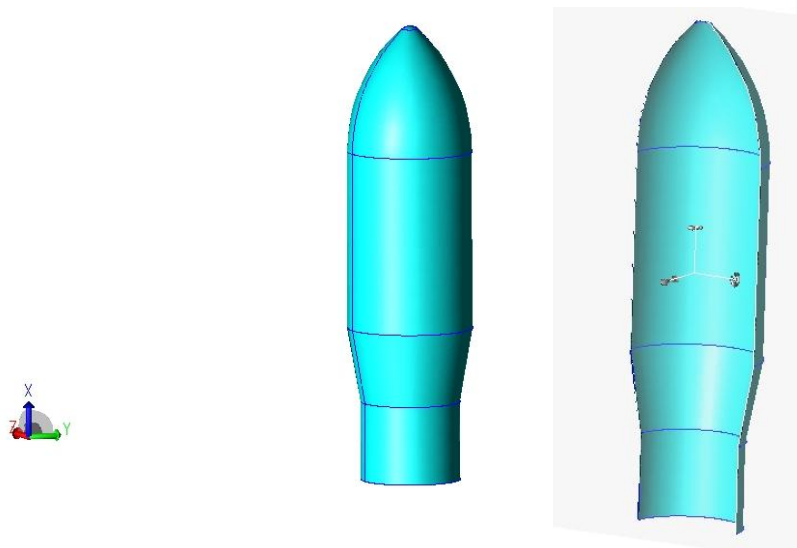
Figure 20. ProCad WIPL-D model of fairing structure.
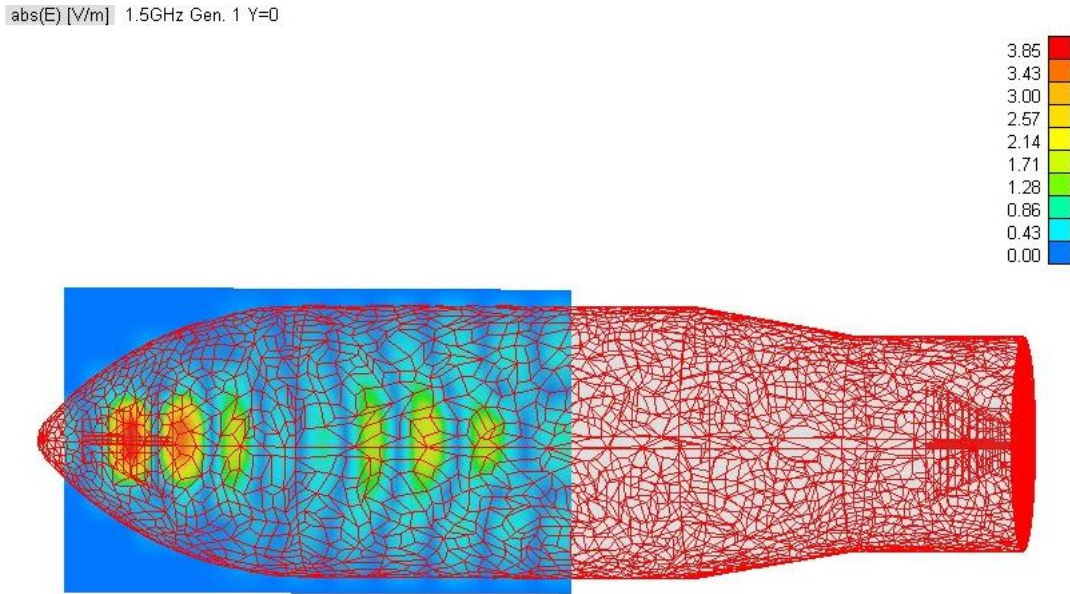
Figure 21. Resonant interaction with cavity in antenna (1.5 GHz).

Mesh refinement and small features removal were applied within the WIPL-D ProCAD environment to the EMCO 3115 model previously created for MLFMM simulations. A wire generator was added for horn excitation and favorable gain pattern comparisons were achieved [4]. This WIPL-D horn model was then imported into the fairing model and translated to the test transmit/receive locations.

The S-parameter data (S_{21}) was examined to determine the mutual coupling between transmit and receive antennas in the faring cavity by running the simulation in the "one generator at a time" mode [90]. The mutual coupling feature of this tool has previously been utilized in evaluating side by side antennas on a substrate as in the case of an antenna array [112]. In this study, mutual coupling is applied to evaluate the power reception by the horn antennas within a large fairing cavity.

The simulation data indicated reasonable comparisons with the fairing test fixture results as shown in Figure 22. The test case did not show a peak at 1.2 GHz, but the squared nature of the test data in that range indicates that increasing the granularity of test frequency would likely have revealed a peak near this frequency. In addition, there is a frequency shift at the lower frequencies between test and model data which could be attributed to the slight variation between the CAD model and the physical implementation of the structure in the upper cone (i.e. the CAD model is continuous, but the fairing fixture is implemented with rings of aluminum lined Lexan material that taper to make up the nose cone section) [107].

Overall the HO MoM method allowed further evaluation of metallic structure than the MLFMM approach did, and including the horn model offered a more accurate depiction of the coupled power. VSWR effects were not included as the model assumes a consistent power at the input of the antenna. Changes in the antenna pattern due to the surrounding cavity are captured with this method resulting in closer simulation of the peak frequencies than in the pattern only implementation. Limitations in the maximum frequency were largely due to the complexity of the antenna and fairing CAD models.
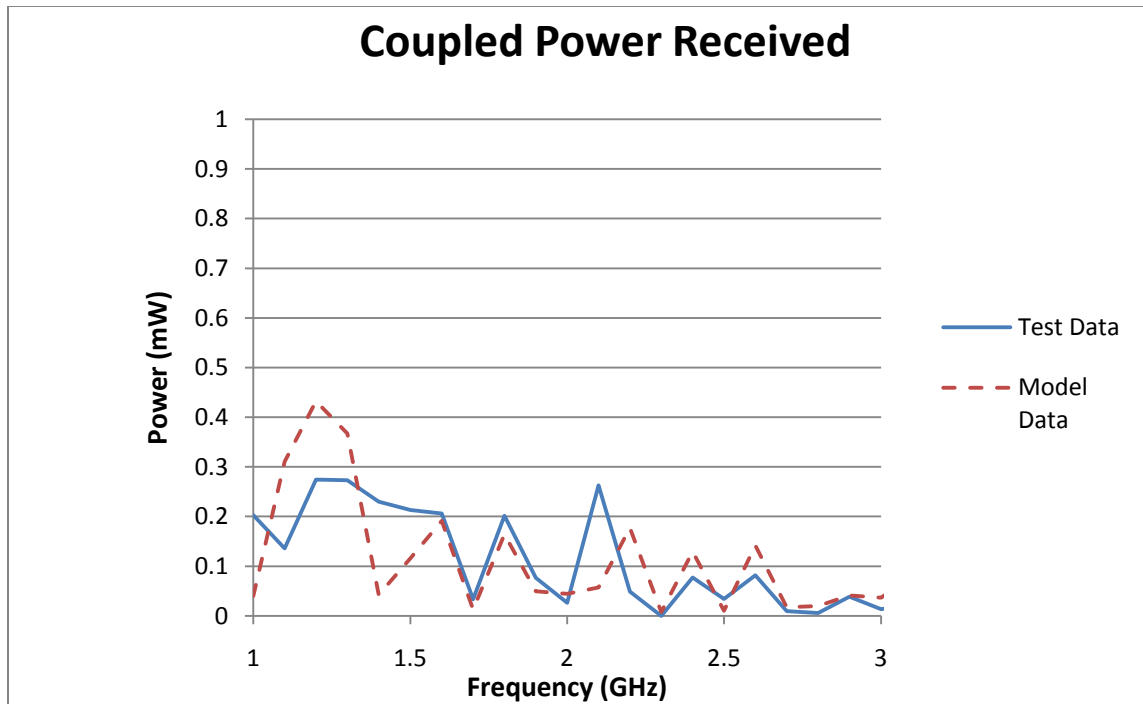
Figure 22. Coupled power results from test and the HO MoM model.

As frequency limits apply to this method when using CAD based meshes and complex antennas, the rotational symmetry of basic fairing structures can be utilized to extend the frequency range using the boundary of revolution option. For rotationally symmetric structures only the specified portion of the structure is considered in the solution resulting in huge computational savings. An example of such a model represented by 15 degrees of the entire structure is shown in Figure 23. This technique is only briefly introduced here, but is applied later in this dissertation to extend frequency and vehicle size limitations. For example a model with a similar size as the test fixture can be evaluated beyond 10 GHz depending on the model complexity.
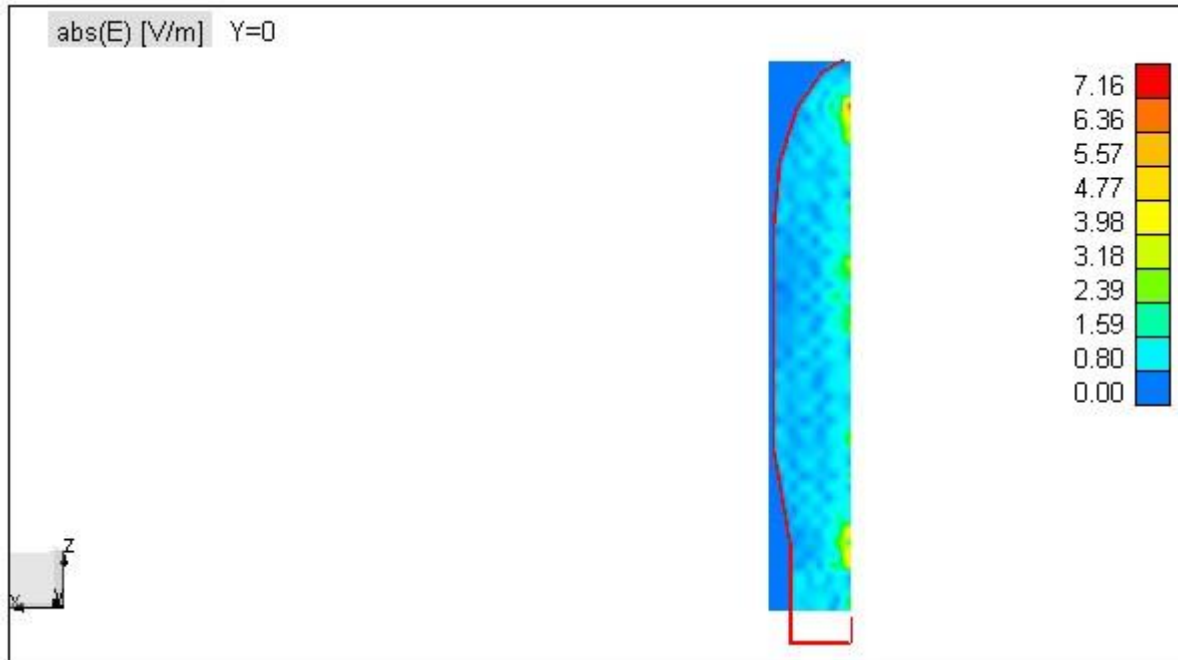
Figure 23. Rotational symmetry fairing used to extend useable frequency range by decreasing the number of unknowns.

3.4   Summary

Two methods MFLMM and HO MoM were utilized to examine modeling techniques for the S-band received power due to an internal source in a metallic payload fairing. Both showed reasonable simulation of peaks over a given frequency range. Including the antenna in the fairing model in WIPL-D, HO MoM showed better peak alignment with the test frequencies than with using the antenna pattern only in the MLFMM model. However, identification of peak values over some frequency range in the most efficient manner is the goal of this study rather than to define the exact peak at the correlated frequency because the actual spacecraft with fairing enclosure is far too complex to be exactly simulated. The antenna pattern model is more efficient, but implementation of MLFMM in a cavity with highly reflective walls creates convergence issues due to an effective numerical excitation of the cavity related to differences in

the numerical representation of zero on a perfect electric conductor [66]. For instance, the tangential electric field on a perfect electric conductor is zero, but truncation of the Green's function shown in equation (45) modifies the actual representation of this boundary to a non-zero small number. When the numerical residual errors approach the same order of magnitude as the desired solution, convergence cannot be achieved.

CFIE implementation improves convergence compared to the EFIE equation, but has minimal effect on the truncation errors introduced by MLFMM. Improvements can be made by decreasing the mesh and box size of MLFMM. This is explored more in the external emitter shielding in CHAPTER 6 as dynamic range with tight error control is especially important for these shielding models. The CFIE implementation is ideal for external sources illuminating a closed conductive cavity with PEC structures because MFIE is included in the CFIE formulation which requires a closed volume. An artificial implementation of an enclosed dielectric volume to force a different combined equation approach described in section 2.1 is also suggested in literature [71][89] and will be examined in this dissertation.

It is also evident from this research that computational efficiency would be enhanced by changes to the excitation simulation when model to test validation is desired. The double ridge guide horn antennas provide excellent gain over a wide frequency band, but require detailed computationally expensive models for accurate simulation which can consume too many resources when electrically large structures are evaluated. Thus antenna sources that can be simulated with little computational expense such as dipoles can extend the simulation frequency range while maintaining the required model accuracy. Smaller antennas will also have less effect than the larger horn antennas on the electric field distribution in the cavity volume. In addition, capacitance to nearby structure affects the gain pattern such that equations used during

testing based on manufacturer gain information are flawed when a surrounding cavity wall is in close proximity to the large horn antenna. These horn antennas are also not in the far field at some frequencies affecting results of expected antenna patterns in the model [113]. Accordingly, the use of movable field probes and smaller transmit antennas is explored for the composite structure in CHAPTER 5.

In addition, for higher order basis functions, much computational advantage can be obtained by building the model within the CEM tool as opposed to implementing the CAD model. This benefit is not realized with linear basis function as the mesh elements must be small with respect to the wavelength. Since most launch vehicles are cylindrical with conical top sections, the full benefit of entire domain basis functions can be utilized.

It should also be noted that the CEM tools used in this study are being constantly improved and frequency limitations for a given configuration will change. However, the basic limitations and mitigations for these approaches are still applicable.

CHAPTER 4. FAIRING WITH ACOUSTIC ABSORBING LAYERS – INTERNAL SOURCE

4.1   <u>Introduction</u>

All launch vehicles need some means of controlling acoustic levels in the fairing cavity due to the launch environment. The acoustic attenuation is typically implemented with acoustic blanketing which is at least somewhat RF dissipative to reduce static charging.   Blanket thicknesses can be several inches of different materials making it computationally prohibitive to model exactly.   In this chapter the acoustic blanket layers are first directly modeled for the two and three layer cases by building the CAD model with separate layers.   Then combined equivalent layers are considered to improve the computational efficiency of the models and allow for implementation on larger vehicle fairings.

As with the metal case, a physical representation is constructed to anchor the CEM tools ability to predict the fairing RF environment. First a simple case is considered where a single layer of Kapton® is placed just inside the aluminum. In this case a simple spacecraft load is also considered. Next an additional Kapton® layer is added separated from the first layer by foam. Techniques for representing these layers directly are first explored and limitations identified to emphasize the need for additional modeling techniques. Next, externally generated equivalent material property or impedance techniques for combined layers are presented. Results from these external formulations are provided as inputs to various material implementation options within the CEM tools. Two methods are examined, both of which determine equivalent material parameters based on reflection and transmission coefficients in layered materials. The first technique defines an equivalent impedance based on perpendicular incidence as described in Section 2.7.3. The second is developed using material properties predicted with S-parameters

measurement and implemented into the FEKO standard coating option (see Section 2.7.4). Parts of this research that were conducted for this dissertation are published in [23].

The focus of this section is in the S-band with some examination of the Kapton® only layer case in the C-band frequencies. The S-band is the most commonly used transmit band for vehicles and spacecraft telemetry. C-Band is also used on each mission for vehicle tracking, but is less often a problem for internal transmission as it is a vehicle band and thus more controllable. Accordingly, measurements for the equivalent technique are focused in these bands.

4.2   Layered Fairing Fixture – Test Results

The outer fairing fixture is the same as the aluminum lined structure described in CHAPTER 3. Lining materials were added to the inside of this test fixture to simulate typical vehicle fairing acoustic blankets. Kapton® is commonly used in space applications for its favorable thermal insulating properties. DuPont's Kapton® 160XC, designed to maintain a surface resistance of 377 ohms with inherent RF absorption properties, is utilized for these outer blanket layers while standard ½ inch foam is used to separate the Kapton® layers.   This material is selected as it is neither a good dielectric or a good conductor and is typical of some materials in launch vehicle fairings. Accordingly, this material provides more modeling challenges than a pure dielectric or conductive material. Figure 24 shows the lining layers.

The following test layers were considered (ii) Aluminum-Kapton (iii) Aluminum-Kapton-with spacecraft load, and (iv) Aluminum-Kapton-Foam-Kapton.

Figure 24 Lining materials (Kapton®,foam, Kapton®, aluminum foil) .

The layers were added individually and the test procedure described in Section 3.2.2 was followed.

A simple cuboidal aluminum lined structure, 26 inches high by 13 inches in width, suspended by clear nylon line to evaluate the effects of adding a spacecraft load to the vehicle was added to the model. The test procedure was repeated for the load case.

The data taken from 1 to 6 GHz for the three different lining configurations is shown in Figure 25.   The test data obtained for the aluminum lined fairing shows wide variation in power levels. This case has predominately the highest envelope.   Peak levels in the aluminum only lined case in the 3 to 6 GHz range are 5 to 10 dB above the power data from the Kapton® lined cases.   Each additional layer caused less received power level fluctuation.   A profound smoothing effect was observed with use of multiple separated layers of Kapton®. Similar cavity variation was shown in the NASA Hallet Redell work presented in [17]. In spacecraft loaded case fluctuations are further attenuated at some frequencies. These results below are used for comparison to the simulated results.
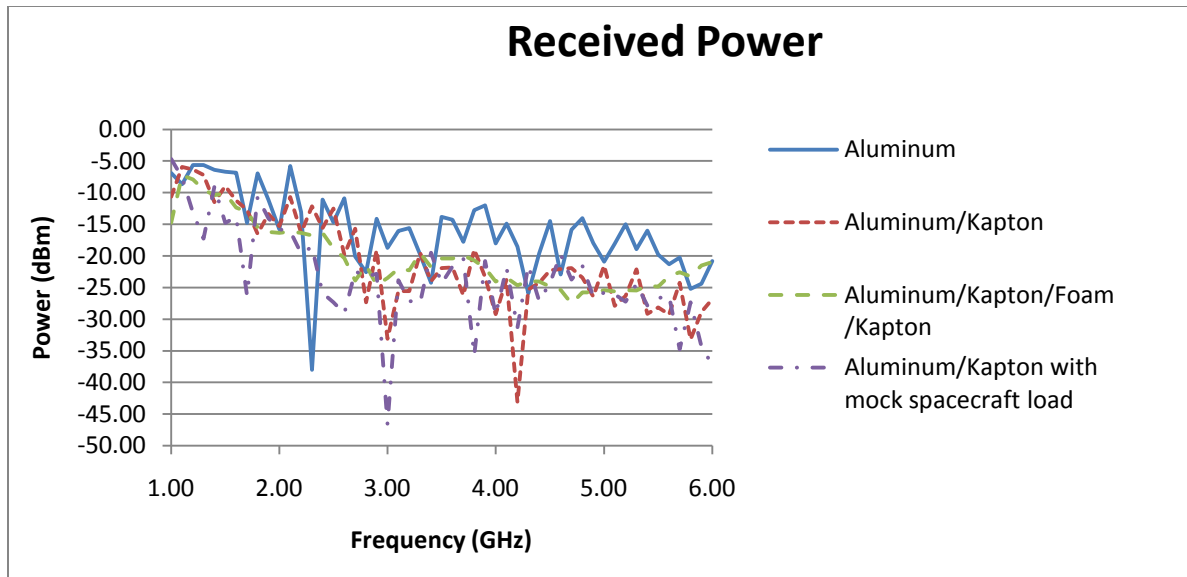
Figure 25. Power measurements for fairing with bare aluminum and with blanketing materials.

4.3   Layered Fairing Fixture - Modeling and Simulation

4.3.1   Separate Layer Models

4.3.1.1 Two Layer Model – Aluminum and Kapton® Layer

The first model considered is the direct model of the two layer CAD input, with an outer aluminum layer and an inner Kapton® layer in the S and C frequency bands. Individual layers to represent the metal shell and the lining can be represented in FEKO at a significant memory and CAD model development expense and is discussed here. Using layer representations that characterize the material absorption can improve MLFMM convergence.   The absorbing impedance sheet option, based on the addition of a surface impedance term to the PEC EFIE solution as described in section 2.7.1, requires a layer of free space on either side of the impedance sheet. The CFIE formulation in FEKO requires a PEC structure and is not an option when representing losses in a cavity is desired [61].

88

To meet the free space requirements a separate CAD model was constructed with an internal layer just inside the aluminum layer. The model differs slightly from the actual Kapton[®] layer in the physical fixture which was directly against the fairing walls with intermittent air pockets, while the model has a consistent layer of air between the aluminum and the Kapton[®] to meet impedance sheet requirements. Figure 26 and Figure 27 show a comparison between the test data and the two layer model for power received in the S and C bands.
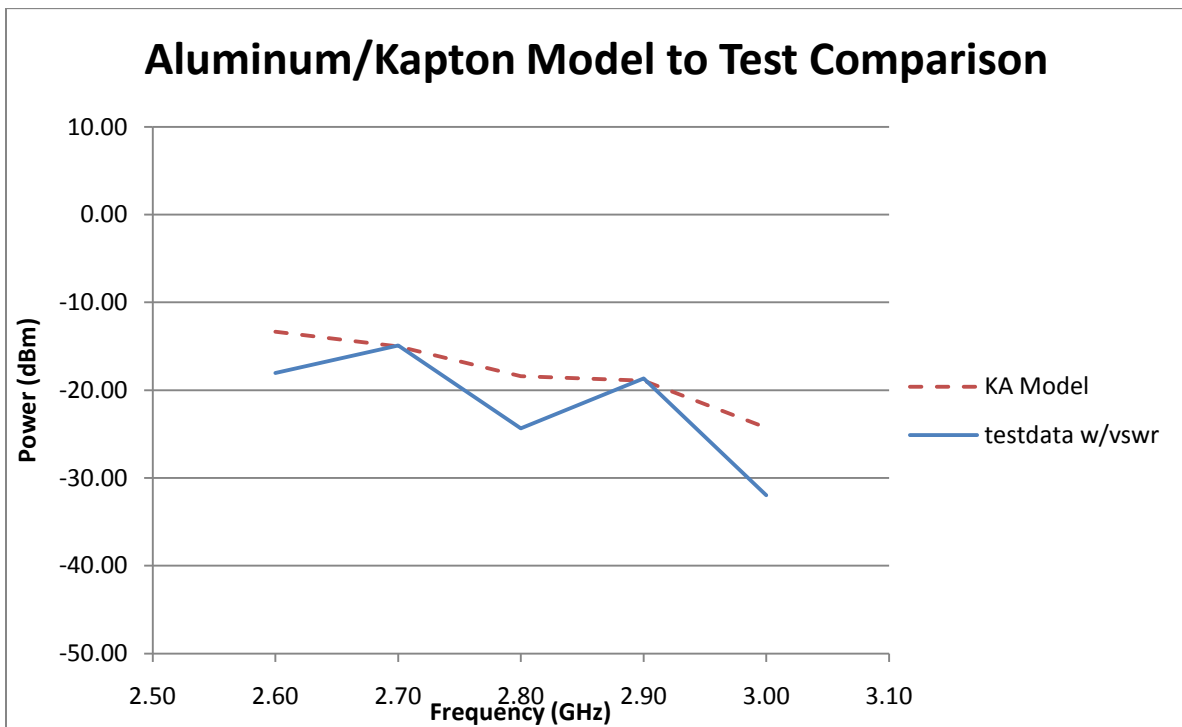
Figure 26. Aluminum with Kapton[®] layer - power received S-band.
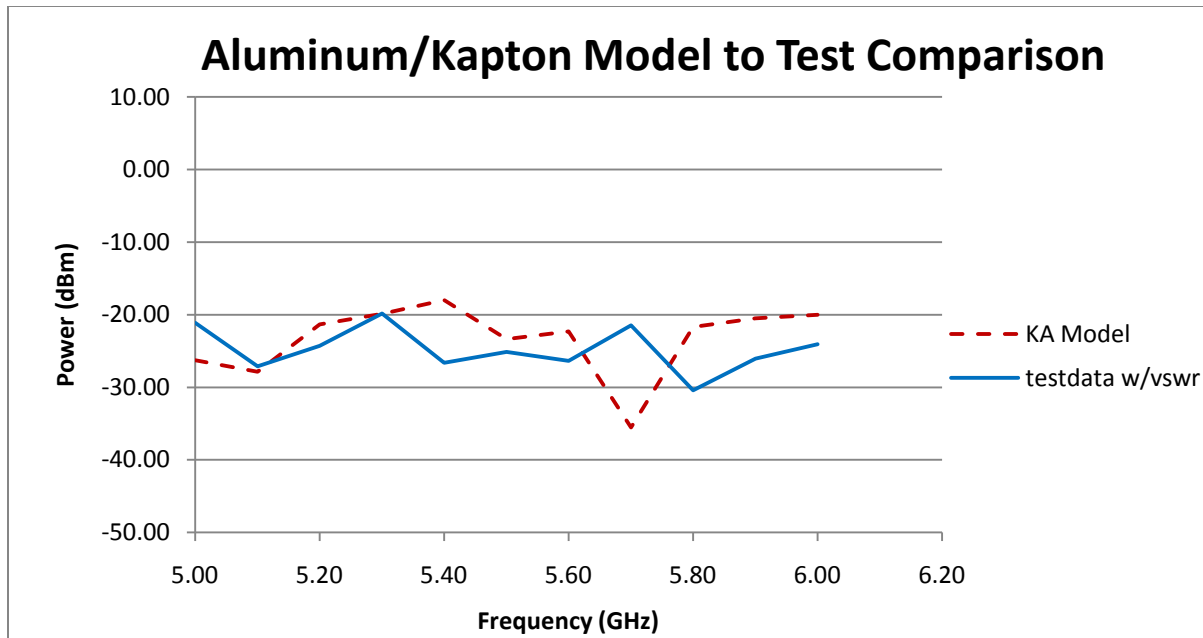
Figure 27. Aluminum with Kapton® layer - power received in the C-Band.

Reasonable prediction of peaks over a wide range is shown with this implementation of an aluminum shell with a separate impedance sheet representing the Kapton® surface impedance properties. Another dominant difference between the model and the physical test model is the application of an antenna as a pattern instead of using the actual antenna in the model.

It was not feasible to implement the double layer CAD model in the higher order MoM tool with the number of unknowns limited to 80,000. Techniques to implement Kapton-lined aluminum structure in that tool are discussed in the equivalent layer section.

4.3.1.2 Three Layer Model - Kapton®-Foam- Kapton® Layer

To implement the second layer of Kapton®, another layer was added to the CAD model at the same spacing as the ½ inch foam. The foam itself has an intrinsic impedance close to free space and was modeled as such. Variations in the aluminum wall implementation were also

90

pursued. Identical results were achieved when the outer wall was implemented as a lossy metal and as an impedance representative of aluminum. Figure 28 depicts the Kapton®-Foam-Kapton® layers and the composite model used within FEKO.

The aluminum foil outer layer and acoustic blanketing layers were represented within FEKO as described below:

- o The fairing outer walls were modeled as a single layer lossy metal with a thickness representing the industry aluminum foil that lined the prototype fairing (0.127 mm thick).
- o The Kapton® acoustic blanket sheets are modeled with a surface impedance based on industry data at the model frequency.
- o The gaps between the impedance sheets represent the foam layer.
- o Free space is required on both sides of the impedance sheet thus a thin layer of free space is introduced between the Kapton® layer and the aluminum foil outer layer
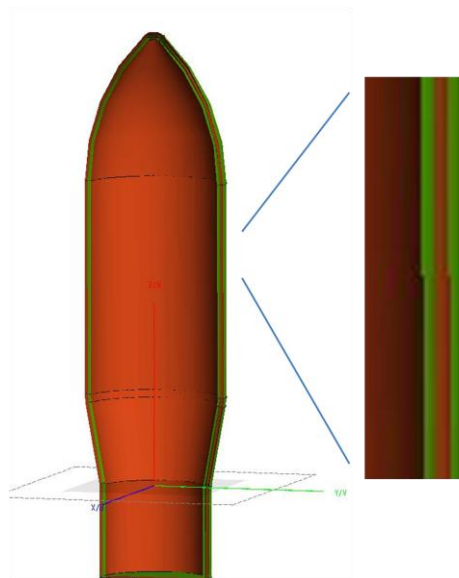
Figure 28. FEKO model with layered acoustic blankets.

Figure 29 shows a comparison of received power between the computational and the test results[114]. The data compares well, with the average variation of 2.43 dB from test data. This is reasonable result given uncaptured variations present in the test set-up. The selection of this frequency range is related to the waveguide measurements used in the equivalent one layer approach described in the following sections.

Comparison of Received Power Three Layer Model to Test Data
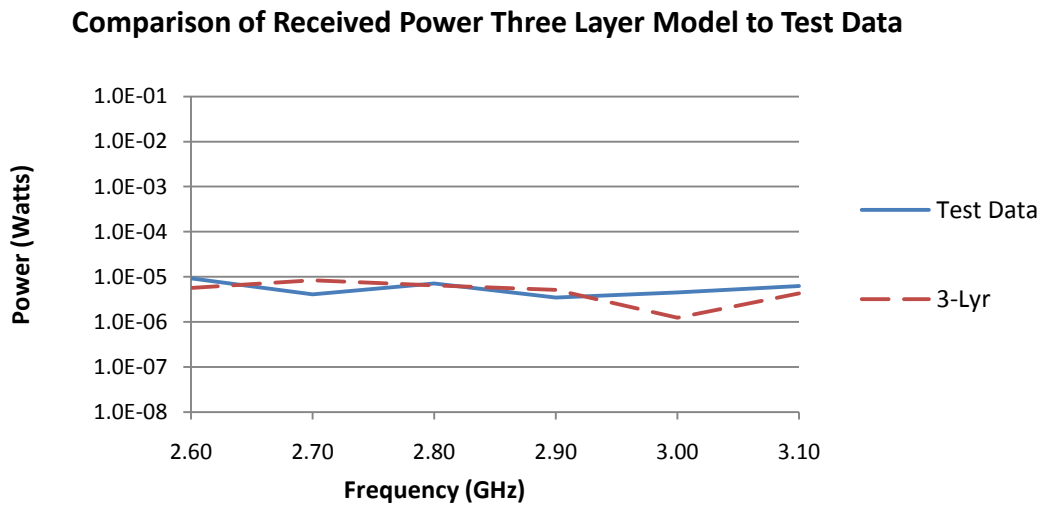
Figure 29. Aluminum shell with Kapton$^{®}$-Foam- Kapton$^{®}$ layer.

4.3.2   Equivalent Layer Models

In the following models equivalent impedances and/or material properties are developed in algorithms outside the CEM tools. These models are then used with the appropriate tool MLFMM or HO MoM to improve computation efficiency and accuracy. The first equivalent model is used with the Hallet Redell method described in Section 2.7.3 and the second equivalent model is a new application of the NRW technique (Section 2.7.4).

4.3.2.1 Hallet Redell Impedance Model with Higher Order MoM

The first equivalent impedance technique considered is similar to that described in [20] to determine the equivalent reflection coefficient for layered dielectrics. In this case, however, an equivalent impedance is represented using permittivity, permeability and conductivity of each layer with perpendicular incidence field assumptions as detailed in Section 2.7.3. This method has heritage with the launch vehicle industry when coupled with a power balance technique to determine an average field in the fairing cavity [24]. Applying this technique within a CEM tool is new.

4.3.2.1.1 Theoretical cone and cylinder model – multilayered model

The first model considered is the theoretical cone and cylinder shown in Figure 30 developed as a precursor to the physical fixtures to compare the Hallet Redell average field technique based on equivalent impedance and surface area in Section 2.7.3 with the CEM tool predictions using the same impedance for the walls derived in (80) in both cases [115]. This model is briefly discussed here to show the equivalent impedance technique in a detailed blanket and composite structure.

Figure 30 Cone and cylinder model

The walls were constructed of multiple layered blankets and the exterior was a composite. The wall and acoustic blanket layers are shown in Figure 31 and are similar to the three layer blanket test case presented in this chapter with the exception that the outer fairing shell is a graphite composite. The impedance model represents a typical fairing acoustic blanket lining a composite fairing. The blankets consist of a layer of Kapton® film overlaid onto melamine foam with another layer of Kapton® film. The excitation is the same horn pattern used earlier in this chapter, and the field distribution obtained within the fairing was compared to that predicted by the Hallet Redell model discussed in section 2.53. The model parameters include a transmitter frequency range of $5 - 6$ GHz and an input power of 10 Watts [116] [115].
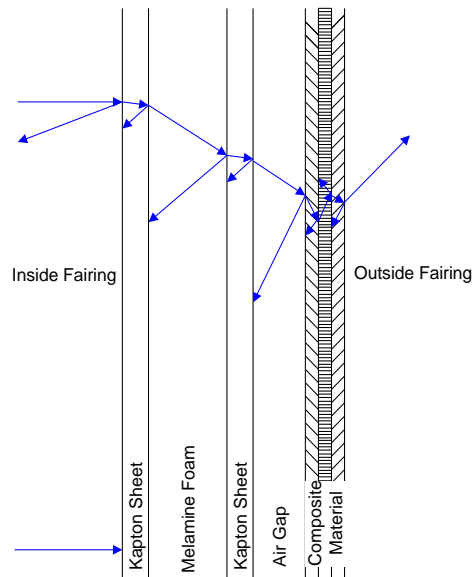
Figure 31 Layered lining of model fairing [115].

An equivalent layer impedance starts with the outermost composite layer and combines with the next outermost layer of Kapton® (80). This impedance is then used as the new outer

layer and combined with the next outermost layer of foam with the same equation. Finally, this impedance is then combined with the inner Kapton® layer to obtain the final equivalent impedance. This final blanket impedance shown in Figure 32 is used for the impedance sheet parameters in FEKO to obtain the field distribution and used in conjunction with the total blanket surface area for the Hallet Redell average field method in (81) to predict an average field in the cavity from 5 to 6 GHz.
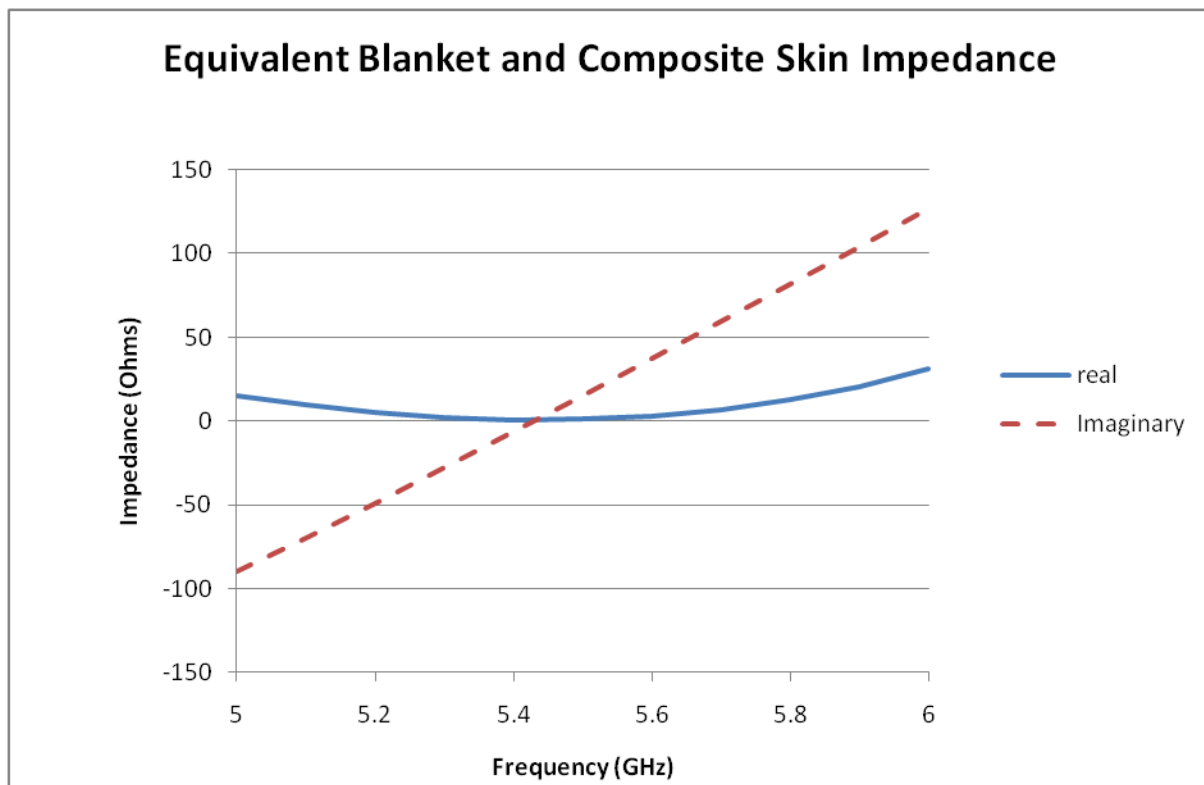
Figure 32. Equivalent impedance of multi-Layer blanketed composite cavity (fairing wall).

The CEM model predicted maximum fields that were three to four times higher than those of the average Hallet Redell method for the same skin impedance. As there was no physical comparison case, this work showed the need for further research and prompted the test

to model comparison studies in this dissertation. The equivalent impedance techniques shown here are used for various fairing models and the results are compared with test data.

4.3.2.1.2 One layer Kapton/aluminum model

The equivalent surface impedance for the test model with a single layer of Kapton® lining an aluminum shell was determined using the same process of the previous section. The resulting equivalent impedance was implemented in the HO MoM and MLFMM single layer models developed in the last chapter. The impedance sheet MLFMM model could not be used due to convergence issues with reflective structures as was the case using just an aluminum shell discussed in the previous chapter. Results obtained when this equivalent impedance was implemented in the HO MoM tool (WIPL-D) are shown in Figure 33. The results for the received power are compared with the Hallet Redell model, which shows a bounding case for the peaks. A reasonable correlation of peak frequencies is seen.
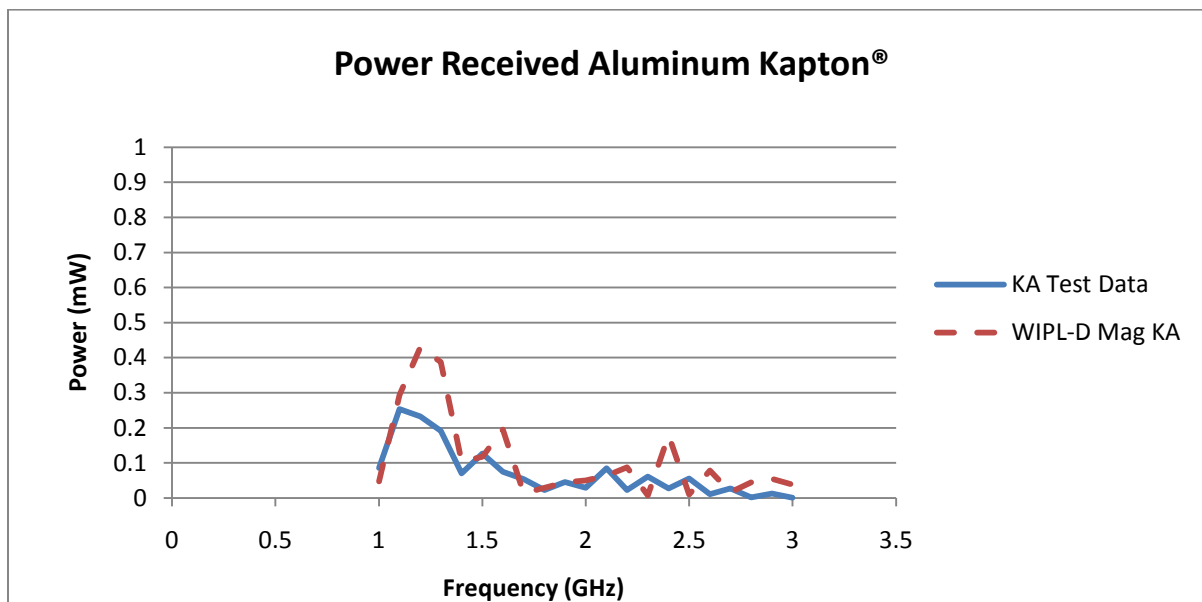
Figure 33. Power received for an aluminum fairing with Kapton® layer.

96

In this HO MoM model, the antenna is implemented in the model which adds to the complexity, but gives a better correlation with test data.

4.3.2.1.3 Kapton® Lined Aluminum Shell Model with load

The spacecraft aluminum load was added to the Kapton® lined aluminum distributed impedance model described in the previous section. Significant changes in the mode structure were observed with the addition of the spacecraft load as seen in Figure 34 as compared to the unloaded case.
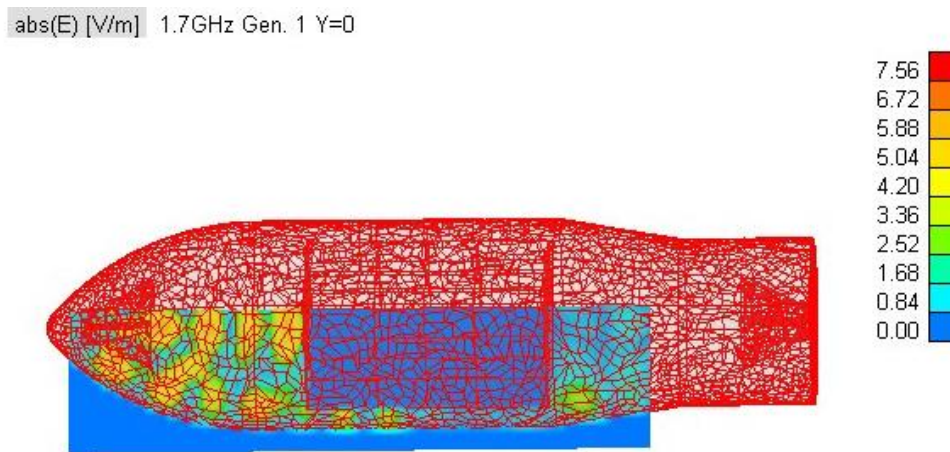
Figure 34 Aluminum fairing with Kapton® lining and PEC spacecraft.

Figure 35 shows that the null space solution common to EFIE solvers forms at some frequencies where resonances are present in the inner cavity. Mitigation of these effects is discussed in the following chapters. It will be shown that these effects are a major problem for

prediction of the inner cavity fields and determining shielding effectiveness (discussed in CHAPTER 6).
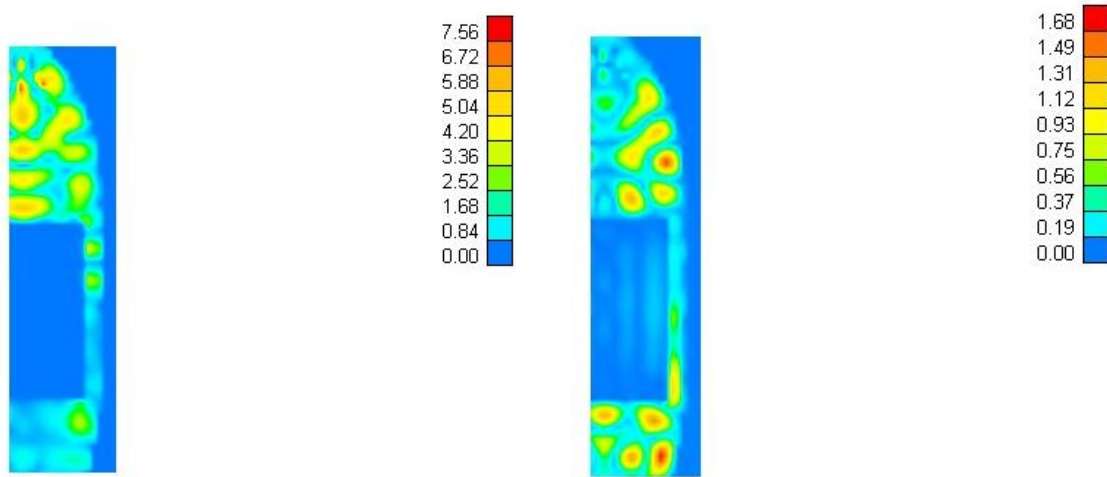
Figure 35. Lined fairing with load showing internal fields in PEC at 1.7 GHz and EFIE solution fields at 1.9 GHz.

Figure 36 reveals good correlation between the equivalent impedance   model and test cases using the Hallet Redell impedance models. The loaded case fields are consistently lower than the unloaded case with the peaks approximately 6 dB less than the unloaded case.

Received Power Loaded Cavity
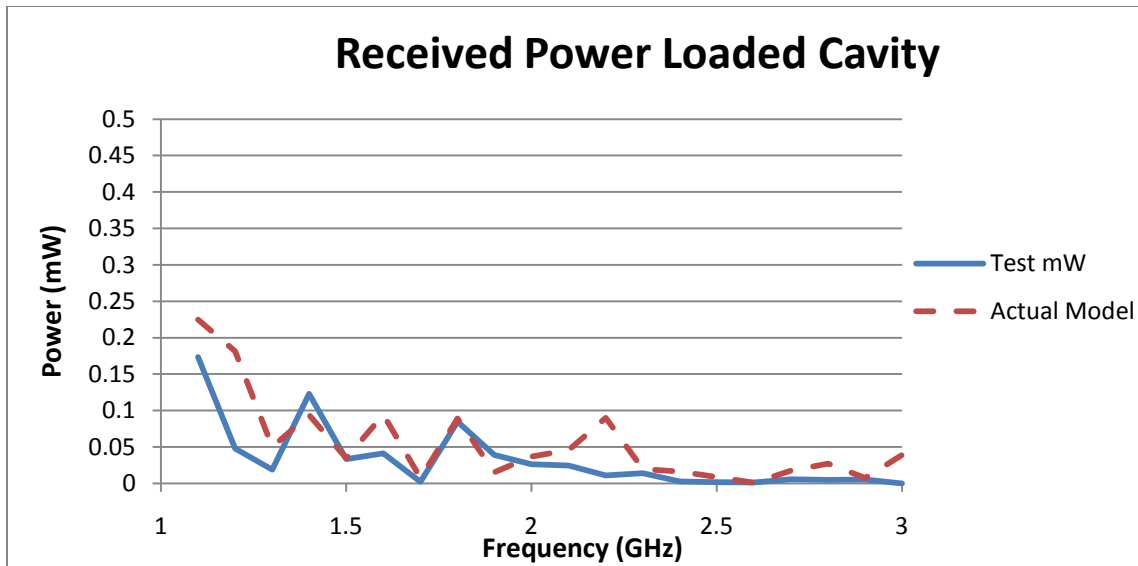
Figure 36. Received power in an aluminum fairing with Kapton® lining with a spacecraft load.

Good correlation is again achieved between test and simulation peaks. Beyond 2 GHz, reflections due to cavity walls caused more losses in the test case. The VSWR was not re-measured with the load in the cavity, but was likely affected by a large reflective surface near the antenna aperture.

4.3.2.2 NRW Equivalent Single Layer Model

It is desirable to further reduce the required computational resource and run-time requirements of the three layer electrically large cavity simulation by using an equivalent one layer model. Another reason to form a one layer equivalent model is the limited availability of vehicle CAD models with blanket configuration information. The model in the Hallet Redell method section is not effective for thicker blankets considered in this section due to perpendicular incidence assumptions in that model. Accordingly a new method is implemented using an application of the NRW technique presented in Section 2.7.4. It should be noted that the following equivalent layer technique is not needed for simulating waveguide structures in

general as there are finite element codes available that precisely model these layers and complex materials in waveguide structures with no simplification. This effort uses the waveguide equivalent model to later implement the layered material effects in the computationally intensive electrically large cavity structures where dimensions can be greater than 100 times the transmit wavelength. Parts of the work for this dissertation that follow have been published in [23].

4.3.2.2.1 Methodology selection

The NRW measurement technique could not be applied to the Kapton only blanket as the sample was too thin to make accurate measurements. Application of the NRW technique is explored in the three layer blanket sample case. The absorbing impedance sheets used in the three layer model require a layer of free space on either side; consequently, to obtain a one layer model a different material representation is required that can readily be combined with the metallic outer layer. The difficulty in representing the entire vehicle in one layer is the contrast between properties of the aluminum layer and that of the acoustic blankets. Accordingly, an option was used to apply the blanket properties as a coating to the metal outer layer. Material properties of the lossy metals and dielectrics are available in the FEKO material tree. Dielectrics can then be selected as a thin dielectric sheet (TDS) with specified thickness and a coating to a metal layer developed with a one layer TDS. The TDS is implemented within FEKO in a similar way as the impedance sheet in (75) with the Z_s term described Section 2.7.1.

A TDS is required to be geometrically or electrically thin (approximately 1/10 the smallest element or wavelength respectively). Due to this requirement, an inherent limitation is often encountered in the computation when the automatic mesh routine generates fine elements to accurately characterize the respective geometries. However, if the coating is geometrically small

with respect to the majority of the elements, the geometrically thin constraint driven by these finer elements can be effectively ignored in the model solution. A FEKO utility will perform a validate check, and will return a solution with warnings only. It is also important to note that the electrically thin constraint is relative to a wavelength in the interfacing medium, but the layer does not have to be electrically small relative to a wavelength of the layer itself [117]. Nevertheless, it is often the situation that the actual thickness of the blankets cannot be represented in a coating, and an equivalent method must always be demonstrated and evaluated.

4.3.2.2.2 Sample S-parameter measurement

The single layer coating model constraint drives the need to alternately represent the three layer blanket model in a waveguide with a one layer TDS. The Nicholson Ross Weir (NRW) technique is used to derive an equivalent permittivity of the entire layered blanket using S-parameter measurements. A blanket sample was placed in an S-Band waveguide. The S-parameters were then measured with a vector network analyzer using a test fixture as shown in Figure 37. These parameters were then used in an equation to determine the transmission coefficient and then used in equation (83) to obtain an approximate value of the equivalent permittivity of a homogenous sample with the same length. As most launch vehicle blanketing materials are non-magnetic, setting the permeability, μ_r, to one simplifies the permittivity determination. Moreover, the TDS implementation requires the permeability to be continuous with the surrounding media.

$$\varepsilon_r = \frac{\lambda_0^2}{\mu_r}\left(\frac{1}{\lambda_c^2} - \left[\frac{1}{2\pi L}\ln\left(\frac{1}{T}\right)\right]^2\right) \qquad (83)$$

where, λ_0 is the free-space wavelength for the desired frequency, λ_c, is the waveguide cut-off wavelength, L is the sample length, and T is the transmission coefficient determined by the measured S-parameters [47].

Figure 37. Material sample test fixture.

Determining the permittivity of a homogeneous sample using waveguide measurements and computational models has been verified as being effective in the literature [48][103]. In this paper, the NRW technique is used to determine a first level approximation of an equivalent permittivity that would apply to a dielectric block with the same measured S-parameters, although the sample itself is layered. Full wave analysis is then used to modify the permittivity at each frequency until a sufficiently close approximation of the S-parameters is found. This equivalent permittivity data is then used to construct the coating in the one layer model of the fairing.

4.3.2.2.3   Waveguide sample models

A three layer MoM model was first constructed in FEKO as shown in Figure 38 to emulate the actual S parameter measurement set-up.
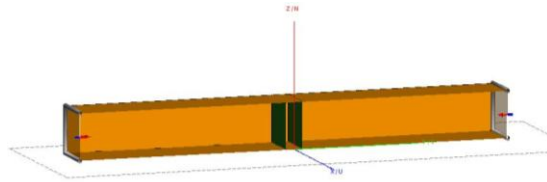
Figure 38. FEKO MoM model of three layer fairing blanket sample.

The permittivity and conductivity of each Kapton layer was characterized as a dielectric with the thickness accounted for in the TDS implementation. The foam was represented by air as in the three layer fairing model. It is straightforward to convert the model with separate layers into a multilayer TDS which only uses one face in the geometry representation. However, the multilayer TDS cannot be represented as a coating to a metal. Hence, representation of the material in a single TDS is pursued.

The finite element method (FEM) was employed to verify that the NRW derived equivalent properties derived with (83) represent the S parameters when the waveguide is filled with a homogeneous dielectric block. The FEM model is shown in Figure 39. In this instance the regions defining the boundary of the block are represented as the dielectric material and implemented with permittivity parameters with respective loss tangents.
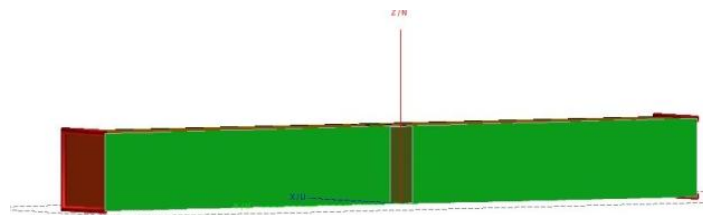
Figure 39. Equivalent homogeneous dielectric block (FEM).

The parameters were then implemented with a TDS single layer MoM model as shown in Figure 40 for final implementation into the fairing fixture.
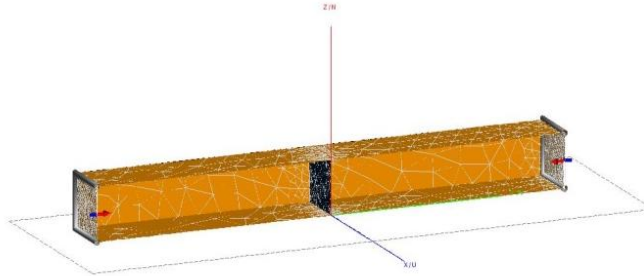
Figure 40. TDS layer in waveguide (MoM).

When meshing constraints require a reduced thickness in the TDS layer, a thinner layer can be established by changing the sample length in (3) to achieve a corresponding permittivity. Figure 41 shows a comparison of test, MoM separate layer model, FEM dielectric block model, and the final single layer TDS with original and reduced sample thicknesses. The FEM model required some parameter optimization. The material parameters can then be adjusted to provide a closer match to the original S_{21} measurements.

Model S21 Comparison
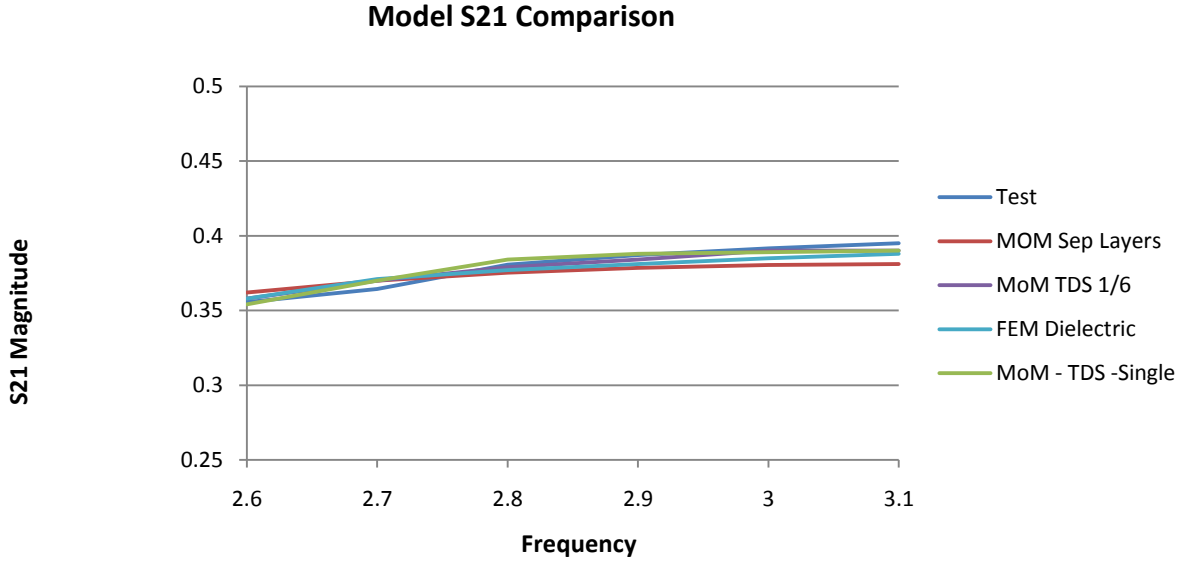
Figure 41. Comparison of the waveguide S-parameter test data to the FEKO models.

4.3.2.2.4   Equivalent one-layer vehicle model

Results in Figure 42 shows that incorporation of the permittivity and loss tangent derived from the NRW waveguide technique into a TDS coating of a single metal layer in the vehicle model provides a reasonable correlation to the test data, as does the three layer model. First, the original sample thickness results are applied directly to the coating properties. Due to layer wavelength related constraints, however, the thickness of the coating is set at three skin depths of the Kapton® layer. A closer approximation is achieved by using (83) to provide a different permittivity and loss tangent to correspond to a sample thickness adjusted to a smaller value. Results shown are for a TDS length of 1/6 of the original sample which varied from the test results an average of only 2.5 dB.

Received Power
Comparison of Equivalent Impedance Techniques
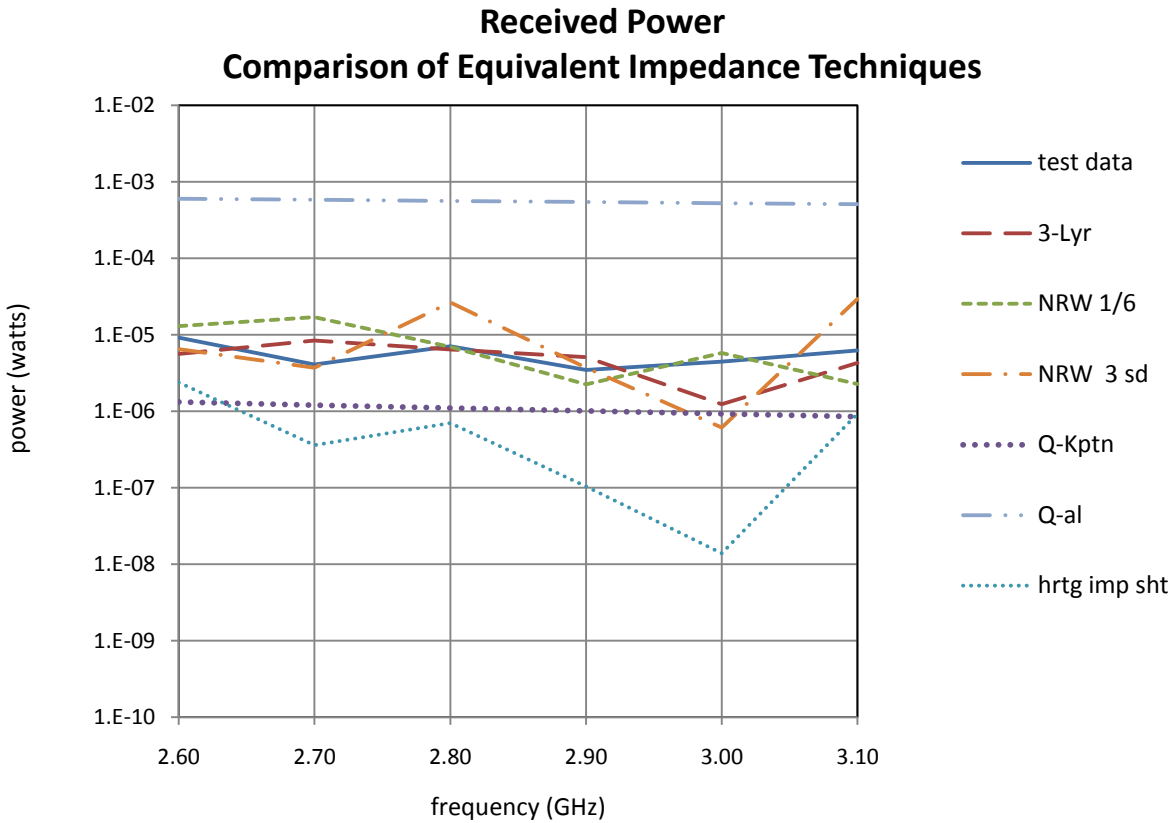
Figure 42. Comparison of received power using the single layer and the three layer fairing models with the test data.

The upper and lower bounds represented in Figure 42 are based on cavity Q equations for aluminum and blanketed walls [24]. It is evident that the FEKO models provide significantly better results than the approximations that are generally relied upon. It should be noted that the primary intent of the Q related approximations are to evaluate chambers with very conductive walls with small absorbers present, but the application of these equations are often extended to cavities with more complex material configurations.   The Hallet Redell   method based impedance model is also shown for comparison. It is clear that the perpendicular incidence assumption is not valid for non-electrically thin layers.

The efficiency benefits of using MLFMM in a three and one layer model as compared to MoM are shown in Table 2.

Table 2: Memory/Run Time Comparison

Method	# Unknowns	CPU Time per Process (hrs)	CPU Time Total (hrs)	Peak Memory (GB)
MoM 1 layer	124,377	21.2	339	115
MLFMM 3 layer	372,622	3.9	60.9	10
MLFMM 1 layer	124,377	0.066	1.1	2.2

4.4   Summary

This chapter shows that the fields due to internal sources in fairing structures with complex blanketing materials can be modeled effectively with equivalent impedance techniques in a multilayer MLFMM model as well as the HO MoM model. The MLFMM model was ideal for multilayer absorbing configurations, while the HO MoM model was most effective for reflective thin layers.   This is important because methods for quantifying fields due to transmission within a vehicle fairing have largely relied on general reverberation chamber average power approximations. The models discussed here included multilayer CAD inputs with each blanketing layer modeled separately, as well as equivalent single layer models. Considering the full three layer blanket models, both methods appeared to have an improvement over the power approximation techniques for a launch vehicle with simulated acoustic blankets. The Hallet Redell method showed reasonable results for the single lined case. The equivalent impedance approach for the full blanket utilized a novel application of NRW formulations to

derive an equivalent permittivity of the three layer configuration. Although impedance sheet direct representation of individual layers provides reasonable results, as the number of layers and/or size of the vehicle increases a combined equivalent layer is needed to develop a model that is reasonably computationally efficient.

Note much of this data approximates the test data peaks when viewed over a range of frequencies, exact points at a single frequency are not identified in all cases as slight variations in test configuration can shift the frequencies. Consequently, it is ineffective to use a model at a single frequency even if the transmit frequency is at a single frequency. The next chapter identifies methods of comparison using spatial and frequency variation in composite fairings.

CHAPTER 5. COMPOSITE FAIRING - INNER SOURCE

5.1   Introduction

Composite fairings have become increasingly prevalent in the launch vehicle industry due to their lighter weights which can improve overall vehicle performance by increasing the allowable weight of the payload for a given thrust. The goal of this chapter is to examine fields in a composite fairing cavity from an internal excitation. Applicability of equivalent impedance techniques presented in the previous chapter is explored for a composite structure.

A composite fairing fixture typical of launch vehicle construction is developed and used for comparison. New testing techniques are examined to more closely represent the field distribution in the fairing cavity instead of considering only the received power at one location. Evaluation of the importance of modeling the dielectric antenna support structures is also undertaken. Limitations in testing techniques are also explored.

As any added structures in the fairing will decrease the computational feasibility of the model, examination of statistical comparison techniques used in reverberation chambers is also examined, as well as the applicability of these techniques to the loaded cases. Finally, the effects of blanketing properties regarding peak fields are examined and recommendations on blanketing implementation are made.

5.2   Composite Fairing Fixture - Test Results

5.2.1   Composite Fairing Fixture

A fairing composite model was constructed with a height of 6 feet and a diameter of 2 feet [118]. The scaled fairing fixture model shown in Figure 43 and used for all simulations in this work is ½ to $^1/_7$ the size of typical launch vehicles. The 1.8 m by 0.6 m fairing fixture is

made of two composite fairing halves with tabs at the edges for clamping the fairing enclosure. Two 1 mm 4 ply layers of carbon composite material sandwich a 6.35 mm Rohacell®WF foam core as shown in Figure 44. Rohacell®WF is a closed-cell rigid foam based on polymethacrylimide chemistry, which does not contain any carbon fiber composites (CFC's) and is often utilized in manufacturing advanced composites for aerospace applications [118]. The surface resistivity was measured as 161 mohms. The composite fairing structure was grounded via a metallic flat plate which interfaced with the bottom edges of the fixture. For the RF testing described in this chapter, copper tape was applied to the seams outside the fairing to prevent leakage.
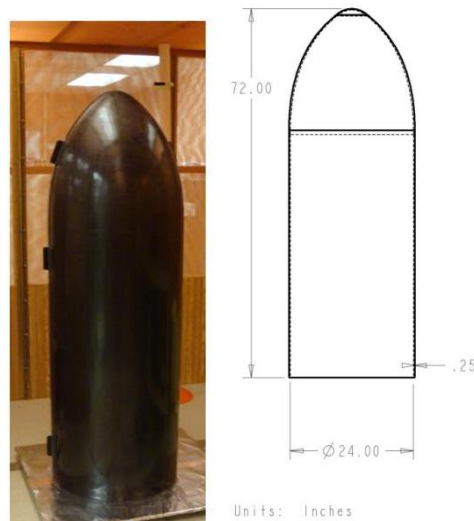
Figure 43. Composite fairing fixture and dimensions.
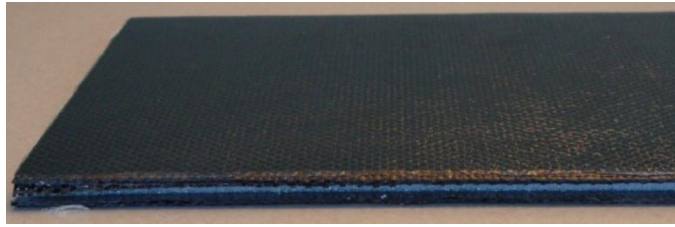
Figure 44. Composite layer sample.

5.2.2   Test Program

To reduce interactions on the cavity resonances from the transmitting and receiving antennas, smaller devices were used than in the metal fairing case. Haigh-Farr S band, model 3106, and C band, model 3107, dipoles were used for transmit and fiber optic field probes were used for receive. A fiberglass mount with 5 cm vertical steps (40 to 110 cm) was used for measurements at multiple locations as shown in Figure 45. Three axis isotropic probes were positioned first at two different outer horizontal positions and moved vertically to quantify the cavity electric field distribution. The probes were then moved to more central positions and the process repeated (see Figure 46). The horizontal probe positions were 0, 9, 16 and - 25cm.

Figure 45.   Composite fairing half test set-up with fiberglass mount and outer probe positions.

Figure 46. Inner probe positions.

The data in Figure 47 shows the repeatability of the data for different passes at the same probe positions. This data shows that the fields are deterministic for a given configuration.

Slight variation between the first pass and the later passes could be contributed to equipment warm-up time.
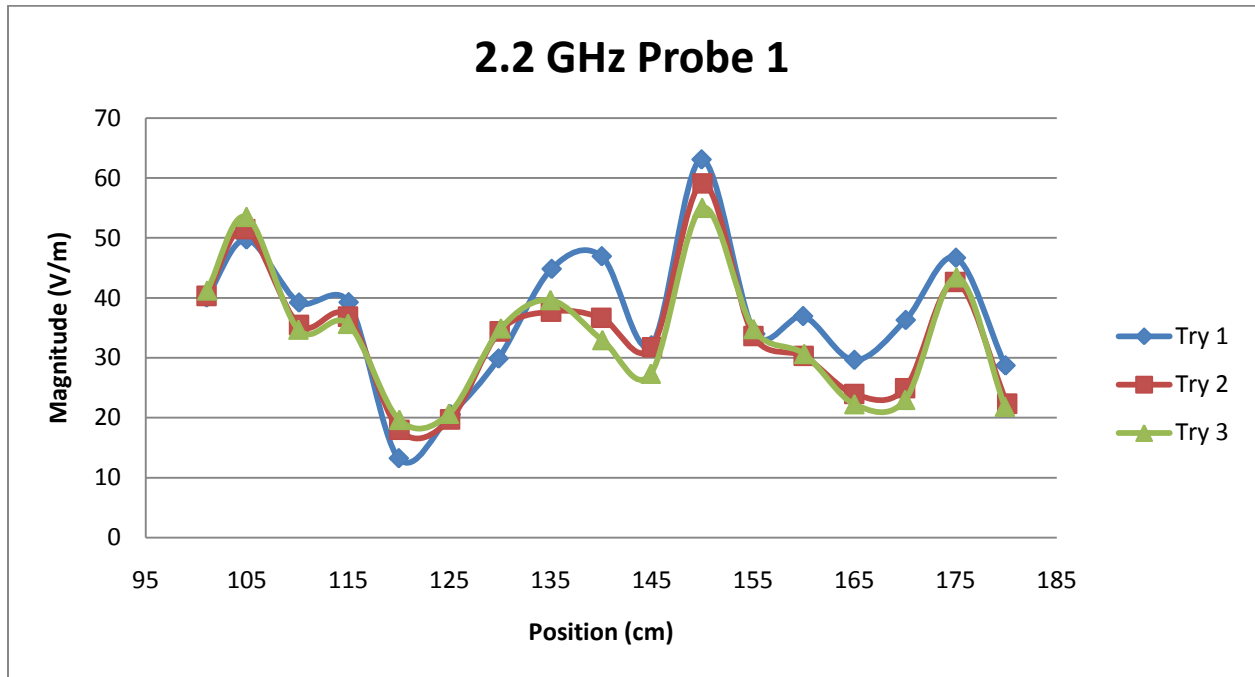
Figure 47. Repeatability data for identical vertical passes at 2.2 GHz.

A sample of the data at three different frequencies is shown in Figure 48. This data reveals the significant variability of the data peaks as the frequency is varied.
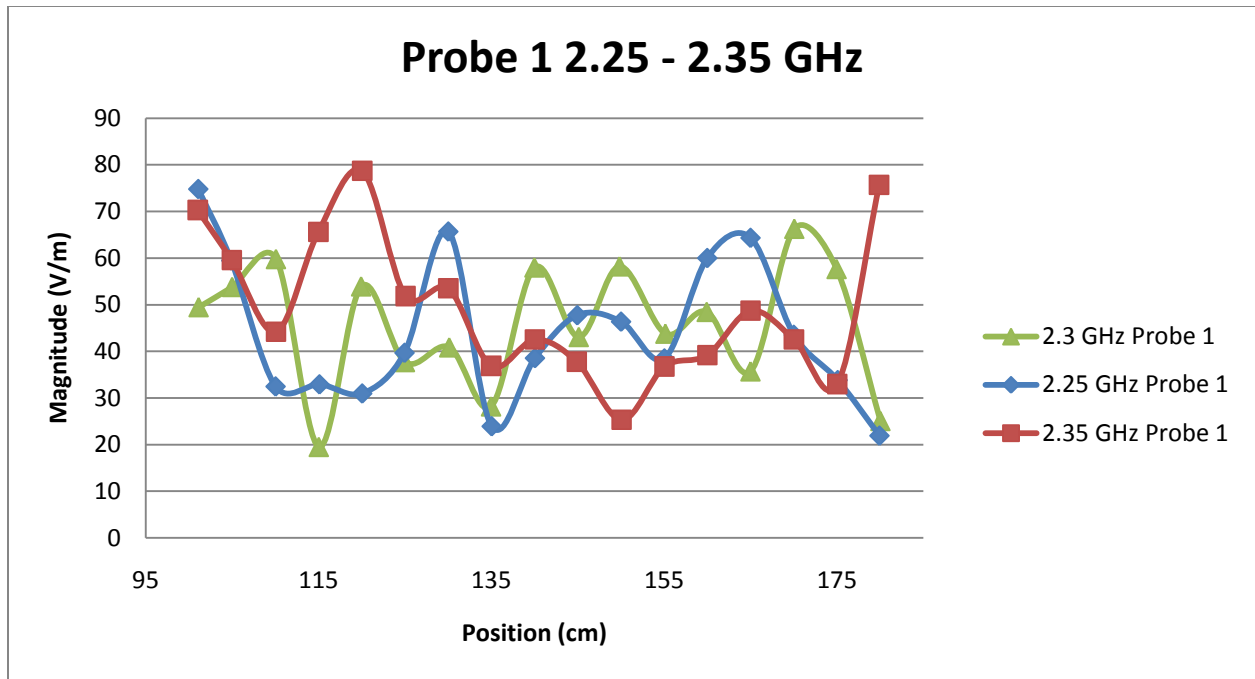
Figure 48. Field variation with a vertical pass at multiple frequencies.

Figure 49 shows the S11 reflection voltage data for the C-band button antenna inside and outside the fairing. The fairing is shown to have considerable impact on the amount of signal reflected. This is because the capacitance to ground changes due to the close proximity to the fairing walls to the antenna. Since the antenna input resistance is influenced by the presence of the cavity and resonances, characterizing the antenna losses in the cavity is essential [119].

C-Band Antenna Voltage Reflection
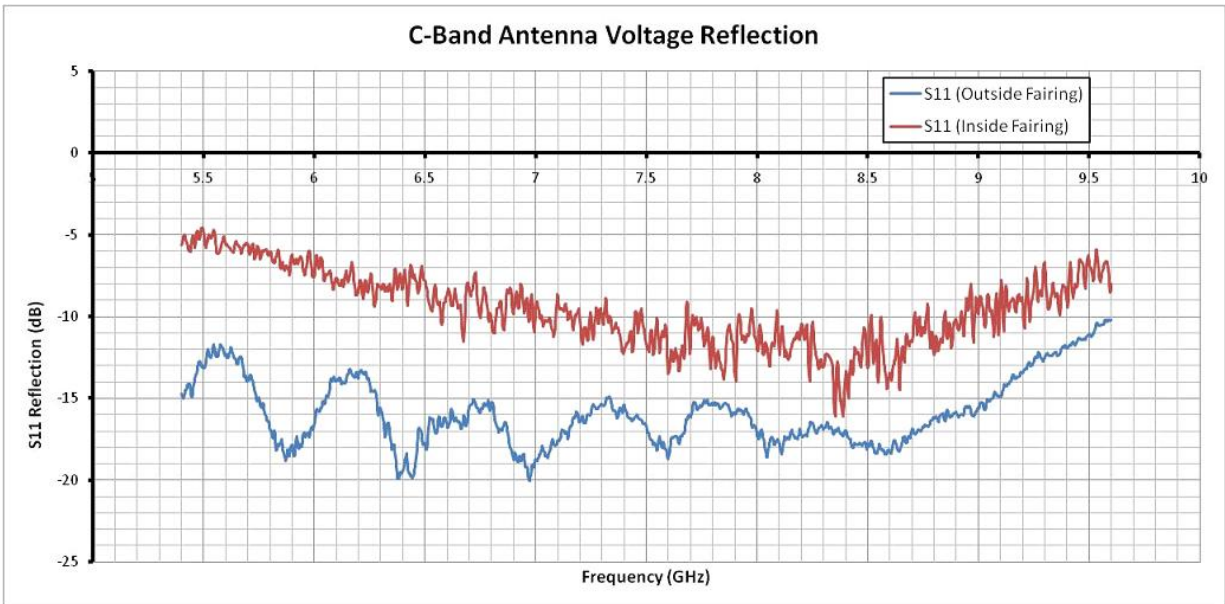
Figure 49. Reflection coefficient for C-Band button antenna in free space and in the fairing cavity.

The three axis probe factor was also assessed and found to decrease sharply (less sensitive) with frequencies approaching the C-Band. To ensure proper readings a larger probe with a flat response across frequencies of interest was used to provide a probe cavity compensation factor. Additionally, it was determined that using a single axis provided more reliable test over less physical area. This is likely due to the fact that the probe necessarily averages over the area, but the model data is at an infinitesimal point. As a final check, the linearity of the probes was assessed by increasing the power and assessing the correlated changes in the measured field. Figure 50 shows the data is linear as the field strength varies as the square root of the power input.
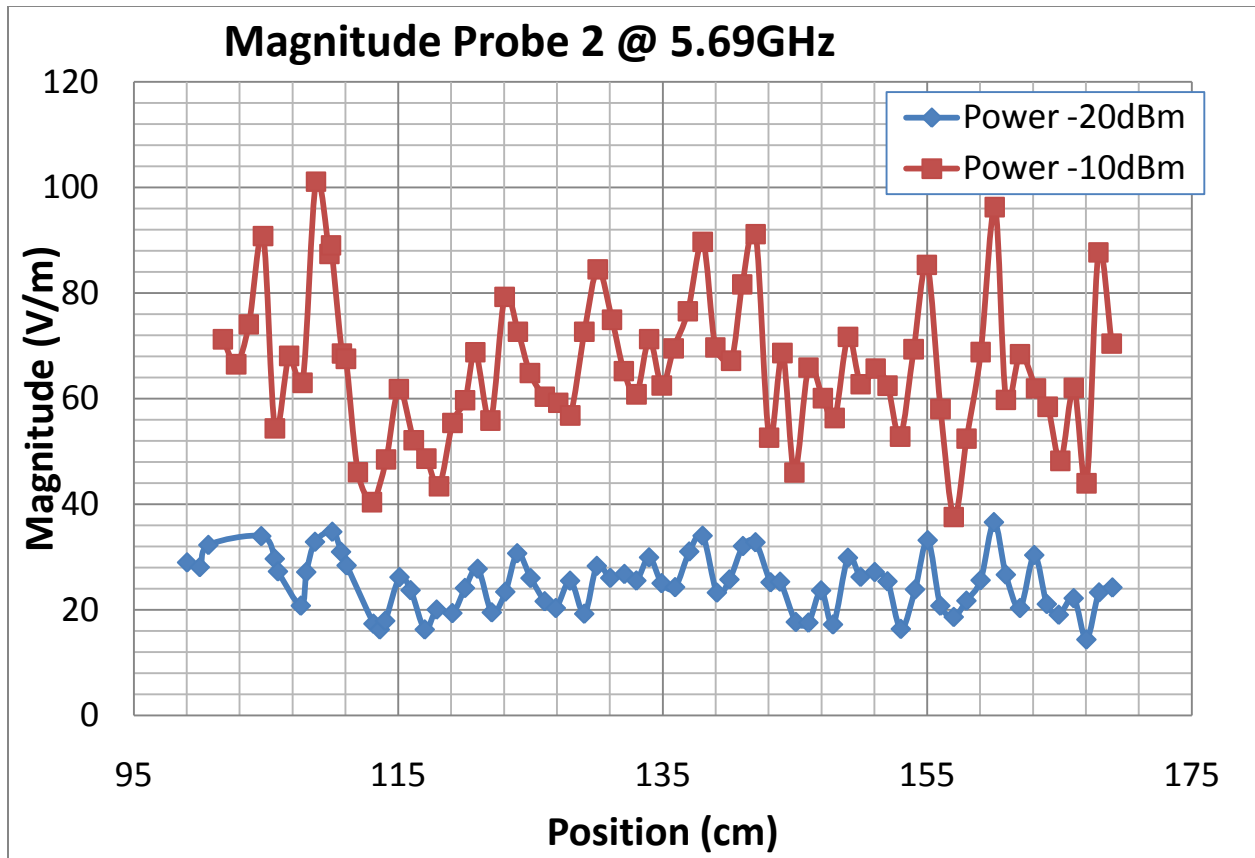
Figure 50. Field probe power response with proportional change in field strength.

5.3   Composite Fairing - Modeling and Simulation

5.3.1   Antenna Model

The dipole antenna models for the S and C bands were constructed in WIPL-D and FEKO. Because the dipole radius was significant, a cylindrical model was constructed. Wire models only allow components in the axial direction eliminating possibly significant interactions in the radial direction. The S-band model is shown in Figure 51. Both the MLFMM model and the HO MoM model were developed, but due to meshing constraints of each program, some variation in the source models exists. The HO MoM model, for instance, requires the plates to have intersecting points, thus the antenna was placed on an easily implementable shape.
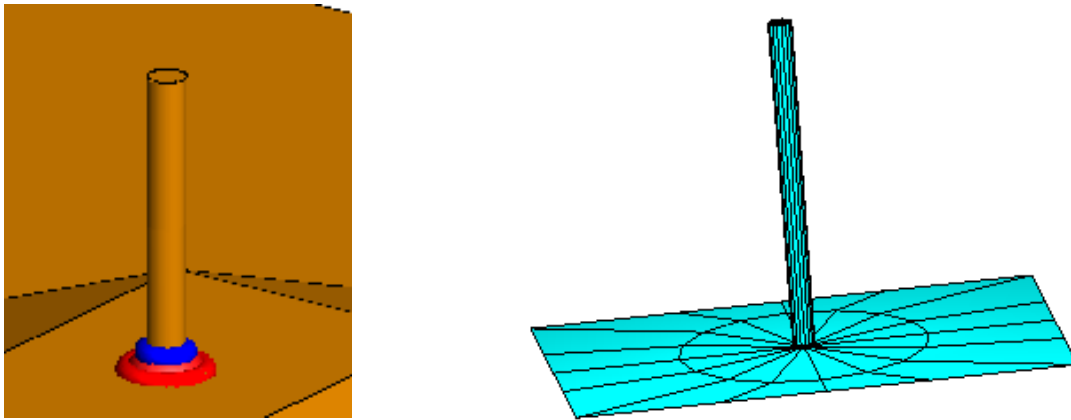
Figure 51.   Antenna cylinder implementation at S-Band in FEKO (left) and WIPL-D (right).

The actual antenna has a plastic antenna cover. The effect of this cover was emulated and compared to the antenna without the dielectric cover as shown in Figure 52.
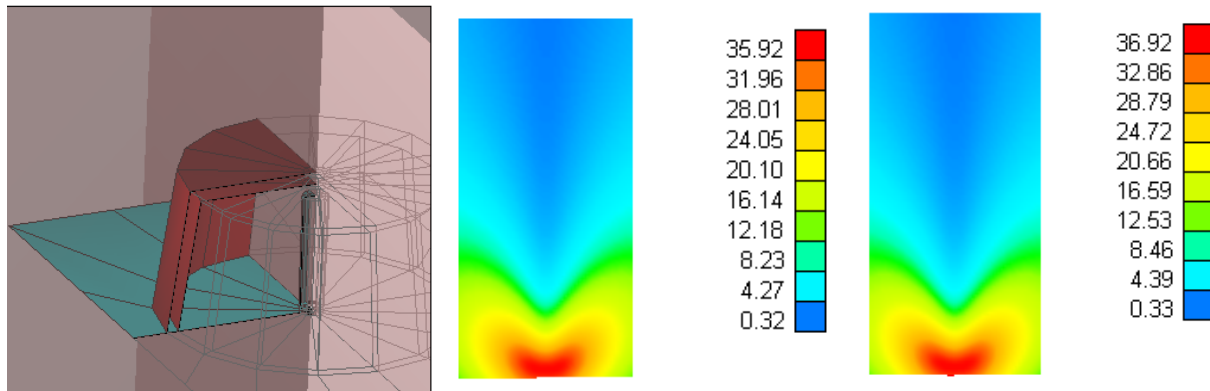
Figure 52. HO MoM Antenna with cover model at C-Band and E-field distributions with (left) and without cover (right).

The antenna dielectric cover was modeled and compared first with air covering then with plastic cover ($\varepsilon_r = 2$). Minimal differences were seen in the results. Detailed studies have shown the influence of these covers on field distribution is minimal, although bandwidth can be

influenced by this covering [120]. The cover was not used during the cavity simulations to decrease the number of unknowns required for the solution.

5.3.2   Aperture modeling

The CAD model of the composite test fixture was imported as a PEC structure. Edge properties were then applied for the HO MoM model to the bottom antenna mount aperture to apply the appropriate boundary conditions as discussed in Section 2.3.   Before this edging is in place, meshing is discontinuous at opening and thus fields are discontinuous across the boundary as shown in Figure 53.
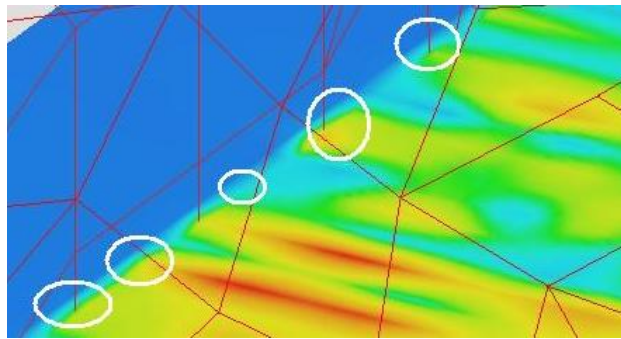
Figure 53. Edge of aperture showing mesh misalignment.

One check to ensure a good model across an aperture is to assign different domains to inside and outside the cavity. The domains represent dielectric properties which in this case are both set to a relative permittivity and permeability of one.   This increases the number of unknowns and thus is only used for checking the model. The fields can then be examined separately for each domain. Good continuity was achieved as demonstrated in Figure 54 [90].
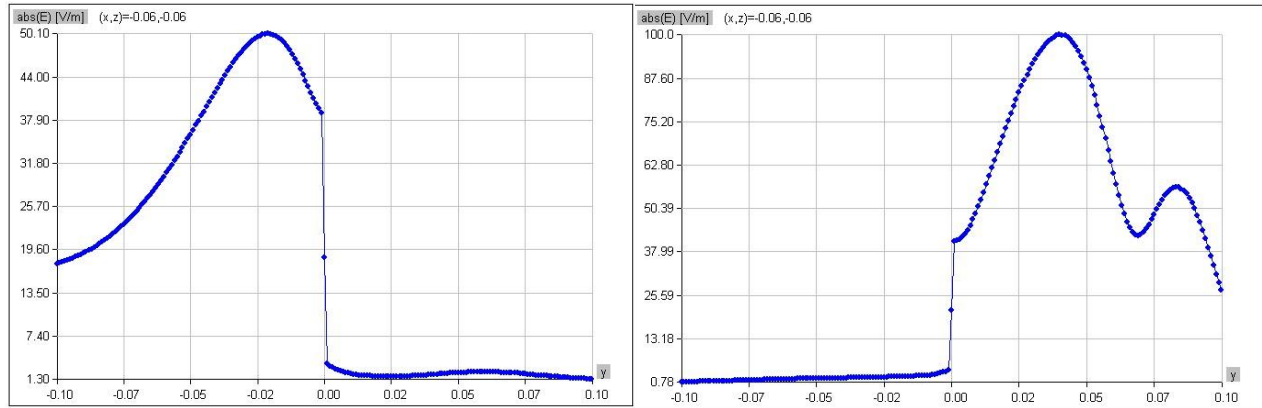
Figure 54. Field continuity for external and internal fields.

5.3.3 Composite Impedance model

Composite materials are not homogeneous. As shown in Figure 44, the composite material of this fairing fixture is layered itself with graphite composite materials sandwiching a foam core. Each outer graphite composite layer is non-homogenous. The layer is made of several composite plies. Each of these plies has graphite fibers held together by an epoxy. The plies are typically placed in different directions to build up the composite layer as shown in Figure 55. The arrows represent the conductive fibers and the white area represents the epoxy. Individual layers will have a dominant conductivity in different directions due to the conductive fiber placement. This crossing of layers builds strength more uniformly and allows for a more uniform conductivity [121],[122]. Complex composite models have been developed in industry to depict the anisotropic behavior [56], but these models are not readily incorporated into electrically large structures. It will be shown in CHAPTER 7 that at lightning frequencies which diminish in the MHz range, this material can be modeled effectively using the measured dc surface impedance. In this study, it is desirable to evaluate the composite at the S and C bands,

119

and techniques are examined which represent the high frequency characteristics of these composite structures while maintaining a computationally efficient model.
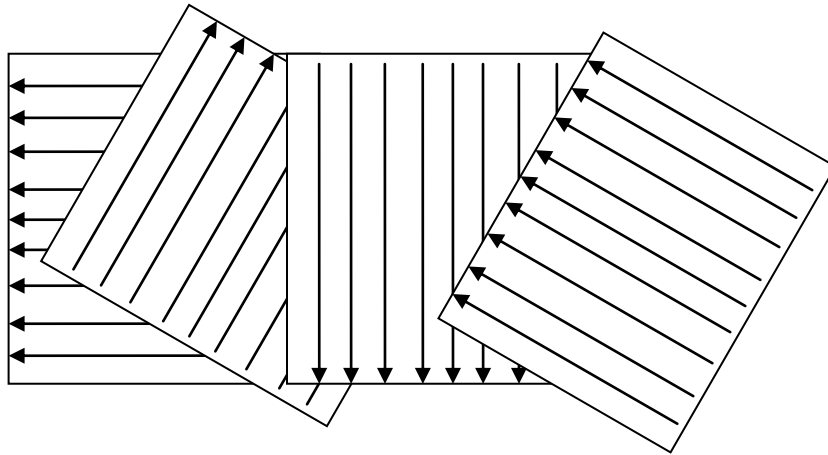
Figure 55. Sample ply lay up for single graphite composite layer.

NRW data was obtained for a single composite layer (4 plies) of the test fixture. The data obtained was then used to approximate equivalent material properties. Additionally, NRW data was obtained for the entire composite construction consisting Rohacell® foam sandwiched by composite layers shown in Figure 44. Using (83) with the relative permeability, μ_r, set to one, the resulting permittivities were calculated. When μ_r was not set to one, unrealistic material property and impedance values resulted. The permittivities and sample thickness values were in turn used to calculate the equivalent surface resistance of the material through techniques in Section 2.7.1. The three layer sample was 0.82 cm thick and the one layer sample was 0.095 cm thick. The resulting impedances are provided in Table 3 below:

Table 3: Complex Impedance

Frequency	3-Layer Sample Impedance	1-Layer Sample Impedance.
S-Band	10.54 – j1.9	8.37 – j5.54
C-Band	0.34 - j1.37	4.71 – j8.76

The side walls of the imported CAD structure in both the HO MoM and MLFMM models were assigned impedance values based on that derived in Table 3 from complex permittivity NRW test data as in the blanketed case.

In addition, a dielectric fiberglass pole was modeled as a long cube with dielectric properties to determine the effect of the fiberglass mount.   Better matching of the magnitude results was achieved with the fiberglass mount at S-band, but the component and statistical results were not improved by adding this mount. As adding dielectrics to models increases the number of unknowns, the empty cavity model was selected for most of the comparisons. Figure 56 shows the comparison of field distributions using the MLFMM and HO MoM models at a single frequency.
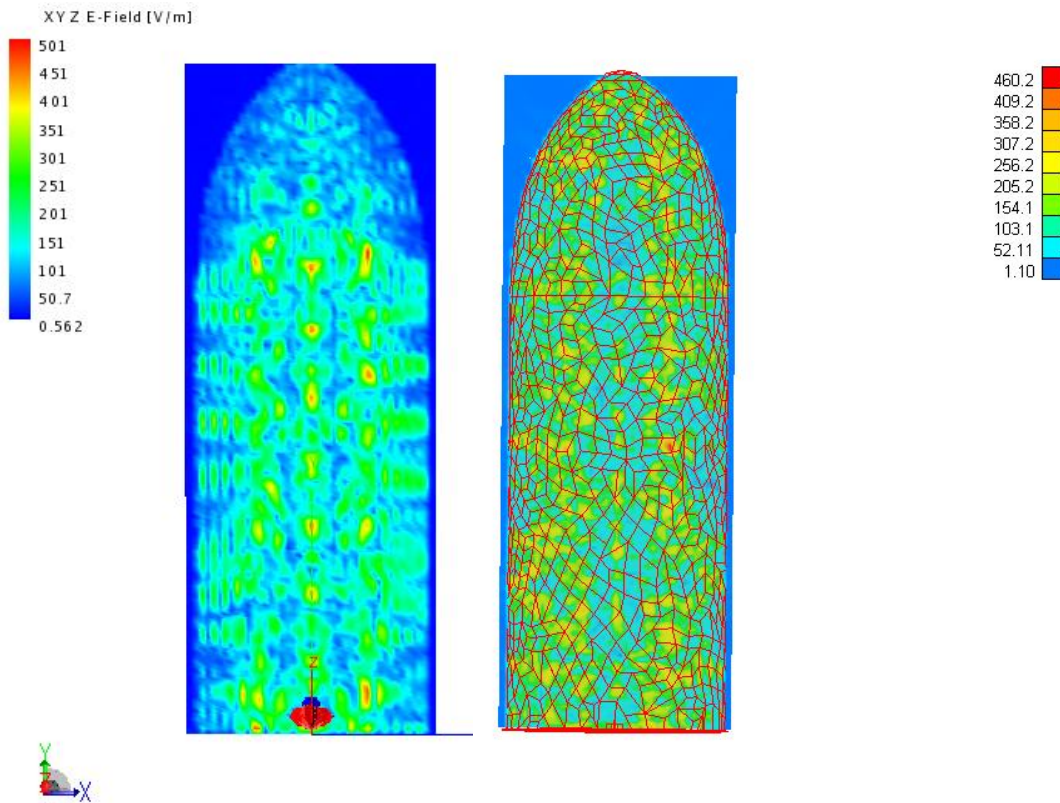
Figure 56. MLFMM vs. HO MoM field distributions or composite fairing at 5.65 GHz (before losses).

Both models were implemented in a single layer impedance model based on the NRW technique described in section 2.7.4. Although the MLFMM EFIE model has some residual (1.11682E-02) and source implementations are slightly different, the models compare well with less than 1 dB difference in peak cavity fields and similar field distribution. However, all impedance comparisons could not be made with the MLFMM model as the residuums were too high for the lower impedance representations (for example, the C-band three layer model). Hence, the majority of the work reflected here is from the HO MoM model. Blanket

comparisons discussed later in this chapter are performed in the MLFMM model as it performs well with absorbing material and is more readily adapted for multiple layers.

5.3.4   Comparison of Composite Model Data to Test Data

Initial composite data comparisons were made for the magnitude of the 3 axis probe data (root sum square of the three axes). Routines were developed within Matlab to average inputs over the probe distance, which are seen in the 3 axis figures with a small averaging distance to keep the graphs at proper scale. However, the probes are approximately 7 cm long and manufacturer recommendations for other than free space conditions are to use single component data. The model data is reported at an infinitesimal point instead of over some probe length, hence better correlation was achieved with single component data.   The vertical component is shown in the single axis figures, but the other components had similar comparisons. Additional comparisons included the use of the three layer composite model versus the single layer composite model with distributed impedance values assigned from Table 3, as well as examining the effects of including the model of the fiberglass pole versus an empty cavity. The three layer composite model results are shown in Figure 57 with the fiberglass pole in the model and in Figure 58 without the fiberglass pole in the model.
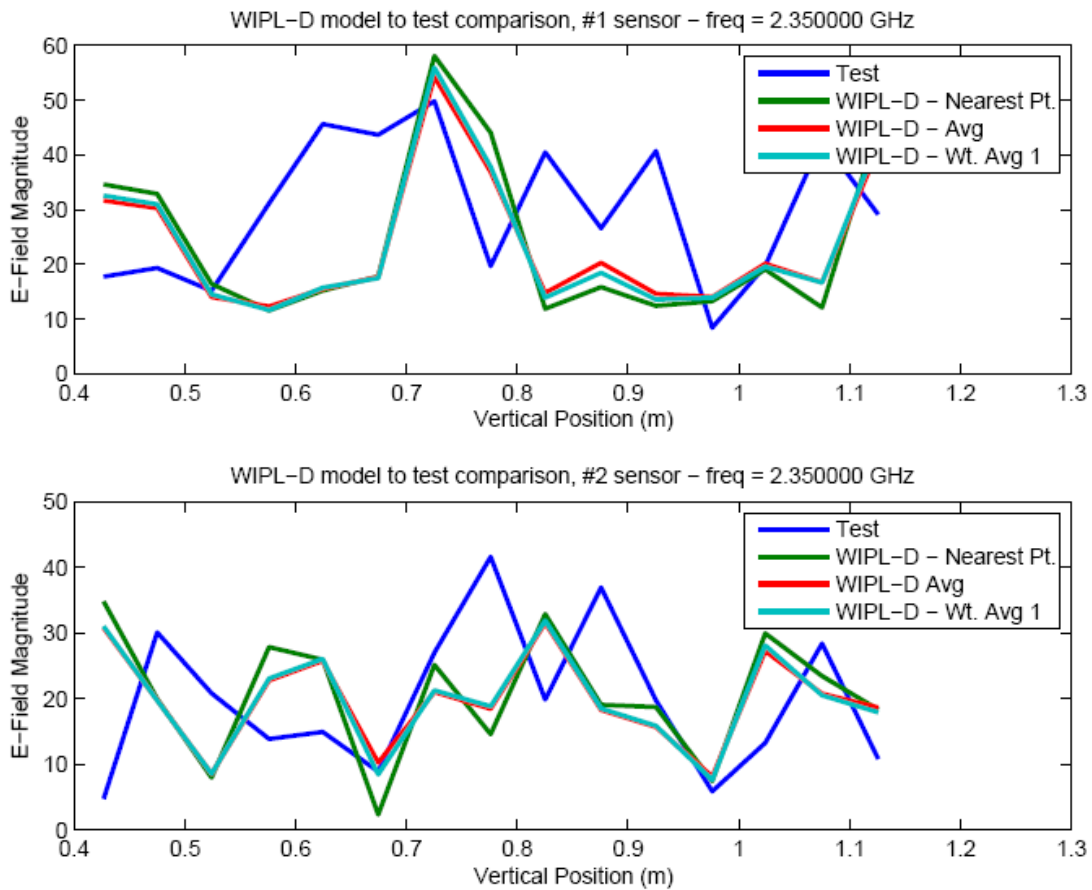
Figure 57. Comparison of the magnitude of 3 axis E-field for composite three layer model with the fiberglass mount.
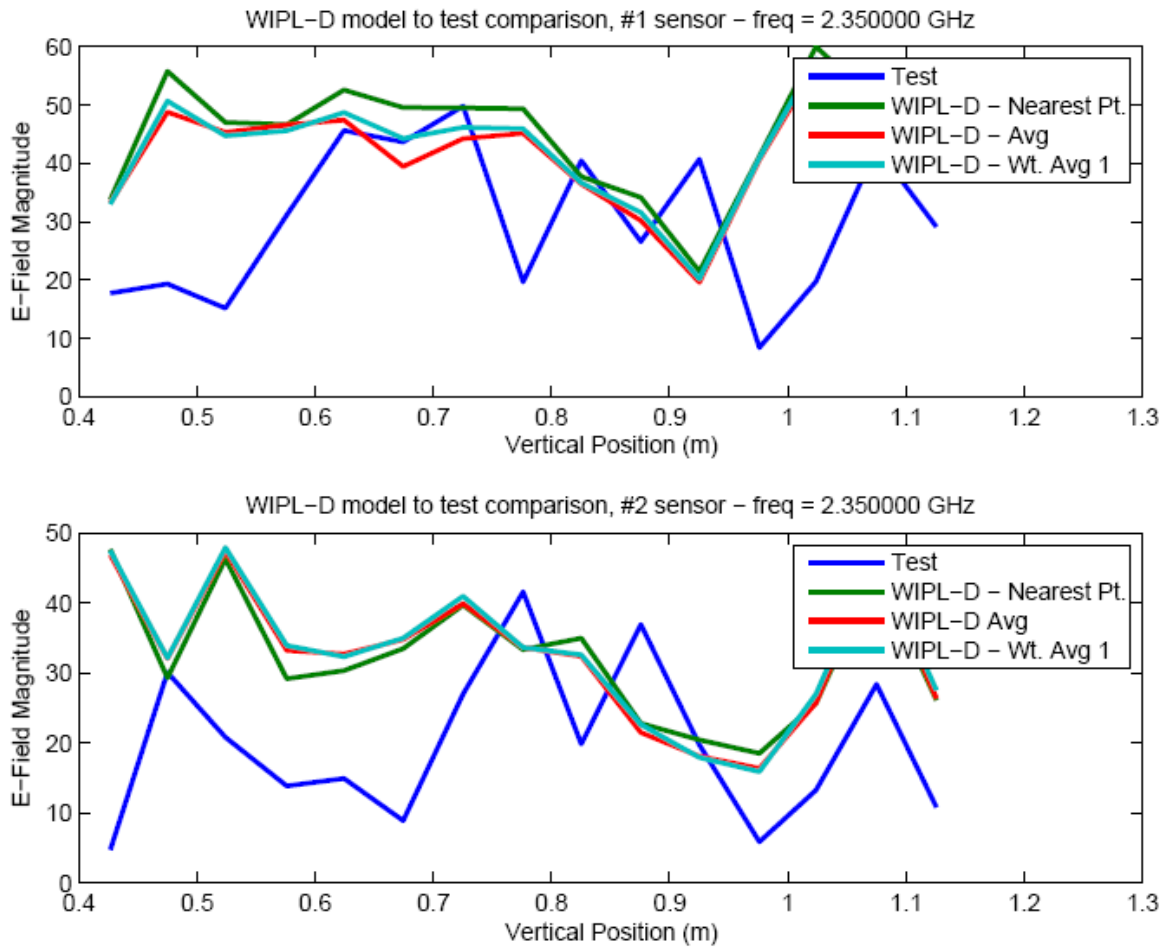
Figure 58. Comparison of the magnitude of 3 axis E-field for composite three layer model without the fiberglass mount.

It is interesting to note as shown in Figure 59 and Figure 60 that the E-fields for the three layer and single layer models were nearly identical for S-band, when substituted in the distributed impedance model. However, for C-band, where the skin depth is much shorter, the 3 layer calculations did not give the same results as the one layer as seen in Figure 61 and Figure 62. In this case the thinner sample, closer to the skin depth gave more reasonable results. This is

consistent with other studies of thin material where dominant parameters affecting the surface impedance vary with the skin depth as discussed in Section 1.2 [49]. When skin depth is smaller than depth of material, then it is better to use a sample size in the equation that represents that depth. If skin depth is larger than sample size, then the full sample can be used as with the layered case in 4.3.2.2.
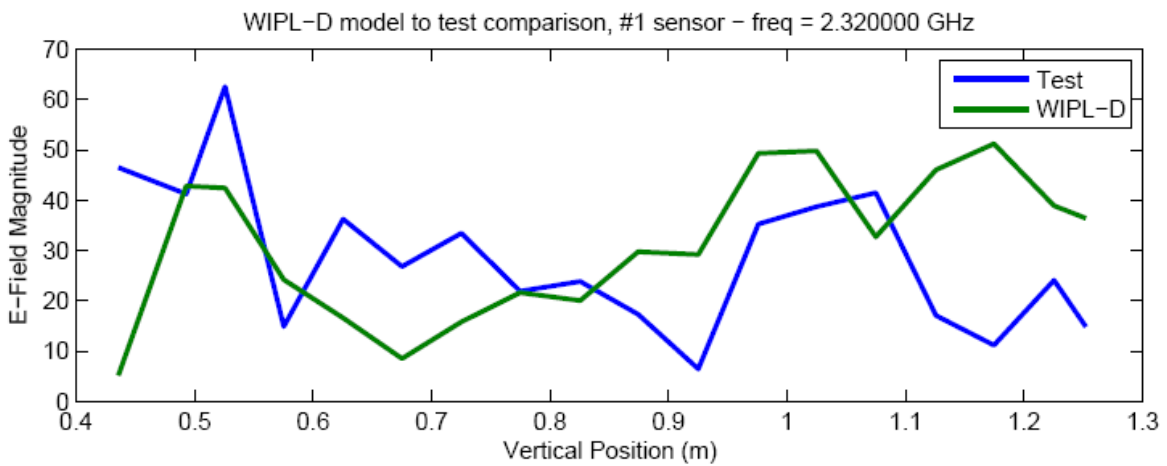
Figure 59. Composite fairing E-Field (z – component): S-Band single layer
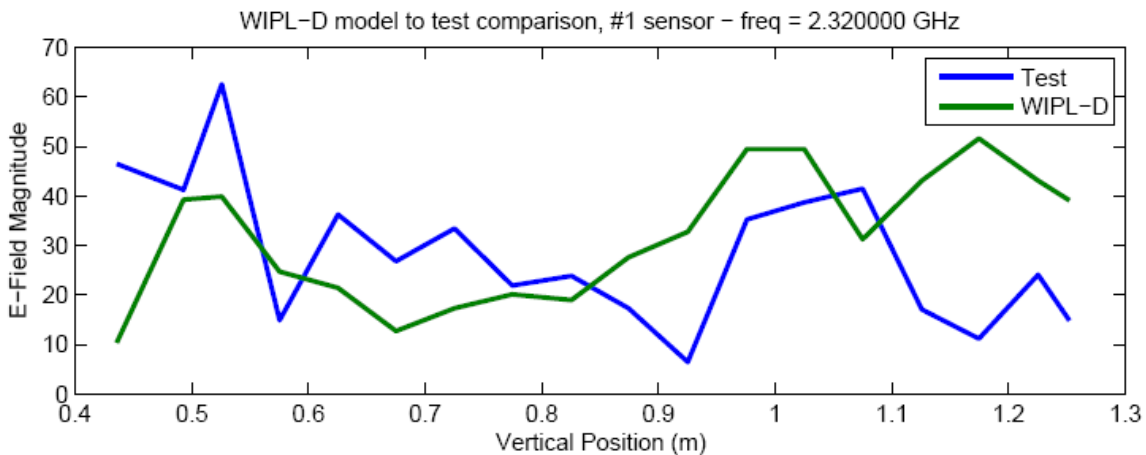
Figure 60. Composite fairing E-Field (z – component): S-Band three layer.
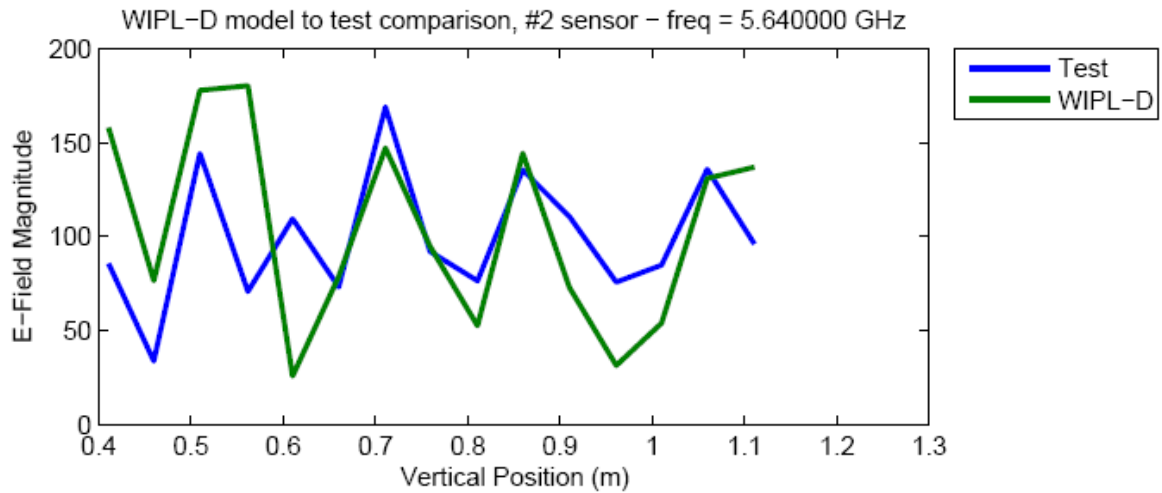
Figure 61. Composite fairing E-Field (z – component): C-Band single layer
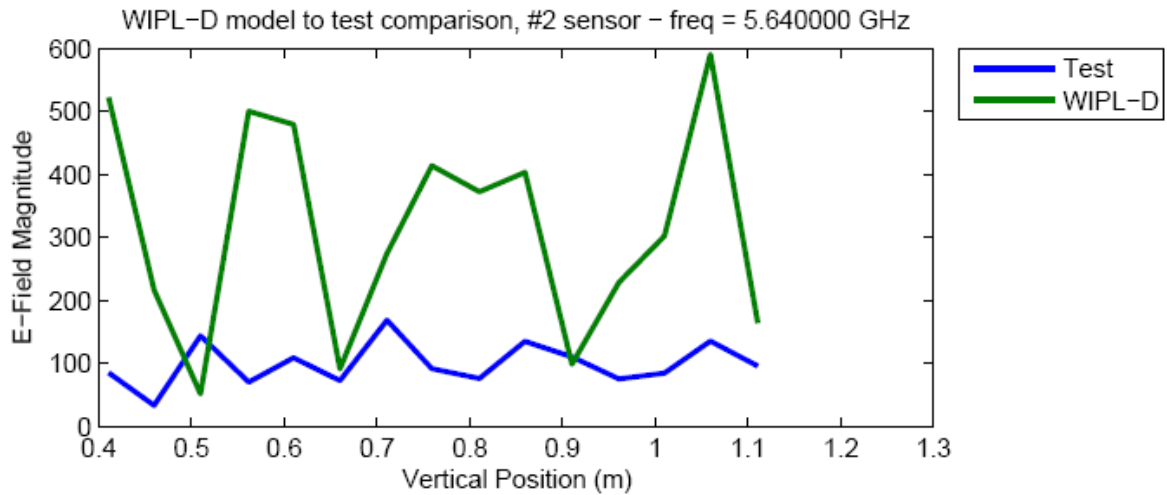
Figure 62. Composite fairing E-Field (z – component): C-Band three layer

A sample of outer probe data for 2.35 GHz, single layer, single axis is shown in Figure 63. Figure 64 shows the same configuration for the inner probes. The single composite layer,

single z component data is shown for C-band at 5.61 GHz in Figure 65. These are a sample of the entire data set from 2.3 to 2.5 GHz and from 5.6 to 5.7 GHz at 10 MHz increments. The entire data set is considered with a frequency stirring technique discussed later in this chapter.
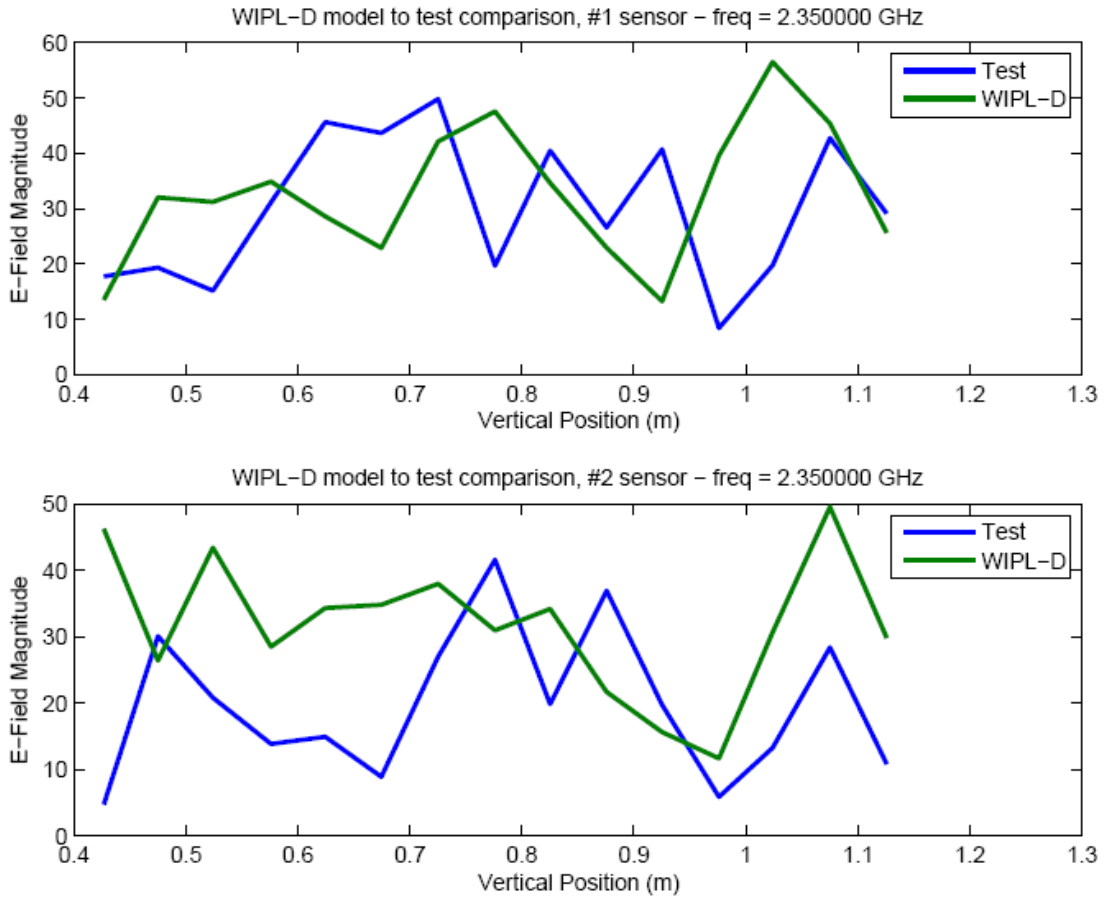
Figure 63. Outer probes vertical component E-field data (no mount).
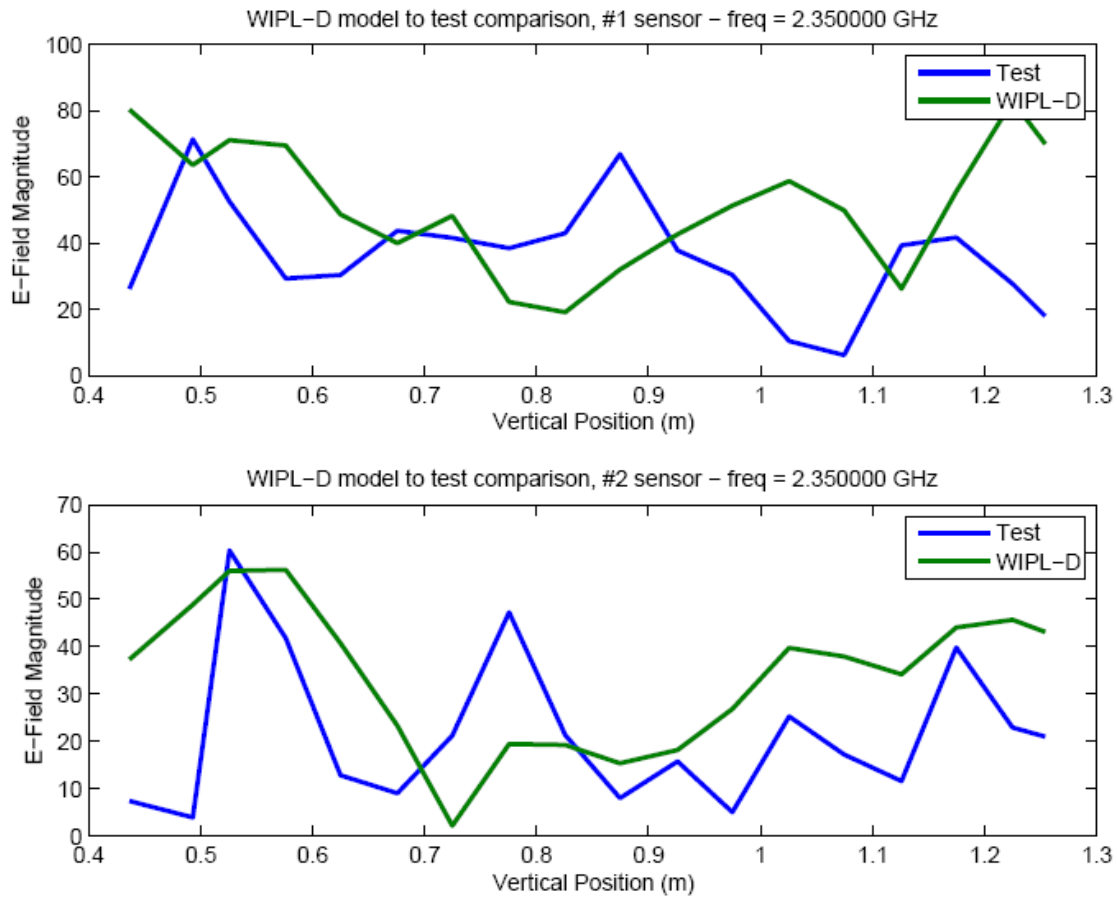
Figure 64.   Inner probes vertical component E-field data (no mount).
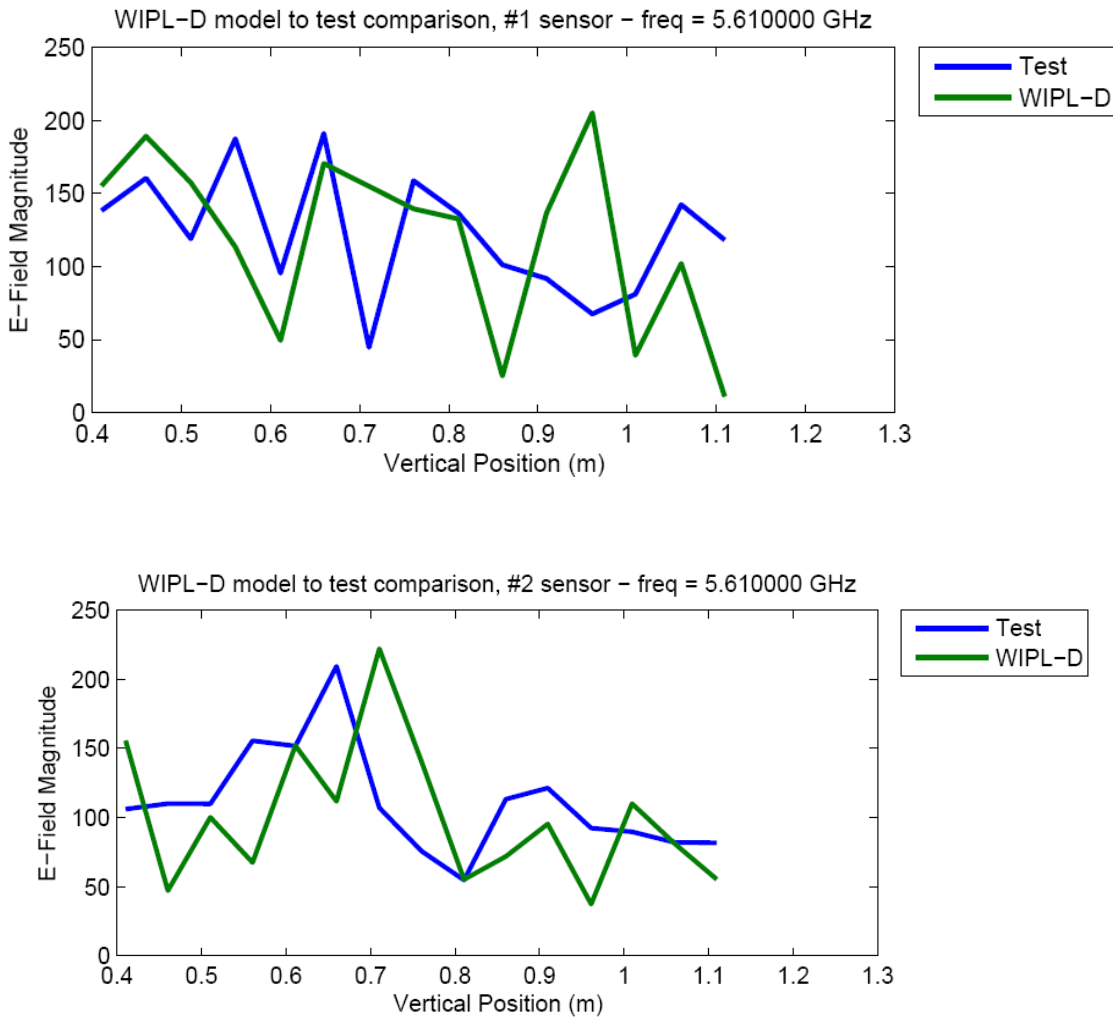
Figure 65. C-Band single layer (outer probes) verticle component.

5.3.5   Comparison of Statistical Model for Fairing Field Determination

The test and model data have relatively the same magnitude, but peaks are often offset in position. This is due to features that are not easily modeled such as the complex shape of the fiberglass mount that changes the horizontal bar location for each position. One of the goals of this research is to provide a method to predict fields in the fairing of very complex structures. For most analysis, an exact replication of the flight condition is not possible or even known.

Hence, a comparison method is desired to show expectations over a range of frequencies and conditions. Statistical methods are a suitable way to accomplish this and are examined here. The selected distributions to be used for comparison are based on those used for reverberation chamber testing, which have shown that reverberation chamber test data correlates well with statistical distributions as described in Section 2.5. However, since the paddle wheel stirring method used in reverberation chambers is often not realistic for a launch vehicle fairing and walking around in the fairing is not feasible, a modified "random walk" procedure was applied to computational and test results [97]. The data was examined in two ways. First, the individual axis readings of the four probe locations and 15 vertical locations were used. To obtain a data-based mean-normalized cumulative distribution function (CDF), each data point was divided by the mean and sorted by amplitude. A comparison is made to the simulated distribution obtained in Section 2.5 using the Chi distribution two degrees of freedom (DoF), which is the distribution for a single axis electric field measurement. For certain low-loss cases the Weibull distribution is used for the comparison. Next, this position data is combined with the data at frequencies 10 MHz apart to represent frequency stirring. The 10 MHz step is often used in industry for such frequency stirring comparisons. In general, the addition of the frequency based samples improves alignment with the simulated statistical field distribution.

The distribution comparisons for one frequency and multiple positions are shown in Figure 66 for test and Figure 67 for the model. These CDF's weakly approximate the theoretical Chi distribution with two degrees of freedom. The model and test cases with frequency stirring are shown in Figure 68 and Figure 69. Similar data is shown for C-Band, a single frequency at multiple positions in Figure 70 and Figure 71. The frequency stirred cases for test and model at the C-Band are shown in Figure 72 and Figure 73. The model data follows the Chi two degree of

freedom CDFs, similar to the test data, an important result for modeling purposes. When results over a series of positions and/or frequencies are considered the model is effective at simulating test results. Hence, the application of this NRW technique is effective with limitations described here. Models are an effective way to capture the predicted peaks over a frequency band, but it is not recommended to model only at the frequency of interest.
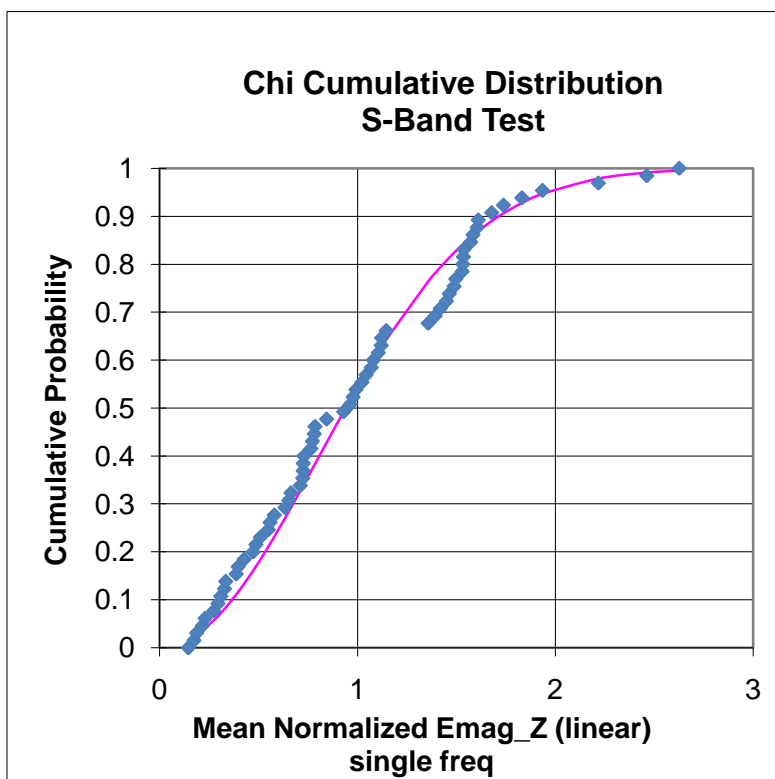
Figure 66. S-Band composite fairing position stirring test data following Chi distribution.
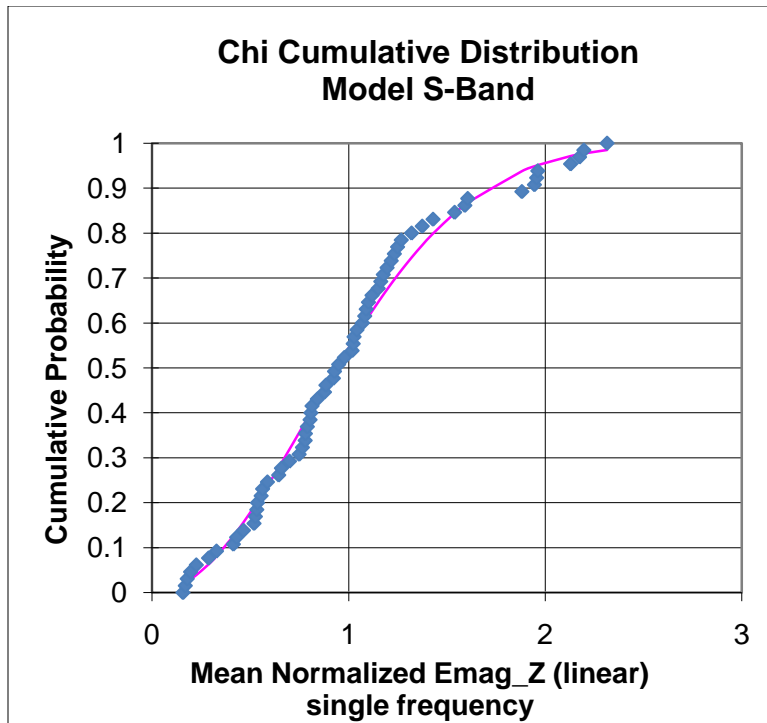
Figure 67. S-Band composite fairing position stirring model data following Chi distribution.
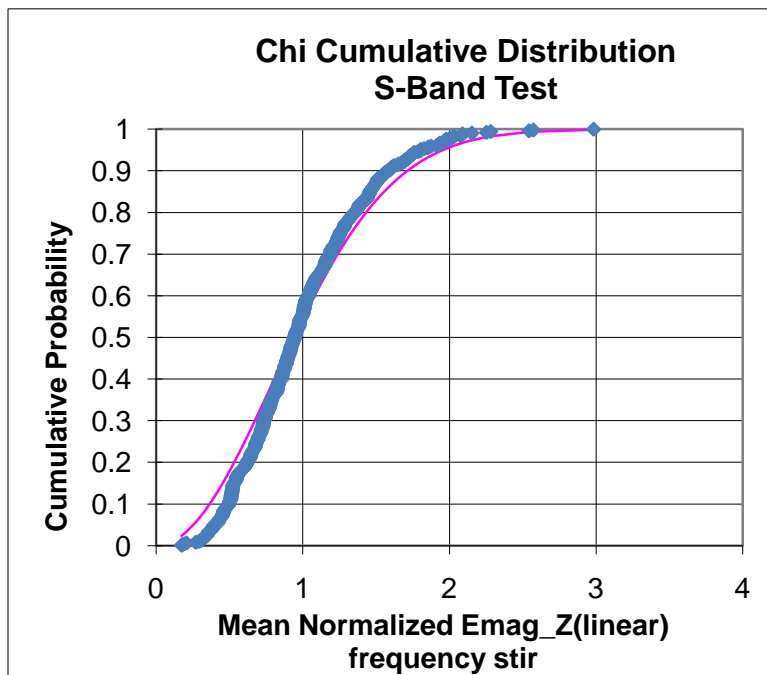
Figure 68. S-Band composite fairing position and frequency stirring test data following Chi distribution.

133
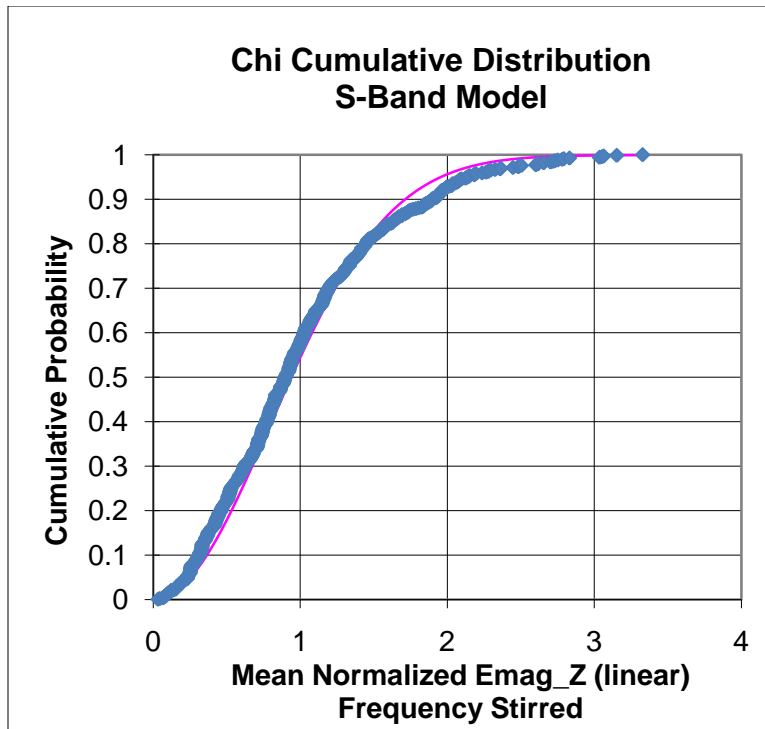
Figure 69. S-Band composite fairing position and frequency stirring model data following Chi distribution.
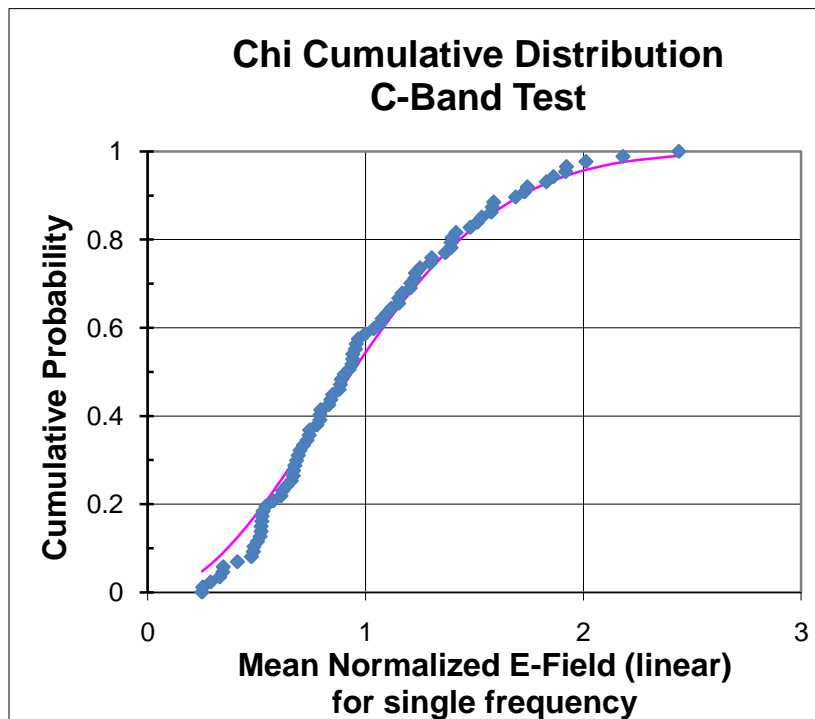
Figure 70. C-Band composite fairing position stirring test data following Chi distribution.
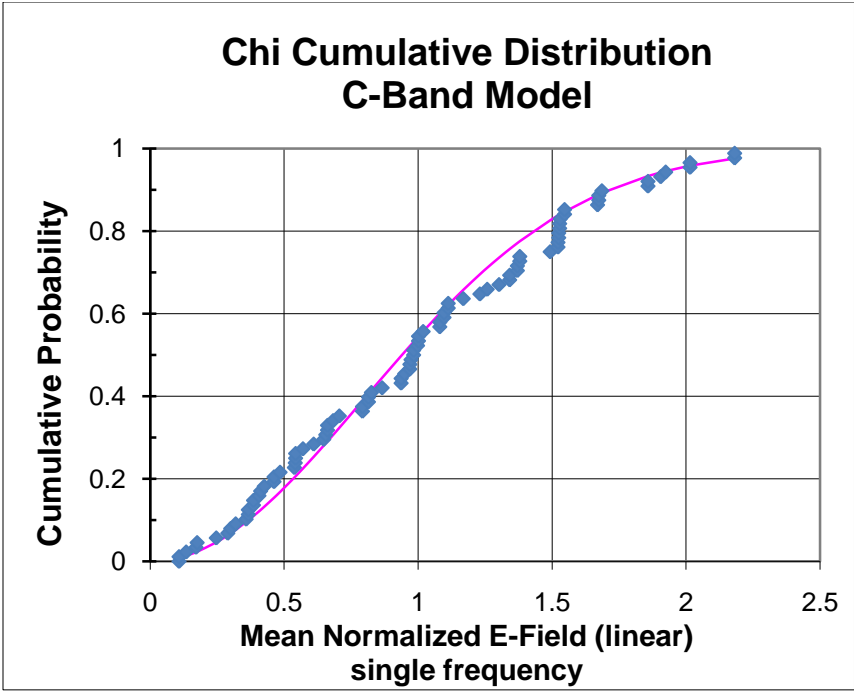
Figure 71. C-Band composite fairing position stirring model data following Chi distribution.
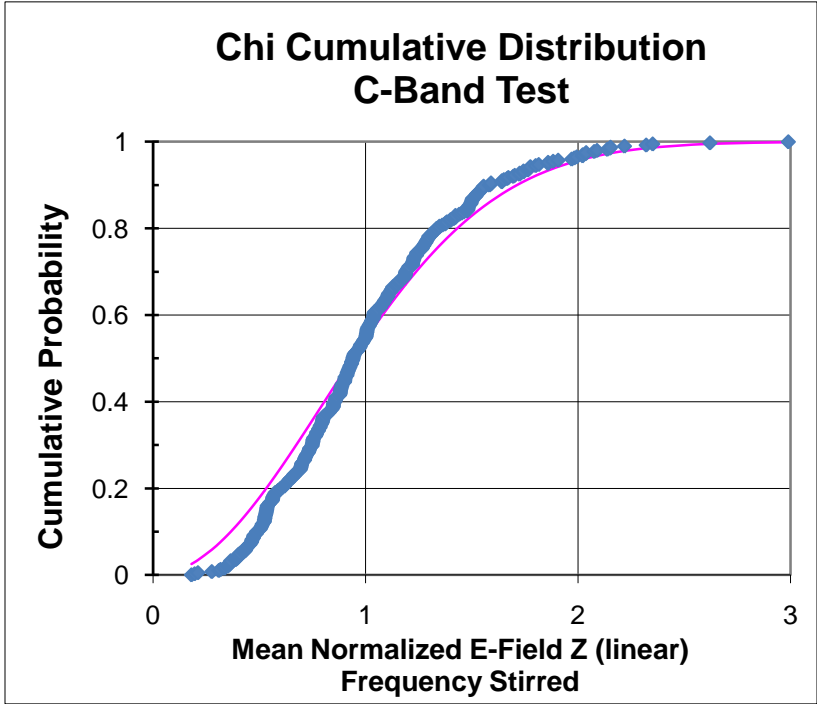
Figure 72. C-Band composite fairing position and frequency stirring test data following Chi distribution.

Chi Cumulative Distribution
C-Band Model
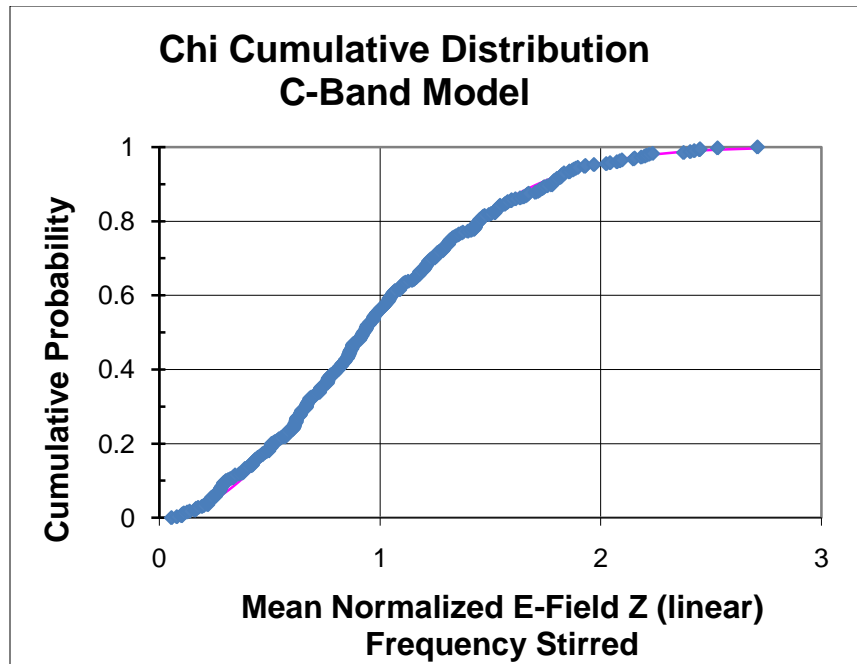
Figure 73. C-Band composite fairing position and frequency stirring model data following Chi distribution.

5.3.6 Lossless (Simulation Only) Distribution Comparison at S-Band

In reverberation chambers undermoded conditions can occur in highly reflective chambers in the lower frequency range of the chamber as described in Section 2.5. To examine the limits of the Chi distribution in undermoded conditions that can occur in launch vehicle fairings, a simulation only lossless structure is evaluated by applying PEC properties to the CAD model walls. Albeit the peak Q is limited somewhat by the discretization process in MoM, the PEC structure is selected because the theoretically infinite Q will lead to an undermoded condition where less energy spreading leads to dominant eigenmodes. Volumetric changes, such as the addition of loads addressed in the next section, can also affect the cavity modes. The size of this CAD structure is electrically large at S-Band, but not large compared to multimoded reverberation chambers where the Chi distribution has been shown to apply. Research suggests

that Weibull distributions can be applied in the undermoded case. It can be seen in Figure 74 and Figure 75 that the simulated PEC data follows the Weibull distribution more closely than the Chi distribution. This change in distribution for the undermoded case is an important bound and its applicability is considered further in the following section.
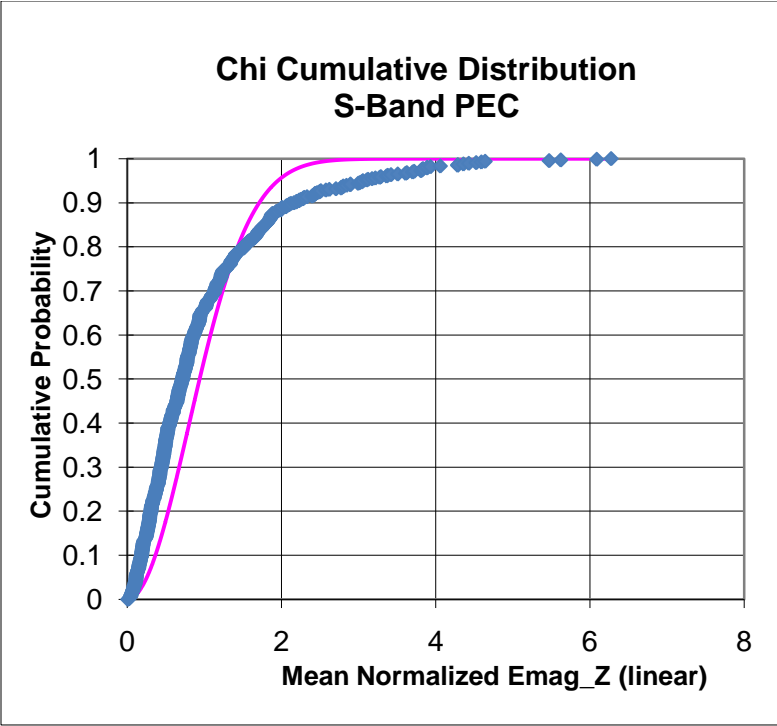
Figure 74. Chi distribution with two degrees of freedom (DoF) with modeled PEC data.
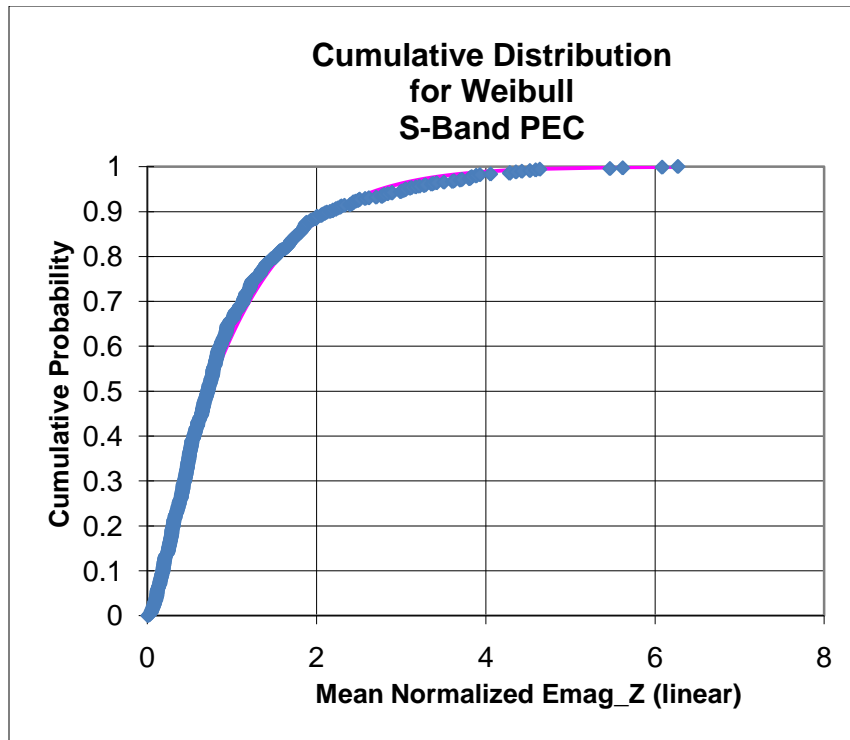
Figure 75.   Weibull distribution with two degrees of freedom (DoF) with modeled PEC data.

5.3.7   Rotational Models

In order to extend the results of this work to electrically larger structures, further examinations of statistical distributions were made for the rotationally symmetric case to examine the effects of larger fairings and the loaded fairing on the distribution.   The use of rotational symmetry greatly extends the computational ability of the tool.   The fairing shown here uses only 15 degrees of the full fairing with a height of 3 meters and a diameter of 1 meter. The excitation is one volt in the C-band.   Note that for this model the excitation must also be rotationally symmetric, which in this case is a dipole.   It can be seen that although the same distribution is achieved for a centrally located emitter in a typical fairing in Figure 76, the loaded fairing distorts the distribution as shown in Figure 77.   The variance from the mean is much

greater in the loaded case. The Weibull distribution shows good agreement with the loaded case distribution as shown in Figure 78 which indicates an undermoded cavity for the loaded case. This makes sense as the proximity of the load to the fairing walls prevents some modes from developing
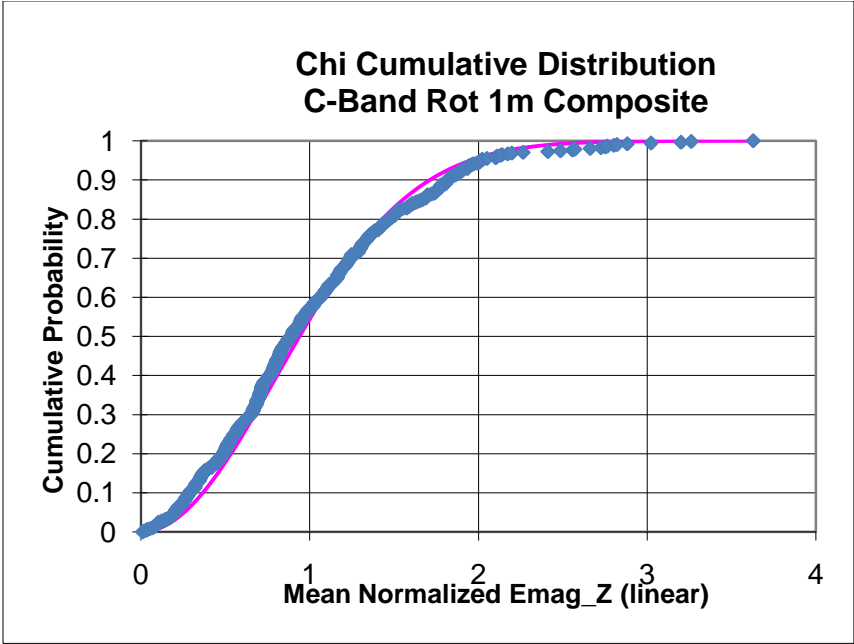
Figure 76. CDF of rotationally symmetric 1 meter model composite fairing with C-Band excitation.
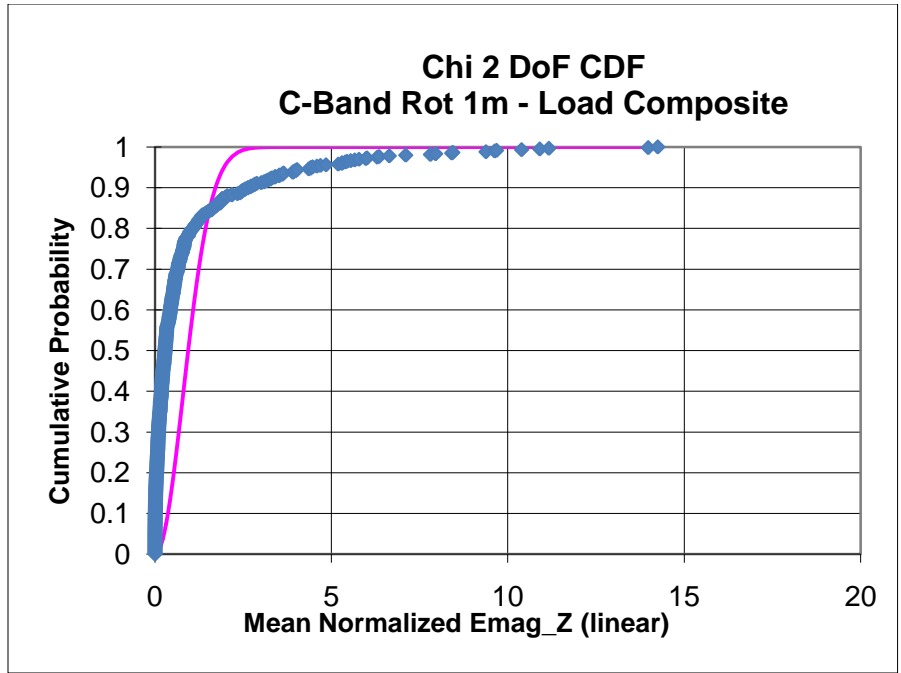
Figure 77. CDF of rotationally symmetric 1 meter model composite fairing with C-Band excitation and spacecraft load.
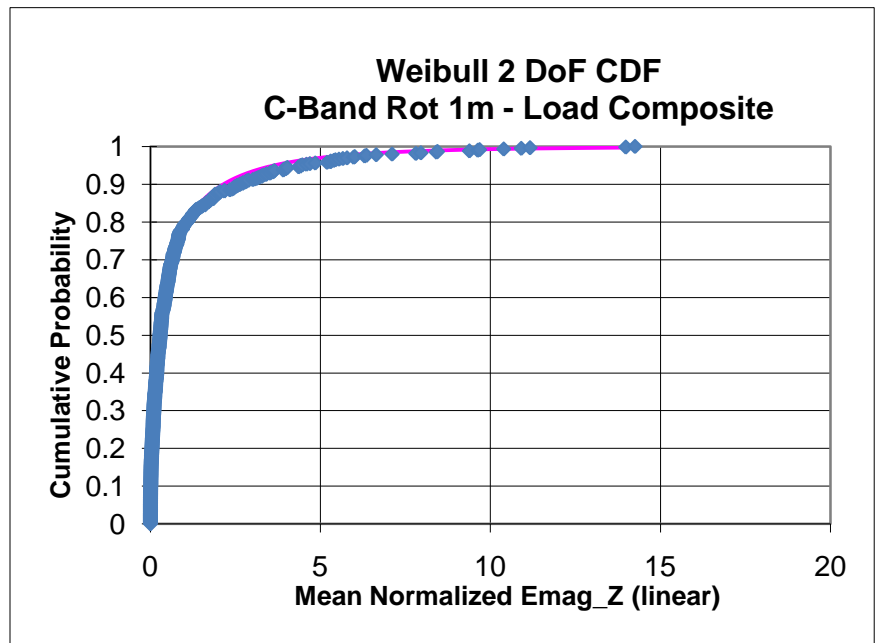
Figure 78. Weibull distribution comparison of loaded composite fairing with rotational symmetry.

The fields within the fairing were then examined for the loaded case. It is desired to see if the empty fairing case provides a magnitude bound for the loaded fairing as was the case when the receive power was only measured in one location in Section 4.3.2.1.3. For this rotationally symmetric case, the bound was applicable for most frequencies and locations except where additional resonances were set up between the load and the fairing wall and at the top of the load. Thus, for general cavity fields away from the load, the loaded case is reasonably enveloped by the unloaded case as shown in Figure 79. At locations were the load is close to the fairing wall, the loaded case is also generally higher, but occasional modes are developed between the fairing wall and the load that cause higher fields as shown in Figure 80. In some cases resonances are blocked from forming between the fairing and load walls resulting in lower fields than the unloaded case at the same frequency. Similar work has shown this mode blockage and the bounding effect of the empty cavity for the loaded case [96], [123]. At places very close to the load boundary, significantly higher fields can develop in the loaded case as shown in Figure 81. Hence detailed modeling is needed to examine resonances at wall boundaries.
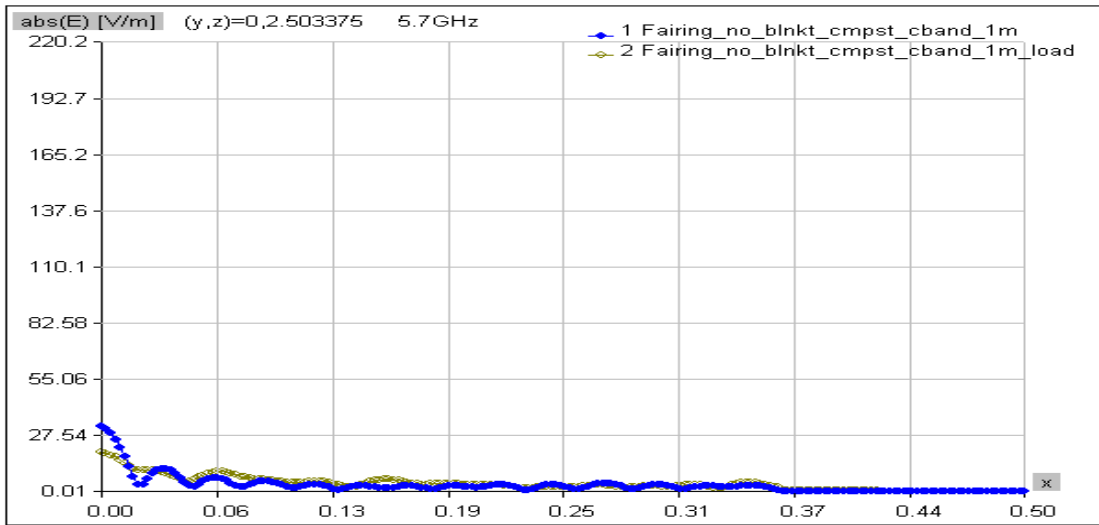
Figure 79. Loaded and Unloaded composite fairing fields along x axis at the top of the fairing (2.5 meters) at 5.7 Ghz.
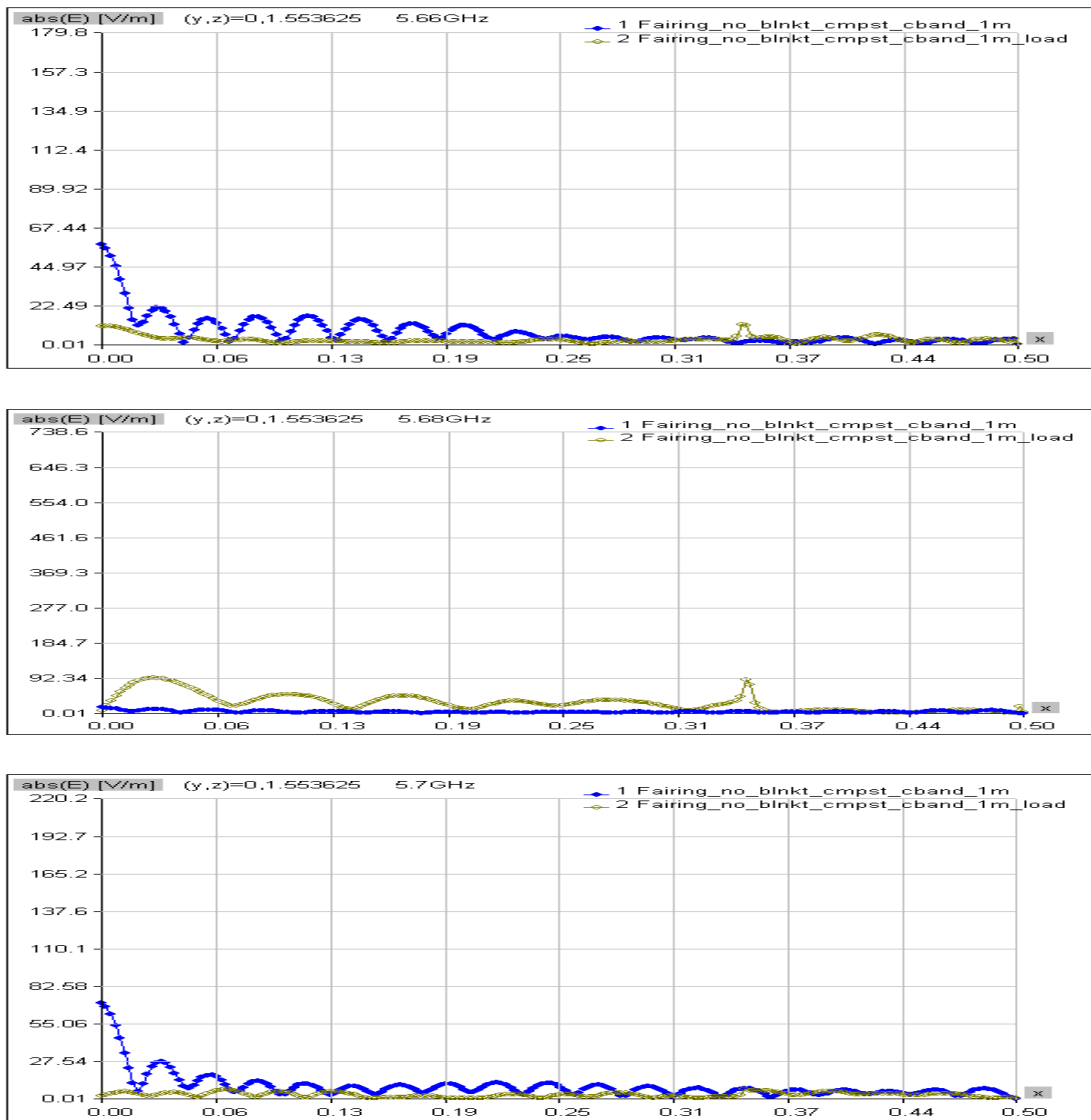
Figure 80. Loaded and unloaded composite fairing fields along x axis at the side of the fairing (1.55 meters) at 5.66, 5.68 and 5.7 GHz.
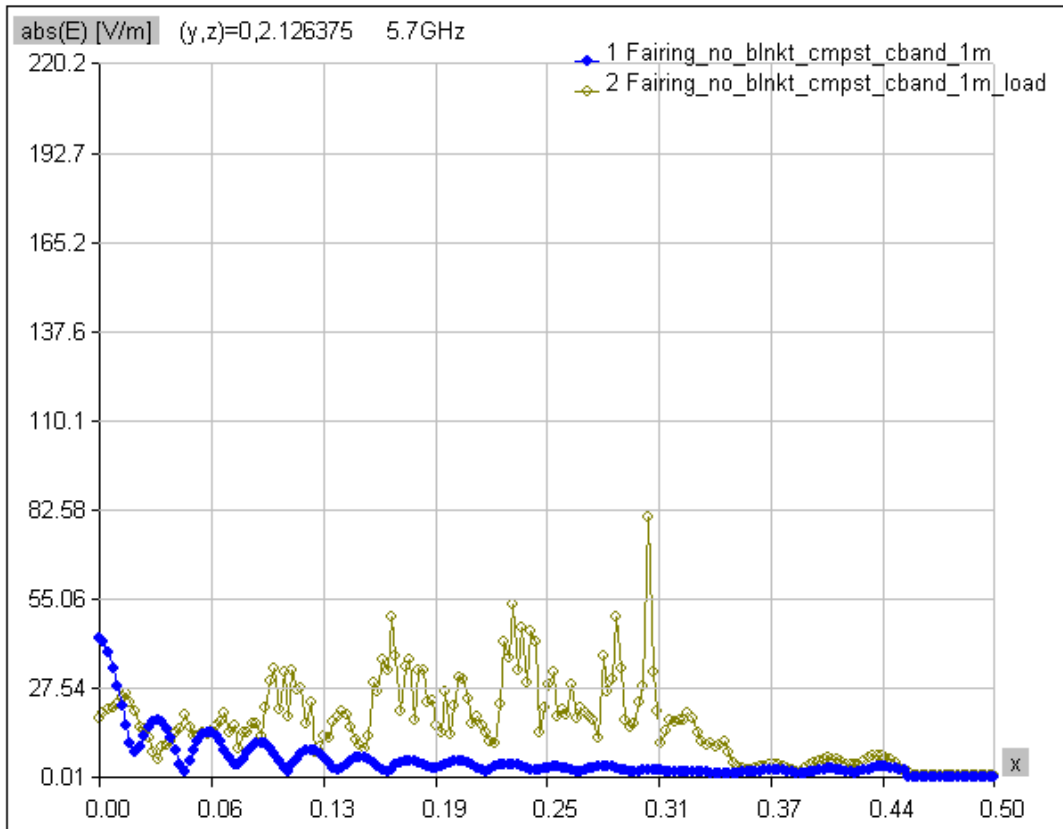
Figure 81. Loaded and Unloaded composite fairing fields along x axis at the PEC load interface (2.1 meters) at 5.7 GHz.

It should be noted that the inner model was assumed to be a closed PEC surface. There should be no penetration of fields in the fairing. However, due to the EFIE issue described in the methodology section, fields do penetrate the fairing as it is essentially a Faraday cage. Techniques to reduce these effects were examined such as improving the integral accuracy, decreasing the mesh size, and increasing the order of the expansion manually as described in Section 2.1. The most effective technique was to fill the inner cavity of the load with a dielectric of air properties which forces the PMCHW equation and provides a combined EFIE/MFIE solution. This is shown in Figure 82. A comparison plot of the x axis data is shown in Figure 83 at z = 1.5 meters, which indicates that the normal 2λ patch mesh size leads to discontinuities at

144

the inner PEC cylinder. There are no discontinuity errors in the fairing fields when the patch size is changed to 0.5λ, however, using the original 2λ patch mesh size and adding a dielectric cylinder with a permittivity of 1 –j1 inside of the original cylinder as shown in Figure 82 gives the expected zero field inside a PEC cylinder, which is essentially a Faraday cage. The choice of the dielectric is not important in this case as the interest is in the fields in the fairing cavity, not in the inner cylinder. For shielding effectiveness problems as discussed in following chapter, the only valid choice for the dielectric is air. It is interesting to note in Figure 83 that either the 0.5λ solution or the 2λ solution with the dielectric inner cylinder give consistent results in the fairing outside of the inner cylinder, even though results inside the inner cylinder are different. This difference becomes an issue for shielding effectiveness studies discussed in the next chapter. The inner dielectric cylinder filling does not need to be the same size as the PEC cylinder to provide an accurate solution.
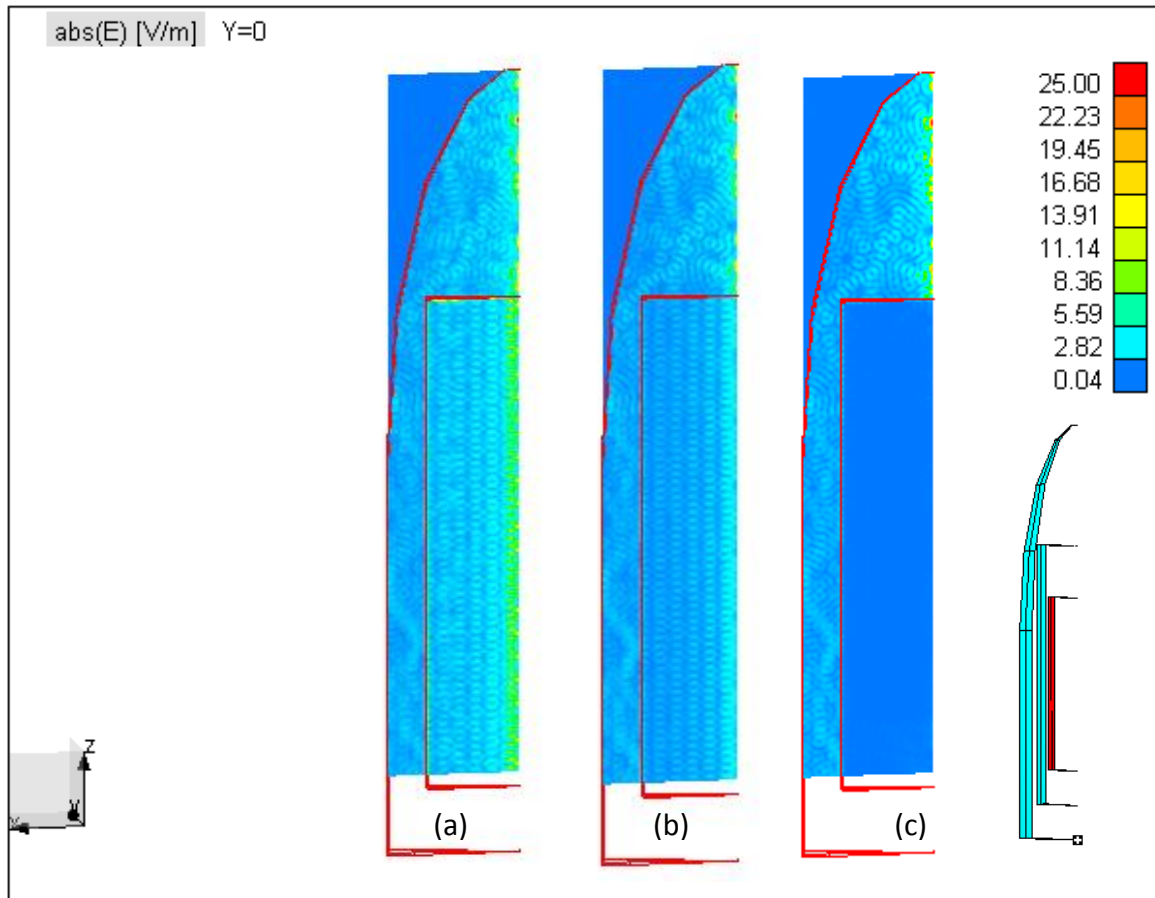
Figure 82. Rotationally symmetric 1 meter diameter composite fairing with PEC load (a) 2λ patch mesh size, (b) 0.5λ patch mesh size, (c) 2λ patch mesh size with inner dielectric shown in inset.
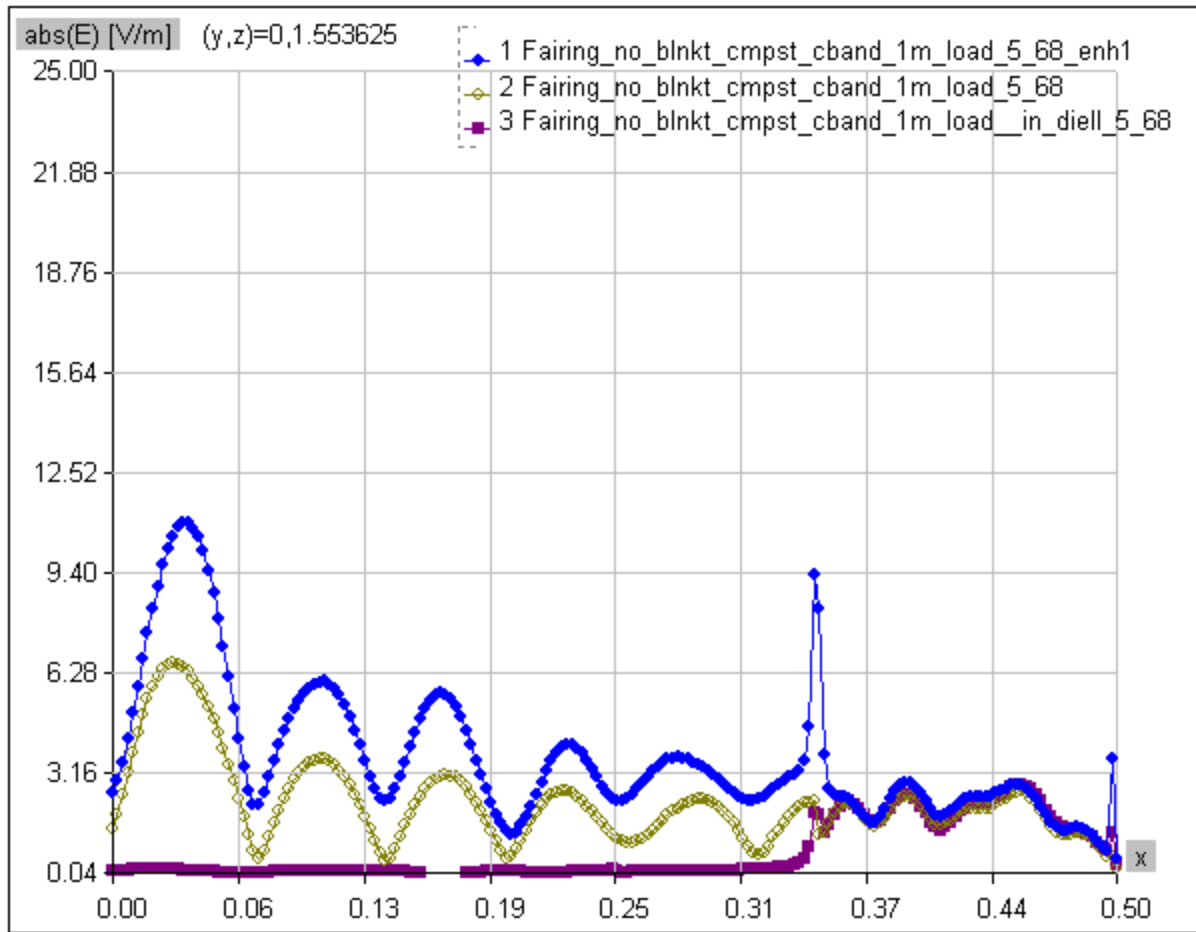
Figure 83. X Direction change for 2λ patch, 0.5λ patch, and 2λ patch with inner air dielectric. cylinder.

5.3.8   Acoustic Blanket Models

The affects of acoustic blanketing with RF absorbing properties were also examined in this chapter for the composite fairing model fixture.   The MLFMM model was used for this application because multiple layers are easily implementable in the FEKO tool and the RF absorption of the blanketing material is adequate to achieve convergence.   Figure 84 shows that fields in fairing are sharply reduced by the addition of an absorbing RF blanket.   Blankets available in the industry were examined.   As anticipated those impedances closest to the

147

impedance of free space provided the most absorption. The 10 kOhm blankets (Figure 85) and

those less than 3 ohms offered little attenuation for the composite fairing.
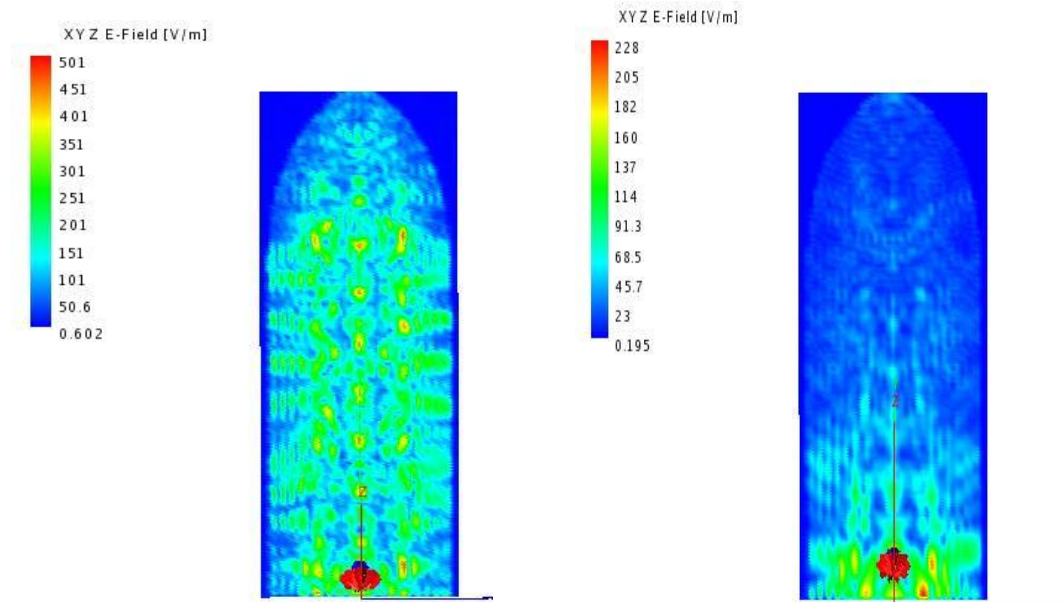
Figure 84. Composite without a blanket (left) and fully blanket 300 ohms (right) at 5.65 GHz.

Placement of absorbing blanketing sections was also examined and shown in Figure 85 and

seen to have an impact on the field distribution. Significant reduction was achieved by placing

the absorbing blankets over a small portion of the walls near the emitter.
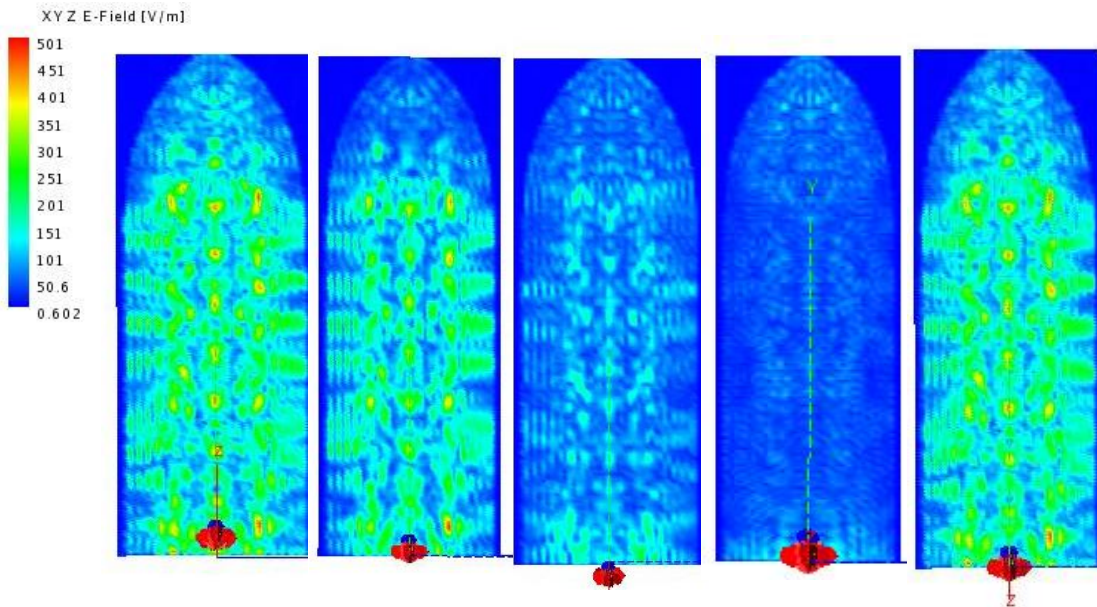
Figure 85. Blanket Configurations - Empty, top only, side only (0.25 m) $\lambda/2$ and $\lambda/4$ spacing from wall, 10 kΩ blankets.

In this case the emitter is a dipole such that the initial pattern is spread radially from the device. It can be seen that the full blanket attenuation can be almost achieved by using side blankets only. Even using a very short side blanket close to the transmitter significantly reduced the cavity overall fields. Further reduction in the field levels is achieved by changing the distance of the blanket to the wall from one inch to one half an inch (approximately $\lambda/2$ and $\lambda/4$ spacing from the wall), accounting for the shorted transmission line effect. Top blankets in this case have minimal effect except for fields close to the top of the fairing.

Careful placement of blankets to absorb fields at their first incidence can accordingly provide an economical method to reduce cavity fields. Blanket impedances of 3, 300, and 10k ohms were chosen in this evaluation due to availability of commercial products [124][125]. Maximal attenuation will be achieved with blanket surface impedances that are close to the free space impedance. Other factors are important, however, when choosing materials for space

149

applications such as their thermal and contamination properties. Materials that are thermal insulators are typically needed and materials with ideal surface resistance for RF absorption are typically thermal conductors as well. Hence, the size of the blankets as shown here can be reduced and optimized with CEM models to meet RF and thermal constraints. In addition, mixing of the fields reduces the peak levels in most of the fairing as shown with the spacecraft loads in the previous section.

5.4   <u>Summary</u>

In this chapter the electromagnetic fields in a composite fairing were examined. First, the NRW technique was applied to the composite walls in both MLFMM and higher order MoM models. The field comparison with the test model showed that peaks over a frequency range or a position range compared well. The statistical Chi distribution with two degrees of freedom was applied to show that the test and model CDFs match this theoretical distribution. This validates the results from the simulation models which can hence be used as long as multiple frequencies or points within the fairing are considered. In addition, the loaded case was considered, which did not follow the same distribution, but rather an undermoded distribution. Effective ways to model inner cavity structures such as spacecraft were presented, and the effects of blanketing on the cavity fields was studied.

CHAPTER 6. SHIELDING EFFECTIVENESS: FAIRING WITH APERTURES - EXTERNAL SOURCE

6.1 <u>Introduction</u>

Evaluating the degree to which an enclosure attenuates external electric fields is referred to as shielding effectiveness. This topic has been widely studied in industry and there are numerable handbook type formulas to predict attenuation of materials and apertures that comprise enclosures. Electromagnetic interference testing is performed in enclosures that routinely achieve 100 dB of shielding effectiveness to meet FCC requirements by implementing well-known industry techniques of applying gaskets and finger-stock around doors, honeycomb and screen in apertures, and highly conductive metals such as copper for the bulk exterior [5], [126]. In recent years, CEM simulations have shown the need to evaluate eigenmodes within these enclosures and add adequate absorption for a repeatable test results. In the case of launch vehicle fairings, performing full-up systems test to evaluate shielding effectiveness is costly and not routinely performed.

Consequently, the focus of this study is not on introducing new shielding effectiveness techniques, but in evaluating the ability to determine this using 3D computational tools. A test fairing with apertures was manufactured and shielding effectiveness tests were conducted. Next, honeycomb fixtures were then installed in the apertures as a means of introducing attenuation. Both of these cases are modeled with 3D CEM simulation. Benefits and limitations of such modeling are discussed as well as techniques to alleviate the limitations. In addition, frequency scaling of a small-scale fixture is used to evaluate shielding impacts to large vehicles.

6.2   Fairing with Apertures_ - Test Results

6.2.1   Fairing Fixture

A sub-scale test fairing representative of a typical launch vehicle fairing was fabricated in order to anchor the use of 3D CEM modeling to evaluate fairing shielding effectiveness. The actual vehicle design was not duplicated due to proprietary reasons. This prototype fairing was developed to sufficiently anchor the computational model in a laboratory implementable setting. Frequency scaling was employed to make the smaller prototype vehicle size applicable to the full scale vehicle. As cavity resonances are proportionate to the transmitted wavelength with respect to the cavity dimensions, the transmitter frequency was increased by the same ratio that the geometry was decreased. The prototype was 6.5 times smaller than the full 4 meter fairing. The full scale frequency of interest was 2.0 to 2.3 GHz as most spacecraft transmit and receive in that range. Accordingly, the transmit frequency of interest is 13 - 15 GHz.   Apertures on the fairing were representative of those on the full-scale vehicle, but scaled to a smaller size to correspond to the higher transmit frequency. Scaling the frequency to model a smaller physical structure is a commonly used technique in the launch vehicle and other industries. Although conductivity of the fixture is not easily scaled, the losses in both the scaled and non-scaled frequency case are ignored and perfect conductivity is assumed. Such scaling is not necessarily feasible for absorbing layered material as conductivity can change significantly over the scaled frequency range.

6.2.2   Test Procedure

A test program of the prototype fairing was developed in order to anchor the computational model. The sub-scale testing effort was initiated to understand the effects of apertures in a representative cavity structure. IEEE-299, IEEE Standard Method for Measuring

the Effectiveness of Electromagnetic Shielding Enclosures, was utilized as the test methodology for characterizing the sub-scale test fairing as shown in Figure 86 [127]. The tests were performed on multiple aperture configurations with the transmitting antenna outside and receiving antenna inside the test article. First, the sub-scale fairing was baselined with open apertures. Second, the sub-scale article was completely closed with conductive tape. These two tests created the bounding cases. Once these boundaries were established, honeycomb inserts were added on the aperture (also shown in Figure 86) to examine the effects of the RF hardening.

Figure 86. Test set-up and fixture showing the honeycomb inserts for RF hardening.

Shielding effectiveness with the honeycomb in place is shown with the moving average values in Figure 87. This shielding effectiveness data is the comparison of the received signal in the chamber without the fairing present and the received signal with the fairing present. The outliers or extreme points of peak measurements were also observed for comparison to the desired shielding effectiveness as a limiting case.

For shielding effectiveness considerations, the main concern for launch vehicle fairings is the external emitter threats. These can be most accurately represented by a plane wave at the frequencies of interest. The shielding effectiveness of a structure is continuous and differentiable, but test chamber reflections that are altered by the presence of the fairing can lead to instantaneously higher or lower shielding calculations and a disturbed data reference (Figure 88). The reference measurement should ideally be flat, but show variations, accordingly, a moving average of the test data is used for comparison to model data which is taken only at specific frequencies, with peaks being taken in a spatial reference area.
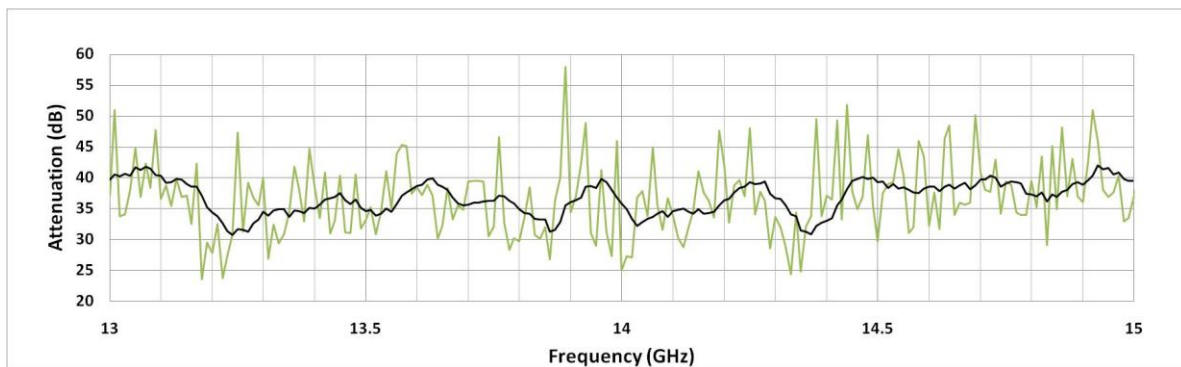
Figure 87. Test moving average (black) versus test individual point (green) shielding effectiveness data with honeycomb inserts.
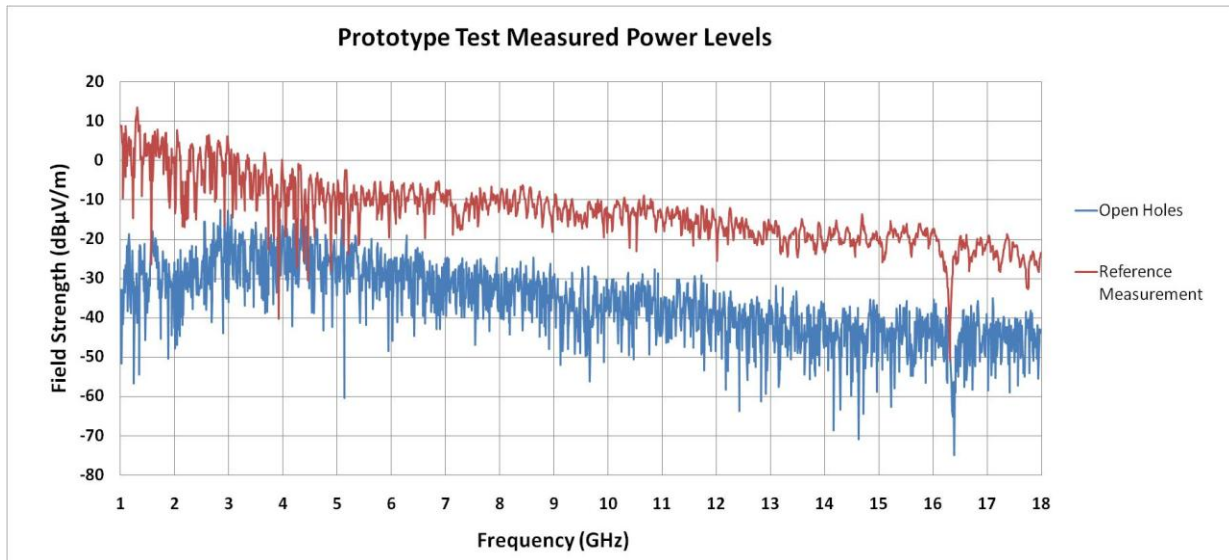
Figure 88. Test power levels with no fairing in chamber (reference case) versus open holes.

Data was collected for the baseline "open-hole" model (no honeycomb in apertures) over the entire test frequency range of 1-18 GHz to look at shielding trends. Additional testing was performed in an open area test site to provide a different test shielding reference. The test variation average is a 3.5 dB between the open-area field test and the anechoic chamber test of the same set-up as shown in Figure 89. This data will later be used as a reasonable bound for model to test comparisons [128].
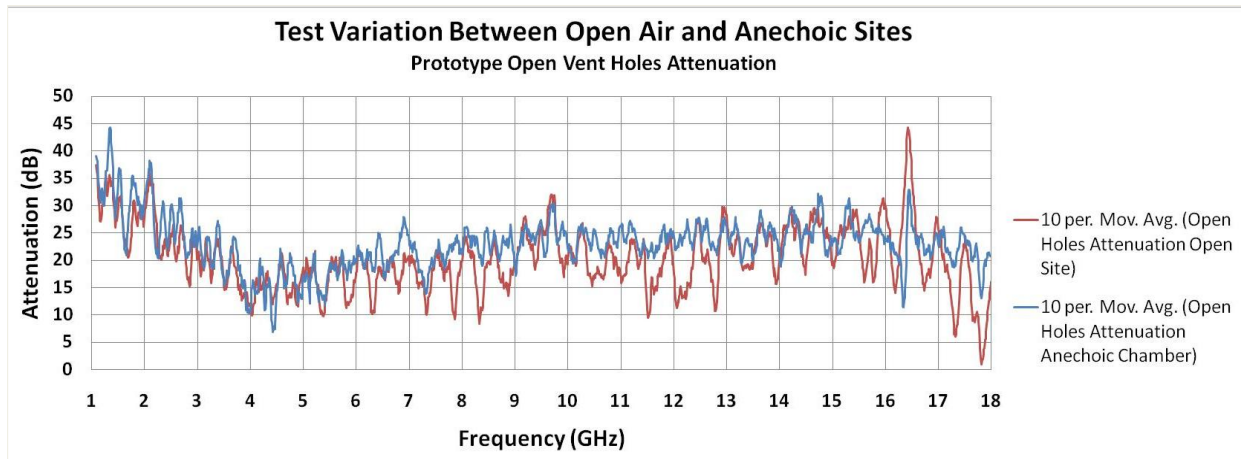
Figure 89. Shielding test data in semi-anechoic versus open area test site.

The summary test data given in Figure 90 shows improvements in shielding effectiveness due to the honeycomb fixture insertion. In some cases, the honeycomb performed within the dynamic shielding effectiveness limits of the test, but in this frequency range, honeycomb did not perform as well as expected. However, overall attenuation of greater than 30 dB is still achieved. Contact of the honeycomb to the fairing walls was maintained, but to prevent altering the fairing walls with each application, no sealant or additional bonding measures were taken at the connecting surfaces, which could have lowered the shielding effectiveness.
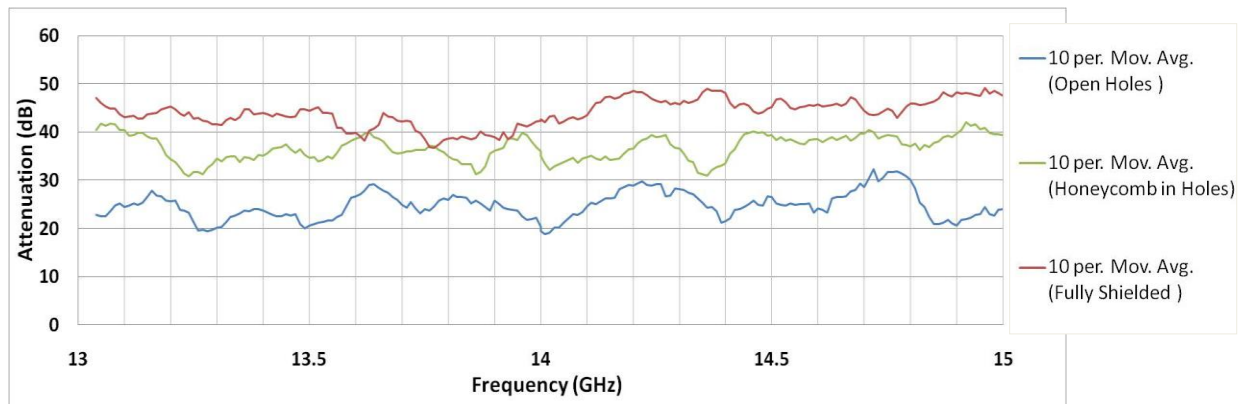
Figure 90. Fairing Test Attenuation Summary.

6.3   Fairing with Apertures - Modeling and Simulation

6.3.1   Baseline Fairing with Apertures Model

First, the simplest test configuration (all vent holes open) is modeled. This case is used for characterizing the model to test uncertainties which were ultimately applied to the more detailed honeycomb vent model.   The mesh requirements of typically one tenth wavelength drive the solver choice to a surface based model that can be solved without entire matrix inversion. The MLFMM method was selected as it maintains the full wave solution with an iterative boxing technique as described in Section 2.2.   The following modeling assumptions were used to keep the model as solveable, yet accurate as possible: surfaces were modeled as perfect electric conductors, plane wave excitation was used, interfacing joints and seams were considered continuous, and small features such as rivets were deleted.   The model with holes as well as the summary of test versus modeled assumptions are shown in Figure 91.

157

Factor	Test	Model	Launch pad
Source	Antenna (approximates plane wave until the far field distance becomes greater (D^2/λ) at the upper frequencies	Plane wave	Plane wave (from external sources)
Reflections	Semi-anechoic has minimal reflections	No external reflective structures modeled.	Launch pad structures will contribute to reflections. No outside reflections during launch

Figure 91. Prototype CAD model with model versus test assumption summary.

Reasonable approximation of the open-hole configuration was achieved with the MLFMM model at the frequency range of interest as seen in Figure 92.
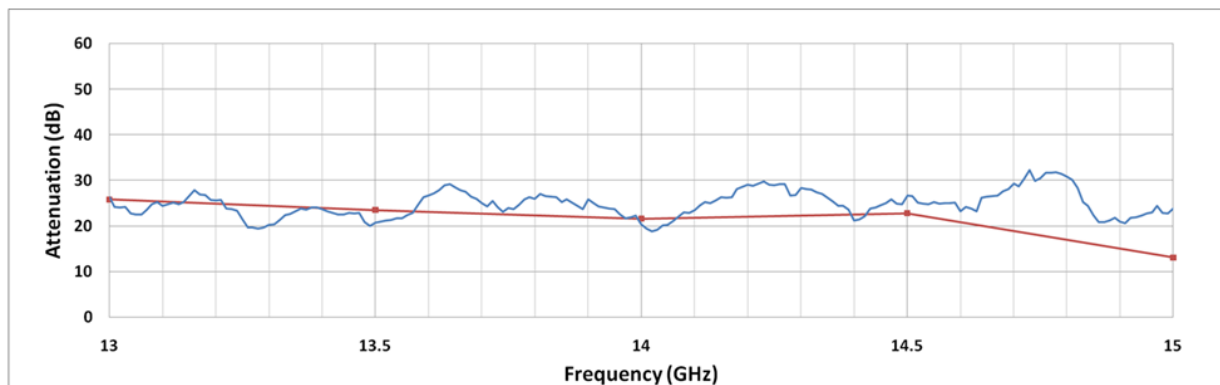
Figure 92: Test To Model Comparison: Open Holes Results - Test Data Moving Average (Blue) to Model Data at Antenna Location (Red).

The baseline model was found to be conservative over the predominate portion of the frequency range. The average variation from the moving average test data was 3.5 dB in the frequency range of interest. The computational residual was less than 2 percent.

Figure 93 shows the open hole to model comparison across the entire tested frequency range and includes a variable z position of the internal electric field. This shows that the model is overall conservative, especially when the fields over a range of points are considered.
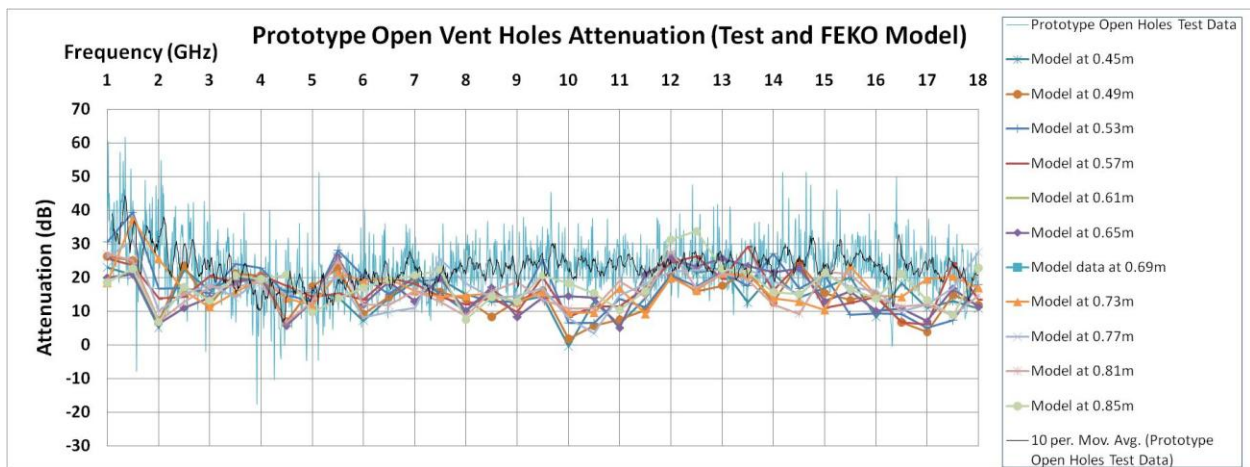
Figure 93. Model to test comparison moving axially up the fairing

In this case the shielding effectiveness data is compared to the model across a wide frequency range using various vertical points as a reference. As the fields can be sampled in the model at fixed intervals instead of just one measurement point, the model offers a wider representation of the field distribution. This data shows that the model is largely conservative compared to the test at least partially due to PEC and plane wave assumptions. Another possible contribution to the model conservatism is numerical excitation. This correlation adds confidence to the use of CEM and to the measurement of a wide range of frequencies to provide overall

159

shielding effectiveness of a narrower range as slight modifications in materials and configuration can shift resonant frequencies.

6.3.2 Alternate approach for Honeycomb Model

A honeycomb model was then developed separately in FEKO and implemented in the vent holes and ECS ports of the FEKO prototype model. The honeycomb was constructed by creating first an individual cell, extruding the planar structure to represent the appropriate honeycomb thickness, copying the cells, and using a cylinder to truncate the honeycomb pattern.

This solution, however, revealed unacceptable results due to excessive residual (see methodology section 2.2). Resonances within a cavity structure with apertures are similar to the resonances in a closed cavity structure and similar numerical residuals occur as in the closed case [69]. For shielding models, the residual error is often more difficult to alleviate because of the desired dynamic range required to simulate shielding of the structures. An alternate approach was thus used to model the effects of the honeycomb structure with a separate model and then apply the attenuation of that model to the source. Although, it was first considered to place the honeycomb in a simpler cube structure to examine the effects independently with the MLFMM method, the resonances of these structures could not be separated to properly evaluate the shielding of the honeycomb.

Another issue with the honeycomb model is the intricacy of the mesh required for this geometrically detailed element decreased the computational efficiency of the model. Singularities were formed at the adjoining edges despite of union and simplifying efforts. To address this issue, a separate honeycomb model was constructed outside the fairing model and the resulting attenuation applied to the model source. The honeycomb model was implemented in an infinite plane so that the Green's planar function could be used. In this technique depth is

allowed and the honeycomb attenuation could be characterized by (20). The honeycomb model is shown in Figure 94.
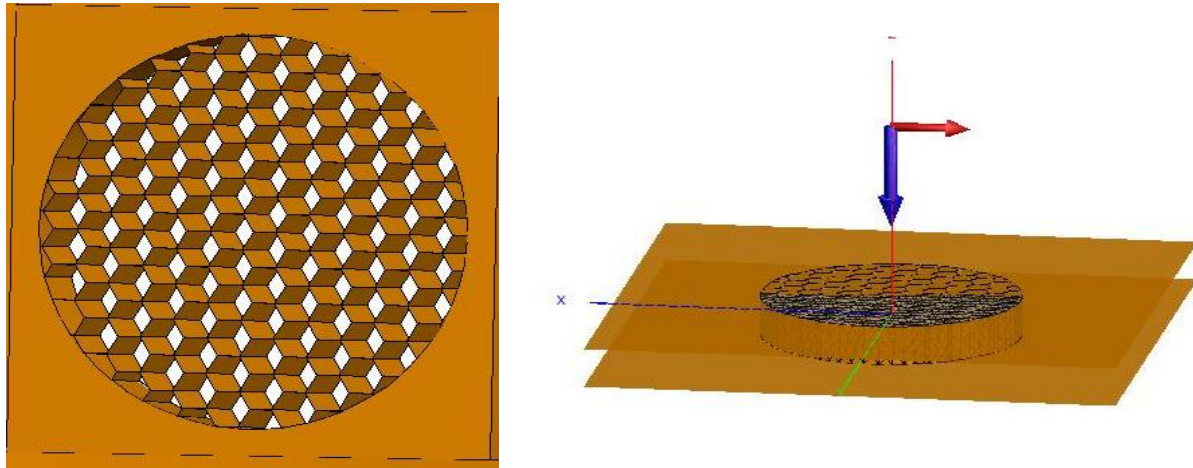
Figure 94. Honeycomb model and model in infinite plane with green's function.

The transmission through the honeycomb plane fixture is shown in Figure 95. Shielding effectiveness is calculated by equation (84) as follows.

$$SE = 20\log(\text{Incident Field/Received Field})$$

(84)

The attenuation produced from this honeycomb configuration in the 13 to 15 GHz range was 27 to 30 dB which represented a reasonable worst case and is more conservative than typical industry data [129]. The modeled honeycomb factor was then applied to the source in the open holes model and field levels within the vehicle assessed. To keep this application conservative, two additional steps were taken: (1) The highest peak found in the volume of the cavity was

considered in the shielding effectiveness calculations, and (2) A comparison model using WIPL-D HO MoM was introduced to evaluate the effect of closed holes.
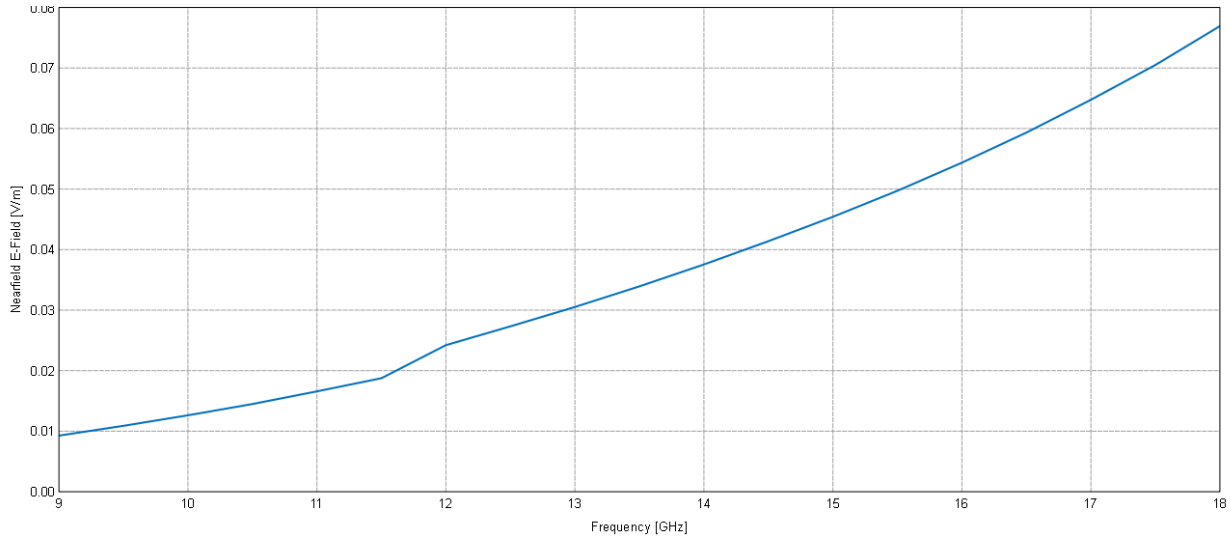
Figure 95. Honeycomb characterization results: transmission through honeycomb (1 V/m input).

Since this method applies the attenuation in the open holes model, the effect of having the honeycomb in place and thus possibly changing the resonant characteristics of the fairing was bounded by a WIPL-D fairing cross reference model with an opening the size of the largest aperture in the original MLFMM. The internal excitation voltage inside the HO MoM model is modified until the peak cavity fields match the MLFMM case with open apertures. The aperture is then closed and the worst case level from either model is used to determine the predicted shielding. The lowest predicted shielding for the prototype honeycomb model in the frequency of interest ($13 - 15$ GHz) was 30 dB. Good correlation to the honeycomb test results was

162

achieved with this approach (see Figure 96). The rotationally symmetric cross reference model is shown in Figure 97.
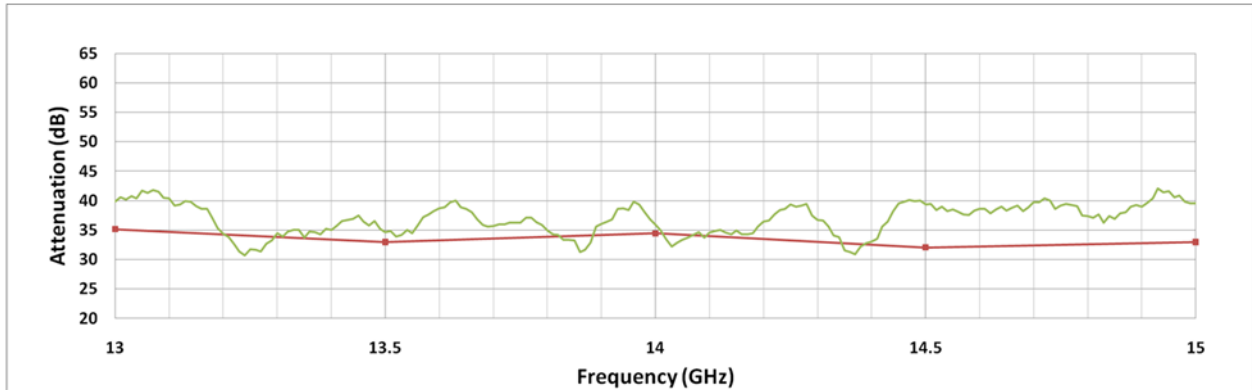
Figure 96: Test to model with honeycomb: test data moving average (green) to worst case model data (red)
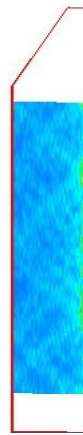
Figure 97. WIPL-D Rotationally Symmetric Model.

A summary of the shielding effectiveness evaluation approach with both MLFMM and rotationally sysmmeteric HO MoM is provided below.

o The MLFMM model is developed with open apertures and an external plane wave source

o The honeycomb is evaluated separately using the planar Green's function.

o This effect is applied to the source and the fields are obtained.

o A HO MoM rotationally symmetric model is developed to evaluate the effect of closed apertures on the fairing field distribution.

o Using both models together provides the bounding cases for the cavity fields (FEKO – open holes, WIPL-D closed holes).

o The HO MoM model excitation is modified to match the field average and peak distribution in the cavity in the MLFMM model without honeycomb.

o Apertures are then closed and the internal excitation is reduced by honeycomb factor revealed in a Green's function infinite plane model.

o Peak and average field distributions are compared between MLFMM and HO MoM to give the minimum shielding.

6.3.3   Full-Scale model

After showing reasonable comparison results for the prototype model, a full-scale vehicle was modeled with the same process. However, the numerical based MLFMM truncation error was higher for this model. One contributing factor is the more complex geometry features in the full-scale model. Additional modification of the model parameters was performed to control the error which included tightening the mesh constraints and altering the MLFMM box size. As discussed in Section 2.2, the MLFMM box size controls the portion of the near geometry that is considered for the direct MoM matrix solution. Altering the box size will affect the amount of residual, but not always in a predictable way due to instability issues addressed in Section 2.2. Hence multiple trials are needed to optimize the results. Each trial for this size fairing takes approximately two days to run, accordingly, using default settings are preferred when numerical residual is not an issue. An example of this reduction in field levels achieved by this numerical manipulation process is shown in Figure 98. In addition, the lossless dielectric method discussed

164

in previous chapters was attempted, but proved computationally prohibitive. Adding the dielectric adds two unknowns per matrix element instead of one.
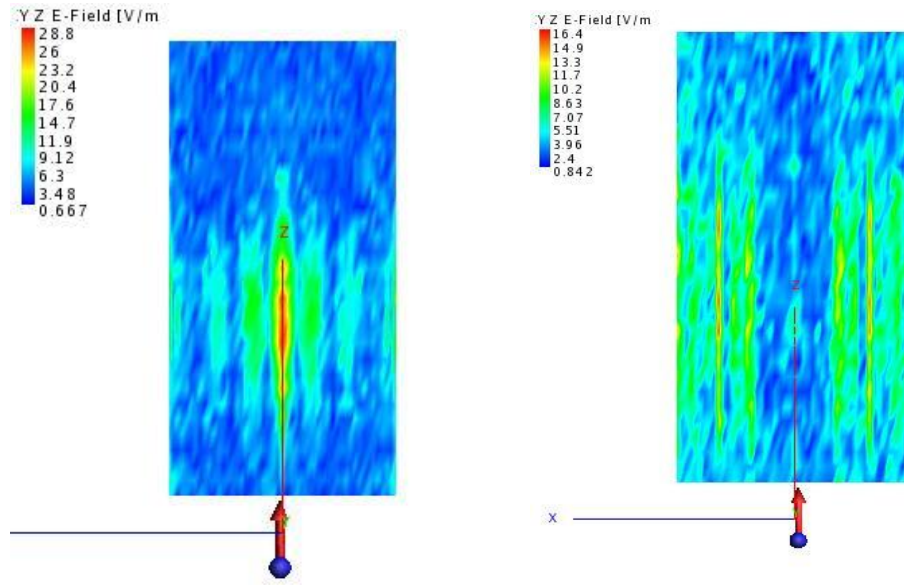
Figure 98. Full fairing field distributions at 2.2 GHz with default and modified settings (mesh λ/15, box 0.19).

Demonstration of numerical excitation is clearly seen in

Figure 98. The center hot spot was reduced almost completely by increasing the number of unknowns with a smaller mesh and implementing smaller MLFMM box size. There are limits to how much these parameters can be reduced, however, both from a memory and a numerical precision standpoint.

6.4 <u>Summary</u>

The test data revealed an inherent shielding effectiveness with the open holes structure that was also shown in the model data where the conservative PEC representation, with peak fairing fields, was used to set a bounding limit for the modeling of the sub-scale test prototype. Due to model limitations for the complex honeycomb structure, an alternate approach of indirectly applying the honeycomb attenuation to the source was used with reasonable correlation to test results. This effort has shown that 3D CEM models can be an effective tool in evaluating shielding effectiveness in launch vehicle fairing cavities and described some limits of such models.

CHAPTER 7. COMPOSITE FAIRING - EXTERNAL TRANSIENT MAGNETIC FIELD SOURCE

7.1   Introduction

In this chapter internal fairing fields and induced fields on internal fairing loops due to external transient sources are evaluated. The transient source of concern is a nearby lightning strike or indirect effects.   The attenuation of induced effects due to nearby lightning strikes by composite structures is not routinely recognized by launch vehicle providers.   Sensitive spacecraft can often not withstand the theoretical worst case induced currents and voltages.

In this research a transmission-line-matrix (TLM) model with CST Microstripes to examine interior fields and induced voltages on interior wire loops in a composite fairing due to a simulated near-by lightning strike is developed. A physical vehicle-like scaled composite fairing test fixture is used to anchor a TLM model in the time domain and a FEKO method of moments model is used in the frequency domain. Although lightning is a transient and effects are typically evaluated in the time domain, the frequency domain was considered to add insight by simulating an industry standard shielding effectiveness test before considering the transient induced effects. Results show that a typical graphite composite fairing provides attenuation resulting in a significant reduction in induced voltages on high impedance circuits despite minimal attenuation of peak magnetic fields from a near-by lightning strike propagating through the fairing walls. Parts of this research that were conducted for this dissertation are published in [130].

7.2   External Transient Source - Test Results

7.2.1   Fairing Fixture and Test Program

The test fixture is identical to that used in the composite study in CHAPTER 5.   Testing was performed in two phases to examine shielding in the frequency domain and study the attenuation of the induced effects in the time domain. Due to the transient nature of lightning, the time domain response is the primary area of interest for lightning related induced effects. As simulating exact lightning magnitudes and pulses is not feasible in a small laboratory setting, a magnetic transient source placed close by is used. To better validate the model, testing and modeling were performed in the frequency and time domains. The frequency domain test is based on an industry standard shielding method. The time domain test is based on a nearby loop designed to generate magnetic transient fields.

7.2.1.1 Frequency Domain Results

Initially, an industry standard magnetic shielding test was performed to characterize the structure's frequency response [127].   As shown in Figure 99, a loop antenna sensor is placed one meter high in the center of the fairing. To determine shielding effectiveness fields produced by the source were measured at the location of the probes with no fairing in place.

An identical loop was used to provide external excitation and internal sensing at specific frequencies. The external loop was placed one meter from the internal sensor. One half of the fairing contained a removable window with a metal reinforcing strip. In one test configuration the fairing was rotated such that the window was placed in between the sensor and the source. This test was performed in order to determine how metal lined apertures, that are typical in

launch vehicles, affect the composite fairing overall shielding effectiveness to lightning induced effects.

Frequency Domain Magnetic Loop Test
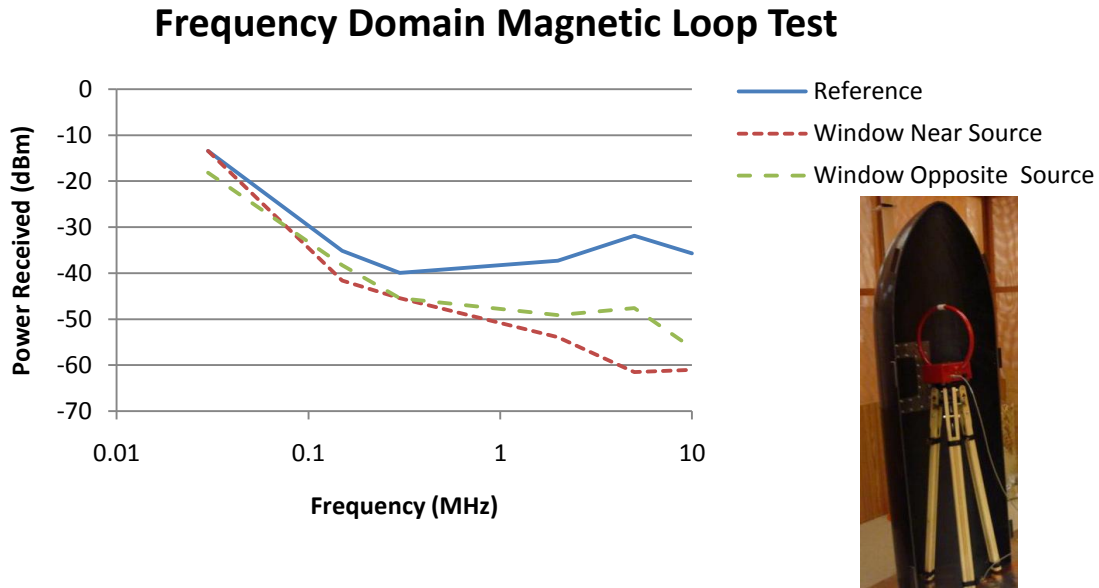
Figure 99.   Power received in composite fairing half with test source.

The test results of the power received in the composite fairing are shown in Figure 99. Frequencies beyond 10 MHz showed leakage and are not used for comparison. The sealing of the two fairing halves was done using clamps instead of conductive tape as in the RF testing described in the Section 5.2. This change was made because the conductive tape around the fairing split-line is the dominant shielding mechanism due to the induction of currents in the tape providing opposing currents to the original field. Using the tight clamp seal was effective through the 10 MHz frequency range which captures most of the range of lightning effects. Additional attenuation is achieved by the metal around the window due to induced eddy currents that oppose the incident field. As the effect seen here is similar to that of the composite without

a window, except for one frequency point, the composite structure without the metal window will be considered as a bounding case used for model comparison.

7.2.1.2 Time Domain Results

A time domain test was established to provide baseline comparison data for a model based magnetic transient source. For the time domain model a large loop driven with a transient 10 µsec pulse was used for the source, and a B-dot sensor was used to measure the change in magnetic field with respect to time. The loop was selected rather than a high voltage source for ease of implementation in the laboratory setting.

The transient source was implemented with a 2 m square PVC structure supporting a 16 gauge wire. The closest side of the loop was placed 0.5 meters from the fairing. This was proximally placed with respect to the composite fairing structure to represent a low impedance magnetic field associated with near field conditions and thus worst case (minimal) shielding of the composite fairing structure. The distal leg of current loop is selected as far as possible away from the fairing in order to limit field cancellation effects as shown in Figure 100. An Electrometrics, EM 3410, spike generator was placed at the base of the structure to drive a 10 µsec pulse into the loop and a 100 volt transient pulse was applied to the loop with a wire conductivity of 5.87×10^7 s/m and a radius of 0.15 cm. This transient current loop was selected rather than a high voltage source for feasibility of implementation in the laboratory setting. Pulses with shorter durations were available, but could not be driven into the large loop.
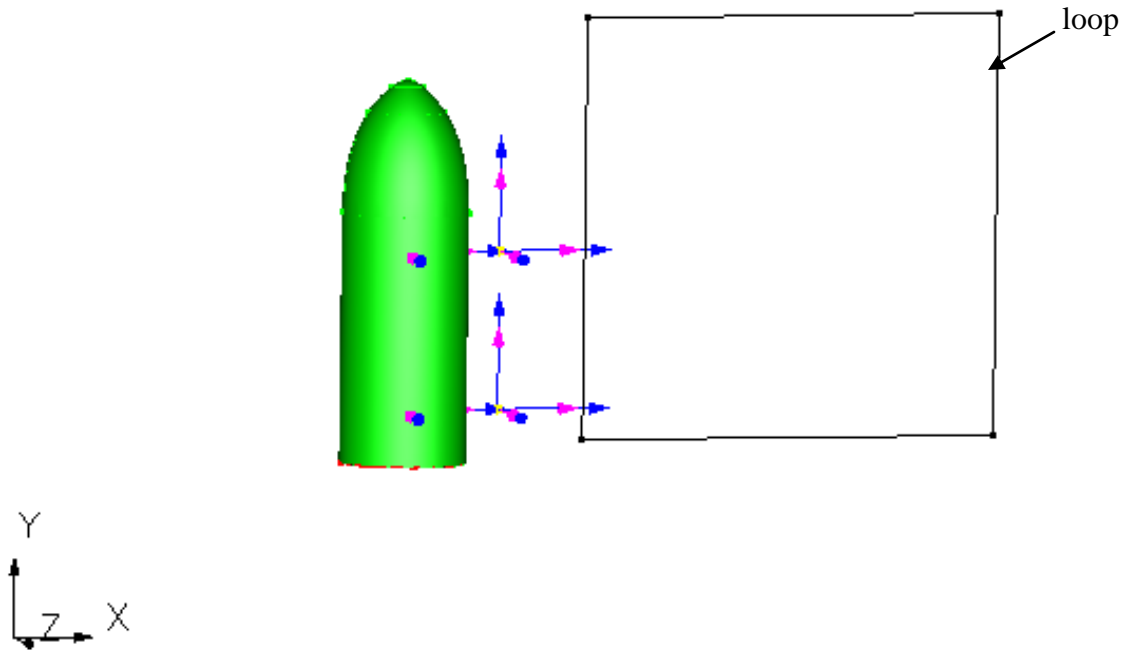
Figure 100. Composite fairing with transient current loop.

A B-dot sensor (ELGAL MDM-0) was employed in conjunction with a digital oscilloscope, to measure the change in magnetic field with respect to time. The received voltage was measured with and without the fairing in place. The reference measurement without the fairing was 54 mV and the encapsulated measurement from the B-dot sensor was 22.9 mV. Hence, the resulting shielding effectiveness was 20 log (52/22.9) = 7.4 dB.

7.3   External Transient - Modeling Results

7.3.1   Composite Structure Model

Modeling the layers of the composite fairing individually requires the mesh to be small with respect to the thickness of each layer and is computationally prohibitive with respect to the entire model size. Accordingly, as with the RF model of the composite structure in CHAPTER 5, it is desired to represent the composite with infinitely thin layers in the CEM model. Although

171

carbon fiber composite (CFC) structures are inhomogeneous and tensor formation of permittivity and permeability are needed for accurate representation of electromagnetic shielding, the frequency range of lightning is generally below the interlayer resonance of composite structures, allowing an effective one layer representation of the composite fairing [56][115]. Literature supports modeling composite materials as a single layer if the period of the structure is small with respect to wavelength [56],[130], [131]. This criterion is clearly met with a thin structure and lightning frequency content below 30 MHz [1]. Several composite builds can effectively be modeled as one layer into the GHz frequency range [56]. Therefore, each composite 4 ply layer structure was represented as an electromagnetically penetrable thin film with conductivity parameters developed from surface resistivity measurements [100].

In addition, composite material is not uniform in all directions; hence, the volume conductivity cannot entirely be determined from the surface conductivity and thickness. However, if there are several layers of composite materials, then multiple orientations of the fibers will exist allowing the standard volume resistivity calculated from surface resistance to approximate the actual conductivity of the structure [12]. The conductivity for the graphite composite layer was modeled with the uniform material assumption and calculated as shown below.

$$\sigma = \frac{1}{\rho} \qquad \rho = R_s t$$

$$\sigma = \frac{1}{(161 mohm)(1mm)} = 6211 \ s/m$$

$Where:$

$\sigma = conductivity \ in \ s/m$

$\rho = volume \ resistivity$

$R_s = surface \ resistivity$

$t = thickness$

(85)

7.3.2   Frequency Domain Model

Simulation in the frequency domain was done using the MoM approach described in Section 2.1 and an imported Pro-E fairing model. The equivalent layer model was implemented using an infinitely thin impedance sheet based on the direct surface impedance measurement. The impedance sheet represents the relationship between the tangential electric field on the surface and the electric surface current [61].   The default mesh size assigned by the program, which is based on frequency, was changed to account for geometry details. A magnetic dipole loop was used for excitation to simulate the test case. A near-field plane was placed at the center of the fairing to evaluate the received magnetic fields with and without the fairing in place.

The method of moment simulations were developed at specific frequencies to emulate the test case. The resulting shielding effectiveness was normalized with respect to the no-fairing structure case. A phase progression of the frequency domain MoM model at 10 MHz showing the diffusion process is provided in Figure 101 [51]. At this frequency, the peak levels on the skin of the vehicle are significantly diminished inside the fairing.
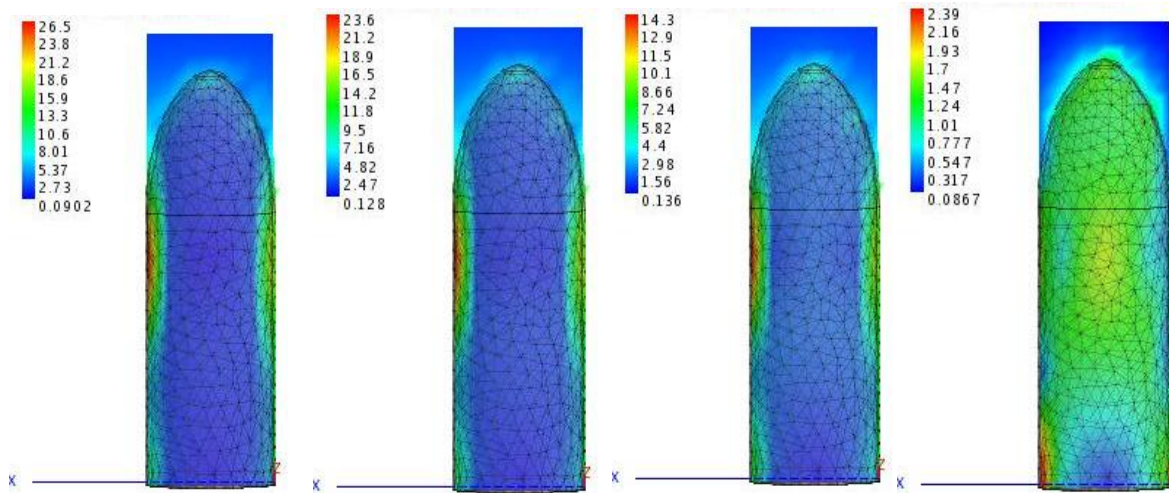
Figure 101 H-Field in Y-vertical and X-horizontal plane (ωt = 0, 30, 60, 90) at 10 MHz.

The concept of diffusion is particularly important for transient events. If the transient pulse is shorter than the diffusion time, the resulting interior signal is significantly diminished [58]. Diffusion is very slow for metals and thus metals provide excellent shielding effectiveness for time varying magnetic and electric fields [58]. Diffusion is considerably faster for composite materials at lightning frequencies due to lower conductivity, however the effect is still shown to lower the magnitude of the internal magnetic fields at higher frequencies. Both test and simulation results, shown in Table 4, indicate an increase in magnetic field shielding effectiveness with increasing frequency up to 10 MHz for the composite fairing test fixture with significant increases at 2 MHz and beyond where the skin depth of the material is on the order of the material thickness. Reasonable correlation between the model and test case is achieved.

Table 4: Frequency domain shielding comparisons

Frequency	Shielding Effectiveness (Test Data) dB	Shielding Effectiveness (Model Data) dB	Difference dB
150 kHz	2	0.9	1.1
300 kHz	5	0.8	4.2
2 MHz	11	10	1
5MHz	17	19.5	2.5
10 MHz	21	21.9	0.9

7.3.3   Time Domain Model

Given the limited frequency content in lightning transient pulses, the TLM tool in CST Microstripes is optimally applied for this electrically small structure. TLM divides the physical space into circuits that can be solved for voltages and currents that are related to fields through analogies to Maxwell's equations as described in Section 2.6 [18].

Two loop excitation waveforms were modeled.   One model, shown in Figure 102, was designed to closely characterize the transient generator pulse that could be implemented using a spike generator driving a pulse into an inductive loop as was used in the test case [54]. The other excitation waveform shown in Figure 102 represents the industry standard double exponential lighting pulse typically specified in lightning standards [52].
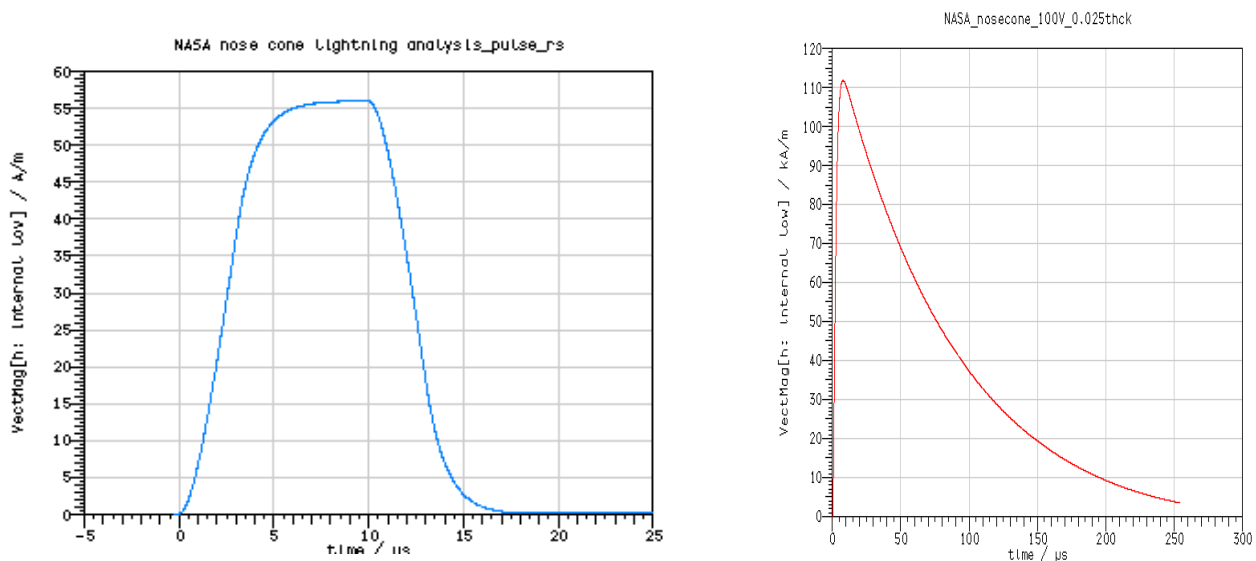
Figure 102. Transient generator (left) and double exponential (right) loop excitation waveforms.

The TLM model frequency span is set to 20 MHz for broad band evaluations, and the structure mesh size is driven by this frequency. The run time duration is extended beyond the default settings to account for the total waveform time. The laboratory loop was modeled with a 10 ohm load impedance to partially account for the inductance created by the loop. The source in the model was designed to closely characterize the transient generator pulse that could be implemented with a spike generator into an inductive loop. A 100 volt transient source is modeled with the loop conductivity set to emulate the test configuration (conductivity - 5.87×10^7 s/m, radius - 0.15 cm). The double exponential loop was modeled with zero resistance and a 10,000 volt source.

The points of maximum change in magnetic field are of primary interest to determine the worst case induced voltages as evidenced in (7).   For the purposes of this evaluation the difference in the peak change in magnetic field with respect to time, with and without the fairing,

176

represents the shielding effectiveness (SE) of the fairing as in (86). A simulated test pulse with 3 μs rise time used to evaluate the change in magnetic field amplitude produced over the rise time period is shown with and without the fairing in Figure 103. For the double exponential signal, the peak change in magnetic field was found to occur between 0.2μs and 0.4 μs as shown in Figure 104. This portion of the curve was used in attenuation comparisons to consider the composite fairings response to the most rapid magnetic field changes.

$$SE = 20 \log \left[\frac{Hnf_{t2} - Hnf_{t1}}{t_2 - t_1} \middle/ \frac{Hf_{t2} - Hf_{t1}}{t_2 - t_1} \right]$$

where

(86)

$Hnf_{t2} = Magnitude\,of\;Hfield\;without\;fairing\;at\;time\;t_2$

$Hf_{t2} = Magnitude\,of\;Hfield\;with\;fairing\;at\;time\;t_2$
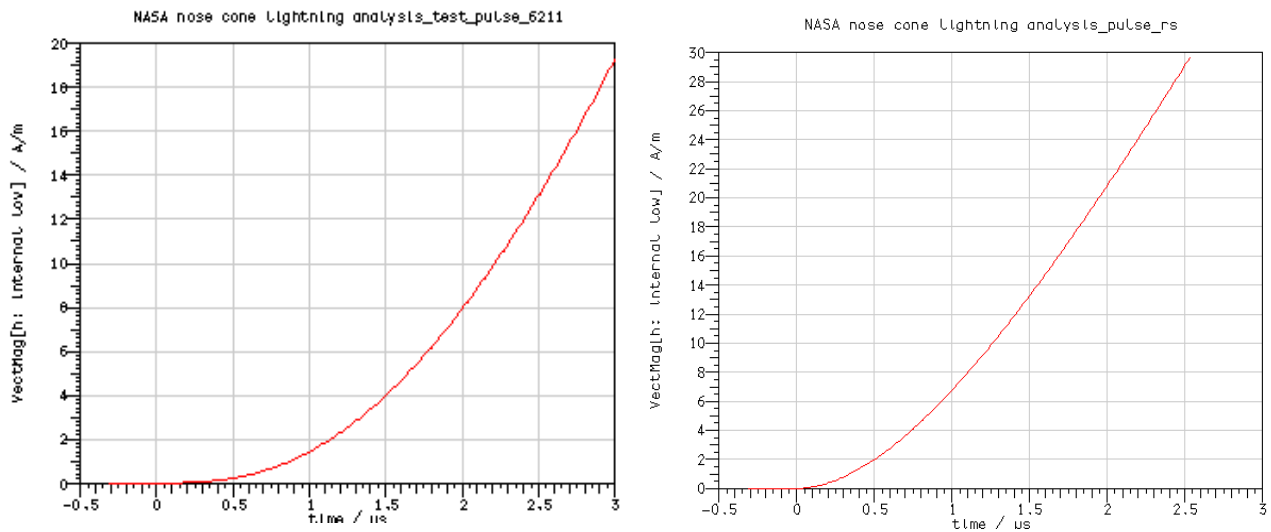
Figure 103. Magnetic field change in test composite fairing with a pulse signal model with respect to no fairing case.

As the actual test case was too inductive to support sharper rise times, this case was evaluated over the 2.5 μsec period, the change in magnetic field in this period with the composite fairing case was 13 A/m and without the fairing was 30 A/m leading to an attenuation of 20log(30/13) = 7.26 dB.
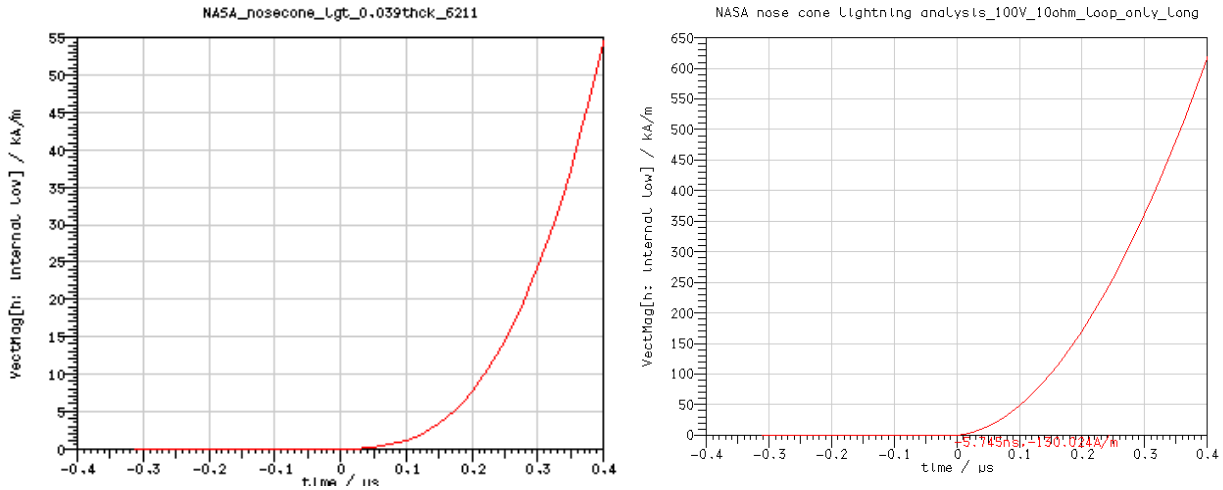
Figure 104. Magnetic field change in composite fairing with double exponential signal model with respect to no fairing case.

In Figure 104 the time period considered is 0.2 to 0.4 μsec where the sharpest rise times existed. The change in magnetic field in this period with the composite fairing was 465 kA/m and without the fairing was 45 kA/m leading to an attenuation of 20 log(465/45) = 20.3 dB.

The baseline comparison case is obtained from measurements with no fairing in place which is modeled by changing the fairing material properties to that of free space. The difference in the change in magnetic field with respect to time with and without the fairing was 7.26 dB in simulation and 7.4 dB in test, revealing good agreement between test and model results.

The double exponential pulse model was further modified in order to compare to the results of industry panel testing. The modifications included using the characteristics of industry graphite composite panels in the fairing fixture model. The panel selected for modeling had a conductivity of 11,600 S/m and thicknesses of 0.25 cm [59],[12]. The industry test in [59] was performed with a B-dot sensor in a metal box with the front wall as a removable panel. A lightning source was introduced directly in front of the removable panel. A fiberglass panel was used for the no-shielding case to compare with the shielding achieved with graphite composite panels. The double exponential wave form was used and the voltage pulse was set to give currents in the kA range more typical of lightning strikes. Using these values with the thin film model in the TLM tool, shielding from dB/dt values were obtained at 38 dB as shown in Figure 105.
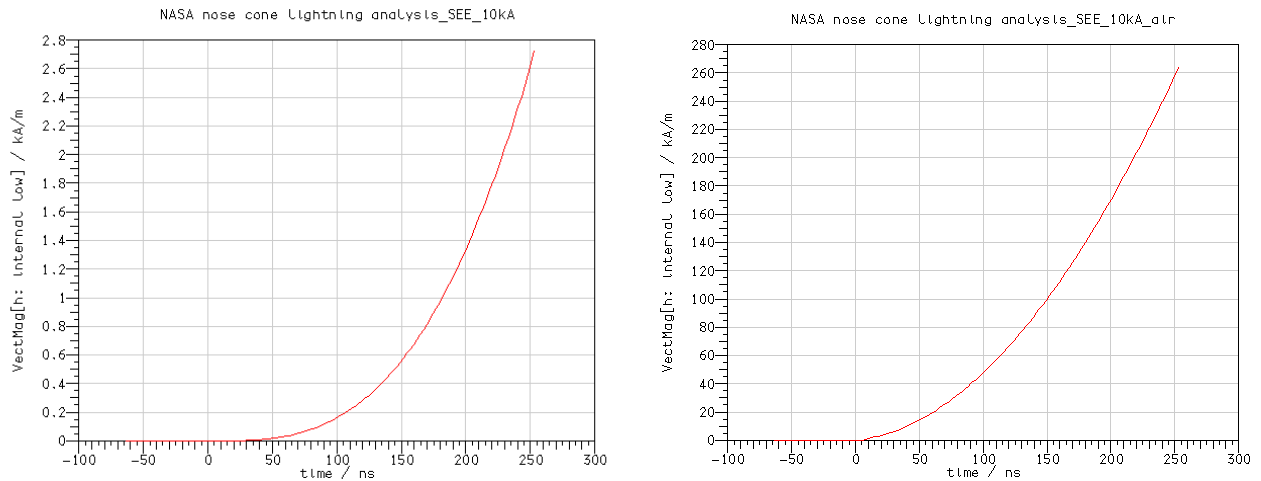
Figure 105. Magnetic field change in composite fairing (11,600 S/m) with high voltage double exponential signal model representative of industry testing with respect to no fairing case.

The peak change in this case occurred from 150 ns to 250 ns. The change in magnetic field in this period with the industry composite fairing properties modeled was 165 KA/m and without the fairing was 2 kA/m giving an attenuation of 20 log(165/2) = 38.3dB.

A summary of the time domain comparisons are shown in Table 5.

Table 5. Time Domain Comparisons

Configuration	Pulse Type	TLM Model Shielding (dB)	Test Shielding
Fairing Fixture	Spike Generator Pulse	7.26	7.4
Fairing Fixture	Double Exponential	20.3	---
Industry Graphite 0.098 inches	Double Exponential	38.3	42.9 – 44.6 (similar panel tests)

The time domain model predicts similar shielding effectiveness to the change in magnetic field as the test case. The same model with the double exponential pulse for excitation indicates higher shielding effectiveness. In this exponential case the faster rise portion of the curve was evaluated and the higher attenuation of these fields was found. Literature evaluation of Gaussian and double exponential transient pulse shielding of composite structures showed similar dependence on the pulse type [55]. The TLM time domain model shown modified with the material properties of the industry test panels showed attenuation of the rate of change of magnetic field in the fairing comparable to industry data [59],[14],[55].

7.3.4 Induced Effects Model

In the simulation done above, the actual laboratory loop set-up was modeled. To eliminate the lab setting constraint and to examine voltages induced in loops the simulation configuration was modified. First, to represent a nearby lighting strike, a 1MV/1Mohm source at the top of a 30 foot long simulated lightning channel was for the source loop in the model as shown in Figure 106 [132]. To reduce electric field contributions, the source was shielded with a graphite epoxy box.
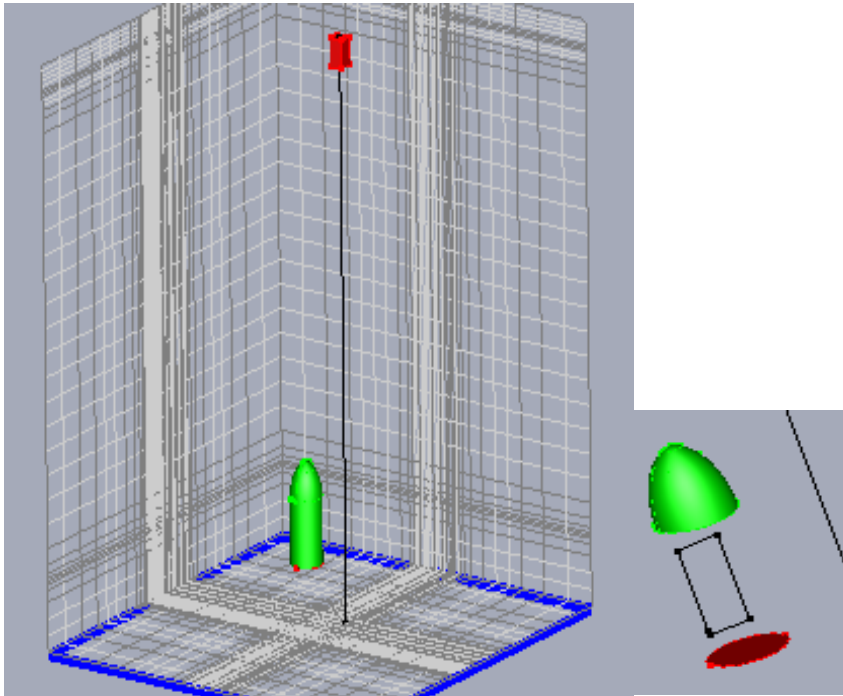
Figure 106. Composite fairing with a simulated lightning source.

The source was driven by the double exponential characteristics given in (87) which are based on MIL-STD-464 [52].

$$i(t) = I_0(e^{-\alpha t} - e^{-\beta t}) \tag{ 87 }$$

Where: $I_0 = 218{,}810$ A, $\alpha = 11{,}354$ s^{-1} and $\beta = 647{,}265$ s^{-1}

In addition, a loop was added in the simulated vehicle to examine currents and voltages on low and high impedance circuitry within the fairing with respect to magnetic field peak reduction. Figure 107 shows the low resistance circuit response excited by a simulated nearby (1 m away) lightning strike with and without a composite fairing surrounding the loop. Figure 108 indicates the high impedance circuit response for the same case. Although peak magnetic field coupling is similar with and without the fairing in place, the rise time is longer with the fairing in place leading to lower induced voltages in interior circuits. As evident in (7), Figure 108 reveals a much sharper peak in induced voltage for the air (no-fairing) case due to the derivative relationship between this voltage and the magnetic field rise time. When the coupled voltage is dominant, as in high impedance circuits, the variation in induced effects is influenced by the diffusion process which slows the rise of the magnetic field [58]. The effect is much less dominant in the low impedance circuit.
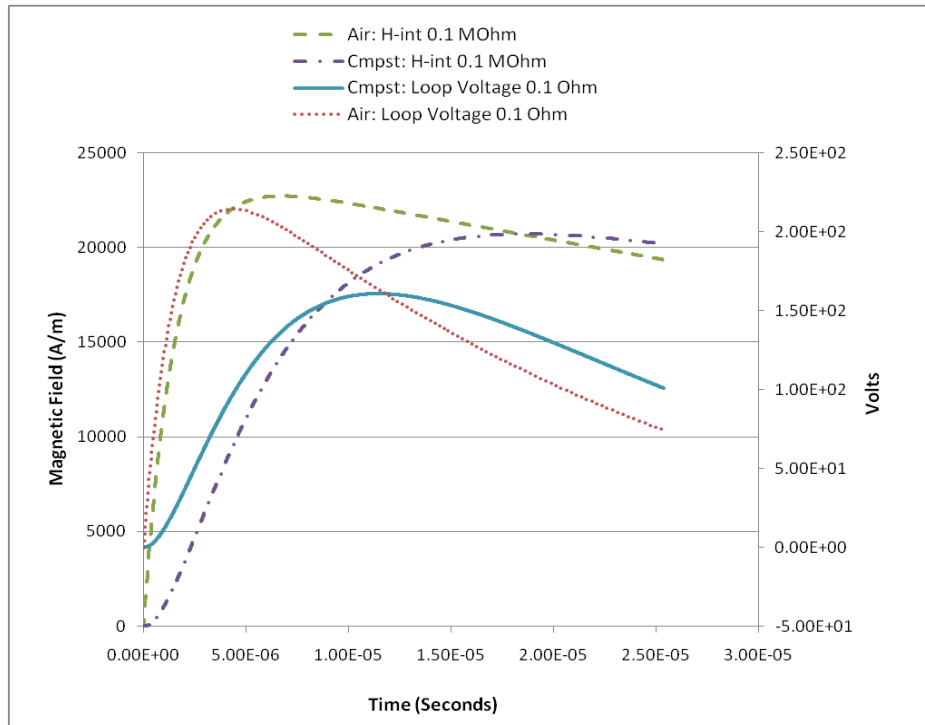
Figure 107.   Composite fairing to air comparison with low impedance internal loop coupling.
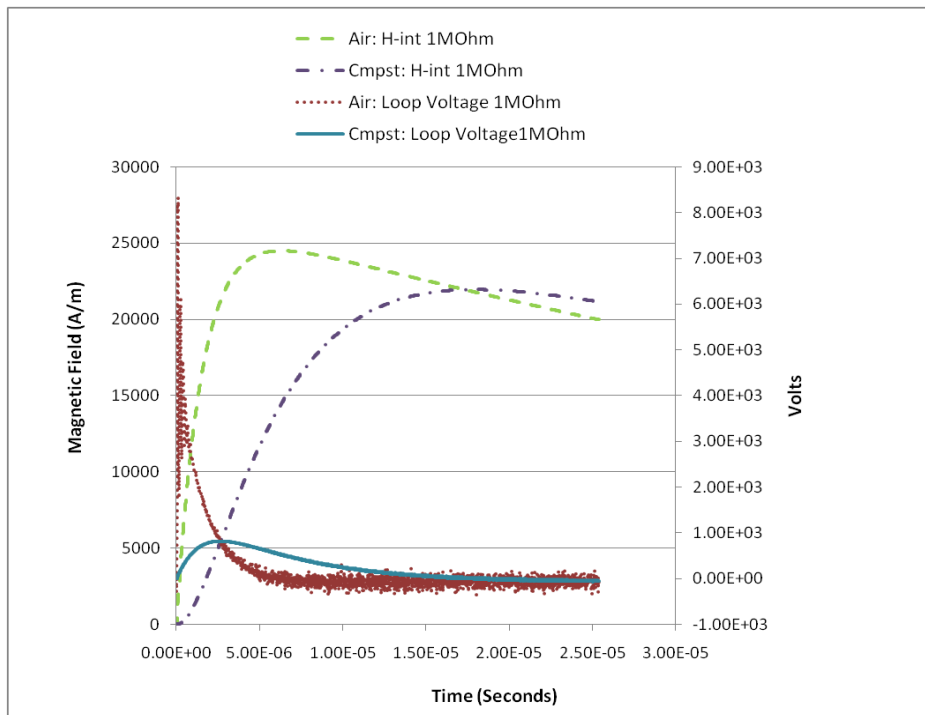
Figure 108. Composite fairing to air comparison with high impedance internal loop coupling.

183

Table 6   provides a comparison of fairing attenuation of induced effects for varying internal loop impedance and distance from source. The plane wave case provides the greatest attenuation due to the higher source impedance of the field with respect to the composite structures. Nevertheless, significant attenuation of induced voltage in the high impedance loop is achieved at close distances where the source impedance is lower than a plane wave.

Table 6:   Comparison of fairing attenuation of induced effects for varying internal loop impedance and distance from source

Loop Impedance Ohms	0.1	1M			
Distance (m)	1	1	3	10	Plane Wave
Induced Voltage Attenuation (dB)	1.5	20.1	20	18.22	31
Magnetic Field Attenuation (dB)	0.8	1.04	.93	1.06	0.87

7.4   Summary

The results presented show that the TLM thin film modeling of the composite structure is effective for evaluating attenuation of transient magnetic fields within the fairing.

The model was modified to align with the industry approach for lightning induced electromagnetic effects. Results shown indicate that a typical graphite composite fairing provides significant reduction in induced voltages on high impedance circuits despite minimal attenuation of peak magnetic fields. The energy in the pulse is spread by the diffusion process through the composite material, and this spreading slows the incident pulse rise time which in turn reduces the coupling to the circuit.

This study provides a good insight and provides accurate results for attenuation of lightning induced effects by composite fairing structures. It fills in a big void in the literature and in industry data related to lighting induced effects. The data from this effort will also be useful for evaluating spacecraft/launch vehicle de-stack criteria.

CHAPTER 8. CONCLUSION

8.1   Model Approach and Configurations

In this dissertation, a comprehensive computational modeling task to evaluate internal launch vehicle fairing fields due to internal and external sources has been presented. The fairing field analysis presents many challenges due to the field that these are electrically large cavity structures at frequencies of interest, i.e., C, S, and X bands. Each model was anchored with physical test results. This is essential for two reasons: 1) the electromagnetic compatibility discipline is historically test based, and 2) there is a lack of literature providing verification of CEM tools used in cavity structures. The methodology of each pertinent, existing CEM tool solution implementation was examined to understand the capabilities and limits of the model. First, internal fairing fields due to internal emitters represented by double ridge guide horns were modeled in a metallic fairing. The limitations of CEM tools using MLFMM and HO MoM techniques were identified and mitigating strategies in evaluating internal fields in highly resonant structures. Next, the fairing with acoustic blanketing layers with RF absorbing properties was modeled. Equivalent impedance strategies were adapted for application within the CEM tools to provide efficient models. The layering features available within the tools were examined and again limitations of such features identified and corrected for this analysis. Composite fairing evaluations were then performed using the same equivalent impedance techniques. The test method was altered to allow for greater visibility of field distribution within the cavity. Chi 2 DOF statistical examination was then utilized and it was seen that both test and model data followed this distribution. The addition of a spacecraft load within the fairing was evaluated to determine its effect on fairing fields and the statistical field distribution. Shielding

effectiveness models of a separate metallic fairing with intentional apertures was then undertaken. Computational limitations specific to problems requiring a large dynamic range were discussed. A detailed model of a honeycomb shielding method was then evaluated with planar Green's function models with the resulting attenuation applied to the source. A rotationally symmetric model was used to further evaluate the internal fields in a closed fairing. In all cases, reasonable results were achieved over the modeled frequency range, comparisons were made to industry techniques, and limitations of the CEM techniques identified. Summary tables are included in the appendices.

Finally, lightning induced effects were examined for the composite structure using TLM. This was essentially a separate study from the other topics due to the transient nature of lightning as well as its low frequency content relative to the previously considered S and C Band transmitters. This evaluation was important for the composite fairing because launch developers assume the fairing provides no attenuation to lightning induced effects. Again, a laboratory fixture was designed and used to validate the model results. Modification of the model was then made to match industry studies. The results showed a significant reduction in coupling to interior high impedance circuits and little to no reduction in interior peak magnitude field. These results are important when considering sensitive circuits interior to the vehicle fairing during nearby lightning strikes.

8.2   Test to Model Comparison Considerations

Model to test comparisons are essential to show applicability of CEM techniques to a discipline historically dependent on test data. However, test to model comparisons are difficult to realize on large complex structures. Determining these fields in closed cavities presents further challenges for both models and test as discussed in the previous section. Some of the recommendations for launch vehicle CEM model to test comparisons are given below:

Excitation Source:

o The transmit antenna should be much smaller than cavity and electrically far from cavity walls to prevent significant pattern mutation by antenna to cavity capacitance.

o Use transmit antennas with easily implementable structures such as dipoles. Models of complex antennas will require significantly more unknowns to solve.

o Generally better results are obtained by including the source in the model rather than using pattern only simulations. Unavailability of necessary correlated phase data from antenna manufactures requires the development of the antenna model to obtain the needed pattern information.

o When transmit and receive antennas are used, account for the antenna measurement distance assumptions in the field pattern. For example, the antenna dimensions of the Double Ridge Guide Horn and similar antennas are large. The receive antenna may not be in the far field of the source antenna such that the distance between antennas is less than $2d^2/\lambda$ where d is the largest antenna dimension [113].

o Measure antenna VSWR for each change in lining/load in the cavity - Models typically have an excitation voltage and do not automatically account for a change in this input due to VSWR effects for structures surrounding the antenna.

Field Data:

o Use flat response probes for measurement (variations in probe factor near the frequency of interest will likely be skewed by surrounding cavity).

o Use fiber optic field probes for receive measurements to prevent interaction with receive antenna wiring.

o Vary location of receive probe within the cavity to obtain a statistical distribution correlation.

o Use multiple frequencies for correlation with statistical distributions. Minor differences in test and model conditions will contribute to frequency shifts.

o Consider only one component (at a time) in comparisons, as magnitude results can be unreliable due to skewed probe factors in cavities.

o Use small probes – probes are necessarily averaged over their size while cavity fields can change significantly from point to point. This will more closely simulate the field data available at infinitesimal points by the CEM tool. These also have less disturbance of the field being measured.

o Note probe settling time and adjust sweep rates accordingly.

8.3   <u>Summary</u>

In this dissertation various available CEM tools were examined for the determination of fairing cavity fields.   Modifications were made to extend their applications and remove the limitations to their use with electrically large cavity structures.   The results obtained are compared with test data and found to agree well. In addition, the results presented here provide a more accurate and in depth knowledge of fairing fields due to internal and external sources and greatly expand the information that is currently available in the literature.   A summary of the work done is given below.

1. Examined applicable CEM techniques for internal and external sources for a broad range of anchored fairing cases identifying recommendations and limitations for determining fields in cavities for each case which can be applied outside of the LV industry.

2. Applied equivalent impedance techniques to form methods to implement material electrical parameters and developed modeling techniques to mitigate CEM tool layering constraints.

3. Developed a comparison of fairing model data to statistical and power balance techniques used in industry to show applicability to launch vehicle CEM models used in the industry.

4. Developed specific fairing test to model comparison recommendations.

APPENDIX A: ADDITIONAL MODELING SUMMARIES

A summary of the fairing cases studied and techniques used is provided in Table 7.

Table 7: Comparison of CEM tools used for fairing field analysis

Fairing Configuration (S and C Band Sources)	MLFMM/RWG 16 parallel processors 128 G RAM total	HO MoM 80,000 unknowns
Closed metallic fairing with internal source	Convergence issues above 2.1 GHz using antenna pattern based source in PEC Cavity	Distributed Impedance model with aluminum resistance in GHz range. Increase integral accuracy for interior cavity model.
Metallic fairing with thin blankets and internal source	Two layer CAD model Outer walls – lossy metal Inner layer(s) – impedance sheet with blanket resistance	Distributed impedance one layer model with Hallet Redell equivalent
Metallic fairing and thick blankets with internal source	Three layer CAD model (as above) Single Layer - Metal with coating option Coating is applied as a thin dielectric sheet implemented by adapted NRW technique with $\mu_r = 1$	Two layer model required greater than 80,000 unknowns.
Internal source composite fairing	Impedance Sheet with adapted NRW technique as above for composite	Distributed Impedance with adapted NRW technique for a one layer model
Loaded Cavity with internal source	Load is evaluated only with adequate absorption to prevent interior resonance and resulting MLFMM instabilities.	Increasing order of basis function, decreasing mesh size and adding an artificial dielectric applied to prevent the EFIE null solution. Adding the Dielectric was most effective at deleting interior load cavity resonance, but all methods compared well for predicting fairing fields.
Metallic fairing with apertures (open and covered with honeycomb material) with external source.	With PEC structure and plane wave external source, the residual solution was adequately low to determine shielding in open aperture case. A separate Green's function model applied to source to evaluate honeycomb application effects and overcome dynamic range issues. Alteration of MLFMM box size and decreased mesh size to reduce residual in full scale model.	Used in conjunction with MLFMM model to evaluate closed cavity fields after honeycomb is applied.

Overall Model Limitations and Associated Mitigations

A description of the limitations of CEM and possible mitigating strategies are provided in Table 8. The CEM tool documentation does not fully describe these issues as the primary use of these tools is for open structures. An understanding of why these limitations exist and how to implement models effectively is essential for using the CEM tools for interior cavity field solutions.

Table 8: CEM Tool Limitations/Mitigations

CEM Tool Limitation	Description	Applicable Mitigation Techniques
EFIE Null Space Solution	When illuminating a closed cavity, the Dirichlet and Neumann boundary conditions of these closed cavities lead to indefinite solutions at the internal resonances of the structure. These are called null space solutions.	CFIE, a linear combination of the EFIE and MFIE equations can be applied for closed PEC structures. Artificial internal dielectrics structures with properties similar to air to force the PMCHW solution.
Discretization Error	For MoM, and other CEM solvers, it is necessary to discretize the structure. Discretization error can occur due to assumptions made regarding the currents on the discretized unit (triangle, quadrilateral, etc.). Discretization can make the null space solution error more pronounced as the resonant solution can occur over a wider range of frequencies.	Smaller segmentation of the structure will increase continuity. Use of higher order basis functions to allow more variation of the currents on a single discretized unit.
MLFMM Errors	Errors related to truncation and convergence	Reducing the mesh size to allow for a more accurate representation of linear elements is effective at reducing this error. If memory allows, $\lambda/15$ improved the results over the default $\lambda/8$ setting by almost 6 dB. The run times will increase in proportion to the decrease in mesh size. Alter box size Increase iterations Decrease allowable Residuum
Integration and Round-off Errors	Error caused by approximation in integral functions and rounding errors	Decrease mesh size Improve Integral Accuracy (WIPL-D) Double precision settings (FEKO)

Equivalent Techniques Summary

Applicability descriptions for the adapted material parameter/impedance techniques are given in Table 9. These techniques were essential to overcome tool assumption limitations regarding material property electrical thickness and surrounding free space impingement.

Table 9: Equivalent Technique and Application

Equivalent Material Parameter Technique	Description	Application
Hallet Redell Vehicle Impedance	Apply (83) serially to outer, then inner layers.	When single very electrically thin layer is applied to metal and single impedance is required
NRW Technique	Use NRW measurement technique described in 2.7.4 to multilayered or inhomogeneous sample of material representative of configuration thickness. Apply method in section 4.3.2.2 to extract equivalent permittivity and permeability from S_{11} data for homogeneous sample of the same thickness. For coating applications, the permeability should be set to 1 to match tool constraints. Obtain equivalent impedance per Section 2.7.1 Use FEM or MoM waveguide models to alter thickness of equivalent homogeneous sample to allowable tool properties (number of skin depths, electrically thin, etc).	For thick layered materials and inhomogeneous materials where single equivalent material parameters are required. If layers are very thin, measurement results are unstable.
Surface Resistance Model	Measure DC surface resistance and implement in an impedance sheet.	Lightning studies of composite structures

MLFMM Error Factor Summary in Cavities

MLFMM has been shown to be an important method to extend the full wave MoM solution to electrically larger structures. The major CEM tools designed to solve this class of

problem include this technique with model material representation and layering features that are suitable for launch vehicle problems. This study revealed limits to this method for cavity implementations. A brief summary of the error source and effective error reduction techniques discussed in this dissertation is provided below. The underlying equations and processes are described in Section 2.2.

Truncation: Manipulations made to the Green's function expressions are mathematically exact when using an infinite series. As some limit must be applied to the series to express it through computational means, a truncation error is introduced. These truncation errors are exaggerated for EFIE solutions of highly resonant structures due to the indefiniteness of these integrals and convergence is often not achieved. The degree to which this error is a problem depends on the dynamic range desired in the problem. For example shielding effectiveness problems typically require a high dynamic range. For cavities, this error will provide an additional numerical excitation that will skew the results higher than the actual levels.

Stability: The summation and integration functions are reversed in the Green's function expansion to make it possible to separate the regions into near and far fields in the MLFMM process. When the Green's function is applied, it is expressed with a Hankel function that becomes divergent with large arguments. Thus increasing the truncation variable can contribute to divergence of the solution.

Size of Box: The boxing algorithm in MLFMM also has a duplicitous nature. The larger the box area, the larger the area that direct MoM is applied. This causes a better solution within that area and consumes more resources. It also causes the neighboring boxes with larger box areas to be solved with direct MoM. However, the larger the box, the poorer the correlation of the points within that box to a central point for translation of effects from and to other boxes. If the boxes

195

are too small, the neighboring boxes beyond the immediate neighbors could be still too close for Green's function accuracy.

Preconditioner Error – To obtain a better solution in MLFMM, an iterative process is used to obtain a minimum residual error. The matrix in turn is preconditioned make this iterative process efficient. Typically methods are employed to avoid time and memory consuming matrix inversions in favor of iterative multiplication schemes. Some preconditioning schemes make assumptions about using only close diagonal elements in the matrix. For parallelization, preconditioning is used so that tasks can be divided among processors. Error can be introduced in each of these steps.

For each type of MLFMM related error, accentuation of the error is evident in cavity problems. The assumption that far away elements will have less impact is valid for most open structures, but can lead to errors for highly resonant cavity structures where eigenmode mode development due to cavity wall boundary conditions can dominate.

Mitigating Factors:

First, allotting for any wall or within cavity absorption conditions will decrease residual error. Altering the box size in MLFMM is the biggest impact on stability. Smaller size can improve the truncation error, but can also cause this instability mentioned above. This instability can often be seen in iterations when the solution begins to slowly converge and suddenly becomes divergent. The CEM tool will select the solution with the lowest residual for the final solution. The number of MLFMM iterations can also be controlled as well as the desired residual error. However, the default values of these parameters are seldom reached in resonant cavity situations and controlling the precision of the solution has a greater effect. For instance, using double precision and decreasing the mesh size can significantly reduce residual error. The

196

preconditioner can also be selected. The standard ILU method allows for increasing the matrix elements on the diagonal for more accuracy. This option is not available for multiple processor runs. For multiprocessor runs, the reducing the number of processors can improve divergence. This decreases overhead operations between processors that can affect the residual.

APPENDIX B: PERMISSIONS

ACES Copyright Transfer

Hello Mrs. Trout,

My name is Sladjana Maric and I am part of WIPL-D team. Milos is now working in our Application department. I am assigned for doing all the jobs regarding sales activity and tech support for our software in USA. In the future, if you have any questions or you need any assistance from WIPL-D team, you can contact me directly.

Regarding the e-mail you sent, you were right, the question is for professor Kolundizja rather than for somebody from Sales and Tech support department. I spoke with professor on this and he is giving you the permission to use the mentioned formulas and theory described in User's Manual.

Good luck with your thesis!

I hope that we will have a good cooperation in the future. If you have any questions, feel free to contact me.

Best regards,
Sladjana

Monday, January 30, 2012, 6:22:53 AM, you wrote:

> Hi Milos,

> This may be a question for Dr. Kolundzija, but I didn't have his e-mail.
>
> I plan to discuss higher order basis functions in my dissertation as
> my advisor wanted me to discuss the methods used in the various
> computational tools I used. I thought the discussion in the WIPL-D
> user's guide was good to show how the continuity equation constraint
> is added to the basis function so that the Galerkin testing function
> can be used. I am writing this to request permission to show
> equations 4.18, 4.19, 4.21 and 4.23 in my dissertation with the
> reference to the user's guide of course and some summary discussion.
> I also wanted to show equation 4.33 for the plates application without
> any derivation or discussion. I can use different references if
> WIPL-D would prefer that I didn't show these equations. I do
> appreciate in either case that WIPL-D makes these
> available to the user as it has been quite helpful.   I included an
> excerpt from the user's guide below so that it is clear to which
> equations I am referring. If this section should not be referenced, I
> will be glad to reference something else in open literature.
>
> Thank you,
> Dawn Trout
>

LIST OF REFERENCES

[1] R. Brewer and D. Trout, "Modern Spacecraft, Antique Specifications," in *IEEE International Symposium on Electromagnetic Compatibility*, San Jose, Aug, 2006, pp. pp 213-218.

[2] D. H. Trout, P. F. Wahid, and J. E. Stanley, "Electromagnetic cavity effects from transmitters inside a launch vehicle fairing," IEEE EMC Symposium," in *Proceedings of IEEE EMC Symposium on EMC*, Austin, 2009, pp. 70-74.

[3] C. Lewis, D. H. Trout, M.E Krome, and T.A. Perry, "NASA Applications for computational electromagnetic analaysis," in *ACES Conference*, Williamsburg, March 2011.

[4] M. Mardiguian, *Controlling radiated emissions by design*. New York: Chapman and Hall, 1992.

[5] D. White, *A Handbook Series on Electromagnetic Interference and Compatibility*. Germantown, Maryland: Don White Consultants, 1973, vol. 3.

[6] C. R. Paul, *Introduction to Electromagnetic Compatiblity*. New York: John Wiley and Sons, Inc., 1992.

[7] R. C. Scully, B. M. Kent, B.M. K. A. Brezinsk, and D. Kempf, "Radio frequency (RF) attenuation measurements of the space shuttle vehicle Electromagnetic Compatibility, 2006. EMC 2006," in *2006 IEEE International Symposium on EMC*, vol. 1, Portland, 2006, pp. 224 – 227.

[8] W. Winter and M. Herbrig, "Time Domain Measurements in Automotive Applications,"

, Austin, 2009, pp. 109 -115.

[9] V. Rajaman, C.F. Bunting, M. D. Deshpande, and Z. A. Khan, "Validation of modal/MoM in shielding effectiveness studies of rectangular enclosures with apertures," *IEEE Transactions on Electromagnetic Compatibility*, vol. 48, no. 2, pp. 348-353, May 2006.

[10] M. Li et al., "EMI from Cavity Modes of Shielding Enclosures – FDTD Modeling and Measurements," vol. 42, no. 1, February 2000.

[11] M. D. Deshpand, "Electromagnetic Field Penetraion Studies," NASA, NASA/CR-2000-210297, 2000.

[12] R.W. Evans, "Design Guidelines for Shielding Effectiveness, Current Carrying Capability and the Enhancement of Conductivity of Composite Materials," CR 4784, August 1997.

[13] G. Szatkowski, "Lightning Damage Diagnosis Research for Composite Aircraft," , November 17-19, 2009.

[14] M. S. Sarto, "A new model for the FDTD analysis of shielding performance of composite structures," *IEEE Transactions on EMC*, vol. 41, no. 4, pp. 298-306, November 1999.

[15] H. Uberall, B. F. Howell, and E.L. Diamond, "Effective medium theory and the attenuation of graphite fiber composites," *Journal of Applied Physics*, vol. 73, no. 7, pp. 3441-3445, April 1993.

[16] C A. Grosvenor et al., "Electromagnetic Penetration Studies for Three Different

Aircraft," in *IEEE International Symposium on Electromagnetic Compatibility*, Austin, 2009, pp. 24-29.

[17] M. Hallett and J. Redell, "Technique for Predicting the RF Field Strength Inside and Enclosure," NASA/TP – 1998-206864, 1998.

[18] D. Pozar, *Microwave Engineering, Third Edition*. Amherst: Wiley, 2005.

[19] J. Van Bladel, *Electromagnetic Fields*. New York: Hemisphere Publishing Corporation, 1985.

[20] C. A. Balanis, *Advanced Engineering Electromagnetics*. New York: Wiley, 1989.

[21] A. Navarro, M.J. Nufiez, and E. Martin, "Finite difference time domain FFT method applied to axially symmetrical electromagnetic resonant devices," *IEEE Proceedings*, vol. 137, Pt.H, no. 3, 1990.

[22] J.M. Jin and J.L. Volakis, "Electromagnetic Scattering and Radiation from Microstrip Patch Antennas and Arrays Residing in a Cavity," University of Michigan, 027723-1-T, 1990.

[23] D. H. Trout, J. E. Stanley, and P F. Wahid, "Electromagnetic Launch Vehicle Fairing and Acoustic Blanket Model of Received Power using FEKO," *Applied Computational Electromagnetics Journal*, vol. 26, no. 12, pp. 973-980, December 2011.

[24] D. A. Hill et al., "Aperture excitation of electrically large, lossy cavities," *IEEE Trans. Electromagn. Compat*, vol. 36, no. 3, pp. 169–177, Aug 1994.

[25] A. Schaffar and P. N. Gineste, "Application of the power balance methods to E- field calculation in the ARIANE 5 launcher payloads cavities," in *International symposium*

on EMC, Long Beach, 2011, pp. 284-289.

[26] J. Liu, X. Zhao, and K. M. Huang, "The probability Distribution of the EM Fields in Single-cavity System and the Applicatin of the PWB method," *PIERS (Progress In Electromagnetics Research) Online*, vol. 6, no. 2, 2010.

[27] G. Orjubin, E. Richalot, S. Mengu´e, M. Wong, and O. Picon, "On the FEM Modal Approach for a Reverberation Chamber Analysis,".

[28] S. Yu and C.Bunting, "Statistical investigation of frequency-stirred reverberation chambers," in *Proceedings of 2003 IEEE Interantional Symposium on Electromagnetic Compatibility*, vol. 1, 2003, pp. 155 - 159.

[29] A. Cicchi and F. Moglie V. M Primiani, "Analysis of antenna behavior in a multipath environment generated by a reverberation chamber," in *IEEE EMC Symposium 2009*, Austin, 2009, pp. 75 - 80, August.

[30] J. Ladbury, G. Koepke, and D. Camell, "Evaluation of the NASA Langley Research Center Mode-Stirred Chamber Facility," NIST, Technical Note 1508, 1999.

[31] G. J. Freyer and M.G. Backstrom, "Comparison of Anechoic and Revereration Chamber Coupling Data as a Function of Directivity Pattern- Part II," in *IEEE International Symposium on Electromagnetic Compatibility,* , Montreal, 2001, pp. 286 - 291 vol.1.

[32] C. F. Bunting, K. J. Moeller, C. J. Reddy, and and S. A. Scearce, "A two-dimentsional finite-element analysis of reverberation chambers," *IEEE Trans. Eelctromagnetic Compatibility*, vol. 41, no. 4, pp. 280-289, Nov 1999.

[33] V Rajamani, C.F Bunting, and J. C West, "Calibration of a numerically modeled

reverberation chamber," in *IEEE International Symposium on Electromagnetic Compatibility* , Austin, 2009, pp. 87-91.

[34] U. Carlberg, P. S. Kildal, A. Wolfgang, O. Sotoudeh, and C. Orlenius, "Calculated and measured absorption cross sections of lossy objects in reverberation chamber," *IEEE Transactions on Electromagentic Compatibility*, vol. 46, no. 2, pp. 146-154, May 2004.

[35] J. P. Durbano, F. E. Ortiz, J. R. Humphrey, D. W. Prather, and M. S. Mirotznik, "Implementation of Three-Dimensional FPGA-Based FDTD Solvers," in *11th Annual IEEE Symposium on Field-Programmable Custom Computing Machines*, 2003, pp. 269-270.

[36] R.T. Johnk et al., "Time-domain pulsed measurements of the NASA Space Power Facility," in *IEEE Symposium on EMC*, Austin, 2009.

[37] H. Zhao and Z. Shen, "Modal-Expansion Analysis of a Monopole in Reverberation Chamber," *Progress In Electromagnetics Research*, vol. 85, pp. 303-322, 2008.

[38] S. Nishizawa and O. Hashimoto, "Effectiveness Analysis of Lossy Dielectric Shields for a Three-Layered Human Model," *IEEE Transactions on Microwave Theory and Techniques,* , vol. 47, no. 3, pp. 277 - 283 , March 1999.

[39] G.J. Freyer, M.O. Hatfield, and M.B. Slocum, "Characterization of the electromagnetic environment in aircraft cavities excited by internal and external sources," in *15th AIAA/IEEE Digital Avionics Systems Conference*, Atlanta, 1996, pp. 327 - 332.

[40] S. Tapigue, M. Klingler, P. Besnier, S. Benhassine, and M. Drissi, "Analysis of Electromagnetic Resonance in the Case of a Vehicle Using Different Sets of Field

Points," in *IEEE Symposum on EMC*, Austin, 2009, pp. 127-132.

[41] S. Clarke and U. Jakobus, "Dielectric Material Modeling in MoM-Based Code FEKO," *IEEE Antennas and Propagation Magazine*, vol. 47, no. 5, pp. 140 - 147, October 2005.

[42] Radio Communications Agency EMC Awareness. [Online]. http://www.ofcom.org.uk/static/archive/ra/topics/research/RAwebPages/Radiocomms/pages/interexpl/aviation.htm

[43] Unsafe at any speed. [Online]. http://spectrum.ieee.org/aerospace/aviation/unsafe-at-any-airspeed

[44] G. Tait, "Propagation and shielding of radio-frequency emissions between multiple-connected reverberant spaces," in *IEEE International Symposium on EMC*, Fort Lauderale, 2010.

[45] T. Yang and J. L. Volakis, "Aperture coupling method for EMI analysis of microwave circuits within multilayer cavities," in *IEEE Antennas and Propagation Society International Symposium* , Albuquerque, 2006, pp. 53 - 56.

[46] K.L. Wong, *Design of Nonplanar Microstrip Antennas and Transmission Lines*.: Wiley Series in Microwave and Optical Engineering, 1999.

[47] Rhode & Schwarz, "Measurement of dielectric material properties," RAC0607-0019, 2006.

[48] M. D. Deshpande, C. J. Reddy, P. I. Tiemsin, and R. Cravey, "A new approach to estimate complex permittivity of dielectric materials at microwave frequencies using waveguide measurements," *IEEE Trans on MicrowaveTheory and Techniques*, vol. 45,

no. 3, pp. 359 - 366 , March 1997.

[49] S. Amari and and J.Bornemann, "LSE - and LSM-mode sheet impedance of thin conductors," *IEEE Transactions on Microwave Theory and Techniques*, vol. 44, no. 6, pp. 967-970, June 1996.

[50] F.A. Fisher, R. A. Perala, and J. A. Plumer, *Lightning Protection of Aircraft*. Pittsfield, MA: Lightning Technologies Inc, 1990.

[51] D. H. Trout, J. E. Stanley, and P F. Wahid, "Evaluation of lightning Induced Effects in Composit Fairing Structure (Part 1 – Frequency Domain)," in *ACES Conference*, Williamsburg, March 2011.

[52] Department of Defense, "Electromagnetic Environmental Effects Requirements for Systems," MIL-STD-464A, 2003.

[53] V.A Rakov and M.A. Uman, *Lightning Physics and Effect*. Cambridge: Cambridge University Press, 2003.

[54] D. H. Trout, J. E. Stanley, and P F. Wahid, "Evaluation of lightning Induced Effects in Composit Fairing Structure (Part 2 – Time Domain)," in *ACES Conference*, Williamsburg, March 2011.

[55] M. S. Sarto, "Hybrid MFIE/FDTD analysis of the shielding effectiveness of a composite enclosure excited by a transient plane wave," *IEEE Transactions on Magnetics*, vol. 36, no. 4, pp. 946-950, July 2000.

[56] C. L. Holloway, M. S. Sarto, and M. Johansson, "Analyzing carbon-fiber composite materials with equivalent-layer models," *IEEE Transactions on EMC*, vol. 47, no. 4, pp.

833 – 844, Nov. 2005.

[57] B. C. Gabrielson, *The Aerospace Engineer's Handbook of Lightning Protection*. Gainsville, VA: Interfence Control Tehcnologies, 1988.

[58] F. M. Tesche, M. Ianoz, and T. Karlsson, *EMC Analysis Methods and Computational Models*. New York: John Wiley and Sons, 1997.

[59] R.W Evans, "Direct and Indirect Lightning Effects on Composite Materials," NASA Contractor Report 4783, 1997.

[60] D. Weston, *Electromagnetic Compatibility: principles and applications*, 2nd ed. New York: CRC Press , 2001.

[61] FEKO. (2010) Field Computations involving objects of arbitrary shape. [Online]. http://www.feko.info/

[62] WIPL-D. (2010) electromagnetic modeling of composite and dielectric structures. [Online]. http://www.wipl-d.com/index.php

[63] B. Archembeault, C. Brench, and O. M. Ramahi, *EMI/EMC Computational Modeling Handbook Second Edition*. Norwell: Kluwer Academic Publishers, 2001.

[64] Mathew N.O. Sadiku, *Numerical Techniques in Electromagnetics, Second Edition*. Boca Rato, FL: CRC Press, 2001.

[65] R.F. Harrington, *Field Computation by Moment Methods*. New York: IEEE Inc., 1993.

[66] B. Kolundzija and A. Djordjevic, *Electromagnetic Modeling of Composite Metallic and Dielectric Structures*. Boston: Artech House, 2004.

[67] U. Jakobus, "Comparison of different techniques for the treatment of lossy

dielectric/magnetic bodies within the method of moments formulation," *AE¨U International Journal of Electronics and Communications*, vol. 54, no. 3, pp. 163-173, 2000.

[68] S. M. Rao, D. R. Wilton, and A. W. Glisson, "Electromagnetic Scattering by Surfaces of Arbitrary Shape," *IEEE Transactions on Antennas and Propagation*, vol. AP-30, no. 3, pp. 409-418, May 1982.

[69] W. C. Chew, J. M. Jin, E. Michielssen, and J. Song, *Fast and Efficient Algorithms in Computational ELectromagnteics*. Norwood, MA: Artech House, Inc., 2001.

[70] Computer Simulation Technology, "CST Microstripes Reference Manual," 2009.

[71] FEKO. (2011, April) How to increase the dynamic range of shielding problems in FEKO. [Online]. www.feko.info/support/helpcenter/how-to/how-to-increase-the-dyn

[72] Yinshang Liu and K.J. Webb, "On detection of the interior resonance errors of surface integral boundary conditions for electromagnetic scattering problems," *IEEE Transactions on Antennas and Propagation*, vol. 49, no. 6, pp. 939 - 943, June 2001.

[73] David Davidson, *Computational EM for RF and Microwave Engineering*, 2nd ed. Cambridge, United Kingdom: Cambridge Univeristy Press, 2011.

[74] EM Software and Systems, "FEKO User's Manual," 2008.

[75] W. C. Gibson, *The Method of Moments in Electromagnetics*. Boca Raton, FL: Chapman and Hall/CRC, 2008.

[76] U. Jakobus, M. Bingle, and J Van Tonder, "Recent extensions in FEKO: Parallel MLFMM and waveguide excitations," in *22nd Annual Review of Progress in Applied*

Computational Electromagnetics, 2006, pp. 695-700.

[77] U. Jakobus, J. Tonder, and M. Schoeman, "Advanced EMC modeling by means of a parallel MLFMM and coupling network theory," in *IEEE International Symposium on Electromagnetic Compatibility* , Detroit, 2008, pp. 1-5.

[78] N. Geng, A. Sullivan, and pp 1561 − 1573 L Carin, "Multilevel Fast-Multipole Algorithm for Scattering from Conducting Targets Above or Embedded in a Lossy Half Space," *IEEE Transactions on Geoscience and Remote Sensing*, vol. 38, no. 4, pp. 1561 − 1573, July 2000.

[79] V. Raykar, "A short primer on the fast multipole method," University of Maryland, College Park, 2006.

[80] Efield AB. (2010, March) efield: Multilevel Fast Multipole. [Online]. http://www.efieldsolutions.com/mlfmm.php

[81] J.M. Song, C. C.Lu, and W. C. Chew, "Multilevel fast multipole algorithm for electromagnetic scattering by large complex objects," *IEEE Trans. Antennas Propagat*, vol. 36, no. 4, pp. 518-526, April 1988.

[82] K. Sertel, "Multilevel fast multipole method for modeling permeable sturctures using conformal finite elements," Dissertation, 2003.

[83] J Song and W. Chew, "Error analysis for the truncation of multipole expansion of vector Green's functions," *IEEE Mircrowave and Wireless Components and Letters*, vol. 11, no. 7, pp. 311-313, July 2001.

[84] P. L. Rui, R. S. Chen, D.X. Wang, and K. N. Yungpp, "A spectral multigrid Method

Combined with MLFMM for Solving Electromagnetic Wave Scattering Problems," *IEEE Transactions n Antennas and Propagation*, vol. 55, no. 9, pp. 2571- 2577, Sep 2007.

[85] Y. Saad, *Iterative Methods for Sparse Linear Systems, 2nd Edition*., 2000.

[86] P.L. Rui, R. S. Chen, Z.W. Liu, and Y. N. Gan, "Schwarz-Krylov subspace method ofr MLFMM analysis of electromagnetic wave scattering problems," *Progress in Electromagnetics Resaerch*, vol. PIER 82, pp. 51-63, 2008.

[87] M. Nilsson, "Stability of the high frequency fast multipole method for Helmholtz' equation in three dimensions," *BIT Numerical Mathematics*, vol. 44, pp. 773-791, 2004.

[88] Y.J. Liu and N.Nishimura, "The fast multipole boundary element method for potential problems: A tutorial," *Engineering Analysis with Boundary Elements*, vol. 30, pp. 371-381, 2006. [Online]. www.elsevier.com/locate/enganabound

[89] B. Kolundzija, J. Ognjanovic, and T Sarkar, "Analysis of Composite Metallic and Dielectric Structures - WIPL-D code," in *Proc. of 17th Applied Computational Electro-magnetics Conference*, Monterey, 2001, pp. 246-253.

[90] WIPL-D Team, *WIPL-D Pro v9.0 User's Manual*. Belgrade, Serbia, 2011.

[91] R. W. McMillan and J.H. Kirkland, "Comparison of WIPL-D to other EM computation methods," in *20th Annual Review of Progress in Applied Computational Electromagnetics*, Syracuse, 2004.

[92] B. H. Jung, T. K. Sarkar, and M. Salazar-Palma, "Combined field integral equaiton for the analysis of scattering from 3D conducting bodies coated with a dielectric material,"

Microwave and Optical Technical Letters, vol. 40, no. 6, pp. 511-516, March 2004.

[93] U. Jakobus, "Analysis of coated metallic surfaces with physical optics for the solution of high-frequency EMC problems".

[94] U. Jakobus and I. P. Theron, "Analysis of coated metallic surfaces with physical optics for the solution of high-frequency EMC problems," in *15th International Zurich Symposium on Electromagnetic Compatibility*, Zurich, 2003, pp. 257 - 261.

[95] EM Software & Systems, "FEKO Short Course," 2010.

[96] REFTAS, "Reverberation Chamber Theory/Experiment Course Notes," Oklahoma State University, Stillwater, 2011.

[97] G. B. Tait and M. B.Slocum, "Random-Walk technique for measuring the electromagnetic environment in electrically large reflective spaces," *IEEE Transactions on Instrumentation and Measurement*, vol. 60, no. 3, pp. 1003-1009, March 2011.

[98] G. Orjubin, "Maximum Field Inside a Reverberation Chamber Modeled by the Generalized Extreme Value Distribution," *IEEE Transactions on Electromagnetic Compatibilit*, vol. 49, no. 1, pp. 104 - 113 , February 2007.

[99] T. Nguyen, "RF Loading Effects of Aircraft Seats in an electromagnetic Reverberation Environment," NASA Report T. Nguyen, RF Loading Effects of Aircraft Seats in an electromagnetic Reverberation Environment, NASA archive, 1999.

[100] CST Microstripes, "Microstripes Reference Manual,".

[101] K.P. Thakur and W.S Holmes, "Dielectric constant and loss factor of dielectric material using finite element method in a cavity," in *IEEE Microwave Conference*, Sydney,

2000, pp. 432 - 436.

[102] B. Davis et al., "Complex permittivity of planar building materials measured with an ultra-wideband free field antenna measurement system," *Journal of Research of the National Institute of Standards and Technology*, vol. 112, no. 1, pp. 67-73, January-February 2007.

[103] M.D. Deshpande and C.J. Reddy, "Application of FEM to estimate complex permittivity of dielectric material at microwave frequency using waveguide measurements," NASA, Langley Research Center, Technical Report 1995.

[104] Agilent Technologies, "Basics of measuring the dielectric properties of materials," Aplication Note,.

[105] Sung Seo, Woo Seok Chin, and Dai Gil Lee, "Characterization of electromagnetic properties of polymeric composite materials with free space method," *Composite Structures, Elsevier*, vol. 66, no. 1-4, pp. 533-542, June 2004.

[106] "Requirements for the Control of Electromagnetic Interference Characteristics of Subsystems and Equipment," Department of Defense (U.S.), Standard MIL-STD-461F, 2007.

[107] M. Kandula, K. Hammad, and P. Schallhorn, "CFD Validation with LDV Test Data for Payload/Fairing Internal Flow," in *35th AIAA Fluid Dynamics Conference*, Toronto, 2005.

[108] ETS Lindgren, "EMCO 3115, User Manual. [Online],".

[109] C. Su, H. Ke, and T. Hubing, "Overview of Electromagnetic Modeling Software," in

25th Annual Review of Progress in Applied Computational Electromagnetics, Monterey, 2009, pp. 736-741.

[110] R. W. McMillan and J. H. Kirkland, "Comparison of WIPL-D to Other EM Computation Methods," in *20th Annual Review of Progress in Applied Computational Electromagnetics*, Syracuse, 2004.

[111] D. H. Trout, J. E. Stanley, and P F. Wahid, "Mutual coupling of internal transmit/receive pair in launch vehicle fairing model using WIPL-D," in *ACES Conference*, Willaimsburg, March 2011.

[112] R. Chair, A. Kishk, and K. Lee, "Comparative Study on the mutual coupling between different sized cylindrical dielectric resonators antennas and circular microstrip patch antennas," *IEEE Transactions on Antennas and Propagation*, vol. 53, no. 3, pp. 1011-1019, March 2005.

[113] M. F. Iskander and M.A.K.Hamid, "Numerical solution of the near-field transmission between two H-plane sectoral electromagnetic horns," *IEEE Transactions on Antennas and Propagation*, vol. AP-24, pp. 87-89, Jan 1976.

[114] D. H. Trout, J. E. Stanley, and P. F. Wahid, "Electromagnetic Launch Vehicle Fairing and Acoustic Blanket Model of Received Power using FEKO," in *ACES Conference*, 2011.

[115] J. E. Stanley, D. H. Trout, S. K. Earles, I. N. Kostanic, and P F. Wahid, "Analysis of Multi-Layer Composite Cavity Using FEKO," *ACES JOURNAL*, vol. 25, no. 1, pp. 69-74, January 2010.

[116] J. E. Stanley, D. H. Trout, S. K. Earles, I. N. Kostanic, and P. F. Wahid, "Analysis of multi-layer composite cavity using FEKO," in *25th Annual Review of Progress in Applied Computation Electromagnetics*, Monterey, March 8-12, 2009, pp. 643-647.

[117] U Jakobus, "Comparison of different techniques for the treatment of lossy dielectric/magnetic bodies within the method of moments formulation," *AE¨U International Journal of Electronics and Communications*, vol. 54, no. 3, pp. 163-173, 2000.

[118] KSC, Analex Corporation, Unniversity of Mississippi, "Indirect Lightning Effects Analysis for A Graphite Composite Structure," Kennedy Space Center, Center Director Discretionary Fund Report 2009.

[119] Y. Huang, R. Narayanan, and G. R. Kadambi, "Electromagnetic Coupling Effects on the Cavity Measurement of Antenna Efficiency," *IEEE Transactions on Antennas and Propagation*, vol. 51, no. 11, pp. 3064 -3071, November 2003.

[120] S.A. Tretyakov, S.I. Maslovski, A.A. Sochava, and C.R Simovski, "The influence of complex material coverings on the quality factor of simple radiating systems," *IEEE Transactions on Antennas and Propagation*, vol. 53, no. 3, pp. 965-970, March 2005.

[121] Cheng-Nan Chiu and Chun Hsiung Chen, "Scattering from an advanced composite cylindrical shell," *IEEE Transactions on Electromagnetic Compatibility*, vol. 38, no. 1, pp. 62-67, February 1996.

[122] S. Rea, E. Orr D. Linton, and J. McConnell, "Electromagnetic shielding properties of carbon fibre composites in avionics systems," *Microwave Review*, pp. 29-32, June 2005.

[123] M.P. Robinson, J. Clegg, and A.C. Marvin, "Radio frequency electromagnetic fields in large conducting enclosures: effects of apertures and human bodies on propagation and field-statistics," *IEEE Transactions on Electromagnetic Compatibility*, vol. 48, no. 2, pp. 304 - 310, May 2006.

[124] Less EMF. (2011) EMF Shielding & Conductive Fabrics. [Online]. www.lessemf.com/fabric.html

[125] Dupont. (2011) Kapton® polyimide film. [Online]. http://www2.dupont.com/Kapton/en_US/index.html

[126] AFSC, "Air Force EMC Design Handbook," Air Force, Handbook AFSC DH 1-4, 1972.

[127] IEEE, "IEEE Standard Method for Measuring the Effectiveness of Electromagnetic Shielding Enclosures," IEEE Std 299, 2006.

[128] E.L. Bronaugh and D.N. Heirman, "Estimating mueasurement uncertainty," *IEEE Practical Papers*, pp. 32-51, 2004.

[129] Chromerics, "EMI Shield Performance Data,".

[130] D. H. Trout, J. E. Stanley, and P F. Wahid, "Evaluation of lightning Induced Effects in Composit Fairing Structure," *Applied Computational Electromagnetics Society*, vol. 26, no. 12, pp. 981-988, December 2011.

[131] M. Sarto, "A matrix surface impedance formulation for the analysis of EM-Interactions to finite laminated composite slabs," in *IEEE International Symposium on Electromagnetic Compatibility*, Santa Clara, 1996, pp. 168-173.

[132] E. F. Casey, "Electromagnetic shielding by advanced composite materials," Kansas

State University, Interaction Note OI-49-H2, 1979.

[133] C. Baldwin, "Full-wave EM modeling and test verification in aerospace applications," in *IEEE EMC Symposium*, Austin, TX, August 17-21, 2009, pp. MO-PM-1-2.

[134] V. Rajamani and C.F. Bunting, "Validation of Modal/. MoM in shielding effectiveness studies of rectangular enclosures with apertures," *IEEE Trans Electromag*.

[135] EM & Software Systems, "[15] FEKO Quarterly, Field computations involving objects of arbitrary shape," March 2005.